SI 1. Description and comparison of the of Al Wusta-1 phalanx.

1.1 Pathology

The Al Wusta-1 (AW-1) phalanx shows evidence of pathological changes to the bone surface. Additional pathological bone formation affects the proximal half of the shaft, covering approximately one quarter of the dorsal surface, measuring 11.9 mm proximo-distally and 5.9 mm radio-ulnarly, and projecting approximately 2.5 mm from inferred 'normal' bone surface. Micro-CT scanning confirms that the additional bone is continuous with the cortical bone of the shaft, but there is no evidence of a fracture or other trauma (Fig. 2B, C). Its irregular, angular morphology suggests that this additional bone may be due to the ossification of the central slip of the extensor digitorum muscle (i.e., a "bony spur" or enthesophyte), which attaches to the intermediate phalanx in this region. The unusual, relatively circular cross-sectional shape of AW-1 may also reflect these pathological changes.

1.2 Linear metric analysis of the Al Wusta-1 intermediate phalanx

Linear measurements of AW-1 are presented in Supplementary Table 1. We conducted an analysis of nine linear measurements of intermediate phalanx shape across a sample of extant primates and fossil hominins (Supplementary Table S2). For extant non-human primates, intermediate phalanges (IPs) from all rays (2-5) of one side (either left or right) were included as it is possible that all non-human primate IPs may show similar morphology to human IPs[1,2]. However, human and fossil hominin IPs from the fifth ray (IP5) show a distinctive, asymmetrical shape that is not present in AW-1 and thus all *H. sapiens* IP5 specimens and potential IP5 fossil hominin specimens were excluded from the analysis. Although data from

multiple IPs from a single individual are not independent, without knowing the exact ray to which AW-1 belongs, nor the exact ray or number of individuals associated with several of the comparative fossil hominin intermediate phalanges, it is more conservative to include the range of morphological variation across multiple rays.

Linear measurements included the maximum proximo-distal length of the phalanx (i.e. total length), maximum dorso-palmar height of the proximal base, the dorso-palmar height and radio-ulnar breadth of the proximal articular facet, radio-ulnar breadth of the proximal shaft, and dorso-palmar height and radio-ulnar breadth of the midshaft and distal shaft, all of which could be confidently measured on AW-1.

All metrics were assessed and compared as a ratio of the total length of the phalanx. Comparisons across extant taxa, Neanderthals and *H. sapiens* (i.e. all taxonomic groups with large enough sample sizes) were evaluated using Mann-Whitney U pairwise comparisons with a Bonferroni correction for multiple comparisons (Supplementary Table 3). Relative comparisons of AW-1 and other fossil specimens were visually assessed via box-and-whisker plots (Supplementary Figure 1).

Comparative analyses reveal that there is substantial overlap across most taxa in all shape ratios. For any given shape ratio, AW-1 falls within the range of variation of cercopiths, *Gorilla*, *A. afarensis*, *A. sediba,* Neanderthals and *H. sapiens*. However, AW-1 is most similar to the median value or falls within the range of variation of recent and early *H. sapiens* for all shape ratios (Supplementary Figure 1), confirming its affiliation with *H. sapiens* revealed by the 3D geometric morphometric analyses (see main text and below). More specifically, AW-1 is very similar to the *H. sapiens* median value in the relative

radioulnar breadth of the proximal base and the proximal shaft, and the dorso-palmar height at midshaft. AW-1 falls within the lower range of variation of *H. sapiens*, and outside or at the extreme of the Neanderthal range of variation, in its dorso-palmar height and radioulnar breadth proximal facet, and its radioulnar breadth at midshaft and the distal shaft.

Note that published values for the controversial *H. sapiens* specimen Cueva Victoria CV-0 specimen are included in the proximal base breadth and midshaft breadth and height shape ratios (Supplementary Figure 1). This specimen is always the most extreme outlier in the box-and-whisker plots, and falls in the direction of the cercopithecid median value, suggesting that this specimen is indeed that of *Theropithecus*, and not *H. sapiens*, supporting Martínez-Navarro and colleagues[1,2].

1.3 Geometric morphometric comparison of non-human primate, fossil hominin and Al Wusta-1 phalanges

To provide a broader interpretive context for AW-1, we provide a principal components analysis of geometric morphometric landmark data (Supplementary Table 4, Supplementary Figure 2) on a sample of phalanges from a range of primates including fossil hominins (Supplementary Table 5). In Figure 3 (main text) and Supplementary Figure 3, PC1 and PC2 together account for 61% of group variance in shape. AW-1 is separated on these two shape vectors from the non-human primates and most of the Neanderthals by a shorter, wider diaphysis and palmarly flatter proximal base. It shares a proximal head that is higher to the right (dorsal view) with *H. sapiens*, although this may be a function of the proportion of left and right sides in each sample. AW-1 falls closest to the Holocene and early *H. sapiens* and is well differentiated from all non-human primates. This is shown by the Procrustes distances

from AW-1 to the mean shapes of each taxonomic group (Figure 3, Supplementary Figure 3 and Supplementary Table 6).

1.4 Geometric morphometric analysis restricted to AW-1 and hominin phalanges of known side and digit numbers

Details of the sample are given in Supplementary Table 7. Methods and Results for pooled left and right hands are given in the main text (see Figure 4 and also Supplementary Tables 8-9.)

1.4.1 Left and right 2nd, 3rd and 4th intermediate phalanges separated.

The results showing AW-1 compared separately to right and to left phalanges (Supplementary Figure 4, Supplementary Tables 10-11) are very similar to the pooled sample (see main text, Figure 4 and Supplementary Tables 8-9), such that AW-1 is closest to Holocene *H. sapiens* 3rd rays for both right and left hand, although Pleistocene *H. sapiens* configurations fall almost completely inside the scatter for the Holocene *H. sapiens* sample. AW-1 is most distinct from the Neanderthal phalanges of both the left and right hands. The greatest separation between AW-1 and other groups is described by PC2 for both the right and left phalanges. These vectors describe the shape difference between shorter and stockier vs. longer and narrower configurations. AW-1 is taller and narrower (in all directions: dorso-palmarly, proximo-distally and radio-ulnarly) than shapes towards the other end of the PC2s, which describe most of the Neanderthal phalanges. Again, these analyses suggest that AW-1 is likely to be a 3rd intermediate phalanx from a *H. sapiens* individual.

1.5 Cross sectional geometry analyses

1.5.1 Materials and Methods

Cross-sectional geometry (CSG) of bones examines the amount and distribution of cortical bone in the cross section, which reflects primarily the impacts of body size, body shape, and activity on the skeleton[3-6]. CSG of AW-1 and the comparative 2nd-4th phalanges (Supplementary Table S7) were calculated in ImageJ[7] using the BoneJ plugin[8] and using the same microCT data as for the GMM analyses. Slices at 54% of total AW-1 phalanx length (measured from the proximal end) were analysed to avoid the influence on cross-sectional properties of the pathological bone formation on the shaft. Total area (TA) of the cross section was calculated by filling the medullary cavity with the 'fill holes' function of ImageJ and rerunning the slice through BoneJ. Percent cortical area (%CA) reflecting cortical bone thickness was calculated as 100*cortical area/TA. *J*, a measure of torsional and twice average bending rigidity, was calculated as the sum of maximum and minimum bending rigidities (I_{max} and I_{min} respectively)[9].

GMM analyses suggest that AW-1 is a 3rd intermediate phalanx, but plots were generated for each of manual rays 2-4 in case these analyses suggested otherwise. Where left and right sides were present for the same ray of the same individual, the mean was used.

As body size and activity are both important determinants of bone cross-sectional properties (see above), CA and *J* were plotted against bone length to examine whether the cross-sectional properties relative to body size could differentiate Neanderthal, Pleistocene *H. sapiens* and Holocene *H. sapiens* and thus be informative regarding the taxonomic affiliation

of AW-1. However, it must be noted that CSG of the phalanges, unlike the limb long bones[4,8], is not well documented in the literature and the relative importance of body size, activity and taxonomy remain to be investigated in detail. The relationship between I_{max} and I_{max}, which reflects the circularity of bone distribution was also examined by plotting I_{max} against I_{min}. Plots were generated using IBM SPSS Statistics v. 23.

1.5.2 Results

In general, AW-1 lies outside of the range of CSG for intermediate phalanges from ray 2, well within the range for ray 3, and at the upper end of the range for ray 4 (Supplementary Figure 5), supporting the interpretation that AW-1 is most likely to be a 3rd intermediate phalanx. For all cross-sectional properties, Holocene *H. sapiens* show a large range of variation and the small sample of Neanderthals and Pleistocene *H. sapiens* do not appear well differentiated from the Holocene specimens. While generally within the range of the comparative specimens, AW-1 falls just outside the range of the sample for I_{max} relative to I_{min}, with a low ratio indicating an unusually circular cross-section. In the long bones of the lower limb, more circular shafts indicate similar loading in multiple directions[10-11], but its precise interpretation for manual phalanges remains to be explored.

Further work to document the range of variation in phalanx CSG and its relationship to ancestry and behaviour patterns would be required to further interpret the cross-sectional circularity of the AW-1. A relationship between this high level of circularity and the pathological bone formation on the dorsal surface of AW-1's shaft cannot be excluded, since the shaft could be expanded in a dorso-palmar direction even where external appearance is

normal, which would serve to lower the I_{max}/I_{min} ratio. Alternatively, a generally high level of loading might account for both the enthesophyte and more circular cross-section of the shaft.

SI 2. U-series and combined US-ESR dating of fossil bone and teeth from Al Wusta.

2.1 Materials and Methods

2.1.1 Material

The human phalanx (AW-1, lab code for U-series = 3675) and a hippopotamus tooth fragment (lab code WU1601) were collected from Trench 1. The external dose rate calculations are based on the data from OSL sample PD40 (Supplementary Table 16), which was collected at the equivalent position within unit 3a.

2.1.2 U-series analysis

U-series analysis of bones can be used to reconstruct U-uptake phases. Modern bones are virtually U free. All the uranium that is measured in fossil samples migrated into the skeletal tissues after these were buried. However, it is difficult to establish whether this U-uptake was a single stage process that occurred a short time after burial, or whether the U-accumulation was a complex, multistage process that may have commenced a significant time after the original burial[12]. In any case, as long as there is no indication for uranium leaching, the calculated U-series age results have to be regarded as minimum age estimates with respect to the age of the fossil.

The experimental setup for the U-series analysis of the AW-1 phalanx was previously described in Grün and colleagues[12]. Laser ablation (LA) was used to drill a number of holes the finger bone following the approach of Benson et al.[13]. After a cleaning run with the laser

set at a diameter of 460 μm, seven holes were drilled for 1000 s (Supplementary Figure 6A) with the laser set at 330 μm. The isotopic data streams (Supplementary Figure 6B) were converted into $^{230}Th/^{234}U$ and $^{234}U/^{238}U$ activity ratios and apparent Th/U age estimates (Supplementary Figure 6C) and subsequently binned into 30 successive sections (each containing 33 cycles) for the calculation of average isotopic ratios and ages (Supplementary Figure 6D; Supplementary Table 12).

A similar experimental setup and methodology were employed for the LA U-series analysis of tooth sample WU1601 (Supplementary Figure 8). Individual closed system U-series age estimates were calculated for each ablation spot and the whole analytical data of the enamel and dentine sections were integrated to provide the data input for the ESR age calculations (Supplementary Table 13).

2.1.3 ESR dose evaluation

Enamel was collected from tooth WU1601 and powdered <200 μm. The sample was then divided into 11 aliquots and gamma irradiated with a Gammacell-1000 Cs-137 source to the following doses: 0, 49, 97, 146, 243, 340, 486, 873, 1457, 2430 and 3397 Gy. ESR measurements were carried out at room temperature with an EMXmicro 6/1 Bruker ESR spectrometer coupled to a standard rectangular ER 4102ST cavity. The following procedure was used to minimise the analytical uncertainties: (i) all aliquots of a given sample were carefully weighed into their corresponding tubes and a variation of <1 mg was tolerated from one aliquot to another; (ii) ESR measurements were performed using a Teflon sample tube holder inserted from the bottom of the cavity to ensure that the vertical position of the tubes

remains exactly the same for all aliquots. The following acquisition parameters were used: 3-30 scans (depending on the sample and aliquot measured), 1 mW microwave power, 1024 points resolution, 15 mT sweep width, 100 kHz modulation frequency, 0.1 mT modulation amplitude, 20 ms conversion time and 5 ms time constant.

ESR intensities were extracted from T1-B2 peak-to-peak amplitudes of the ESR signal of enamel[14], and then corrected by the corresponding number of scans and aliquot mass. Fitting procedures were carried out with the Microcal OriginPro 9.5 software using a Levenberg-Marquardt algorithm by chi-square minimization. D_E values were obtained by fitting a single saturating exponential (SSE) function through the experimental data, with data weighting by the inverse of the squared ESR intensity ($1/I^2$)[15].

The sample was measured three times on different days in order to evaluate the precision in measurement and D_E. Only small variation of between 1.5% and 2.7% (1-σ) were found over the three days, respectively. The final D_E value was calculated by pooling all the ESR intensities derived from the three repeated measurements in a single dose response curve (DRC)[16]. In order to avoid D_E overestimation caused by the use of the SSE function, an appropriate maximum irradiation dose (D_{max}) was selected in accordance with the recommendations by Duval and Grün[17]: given the magnitude of the D_E value (~100 Gy), D_{max}/D_E should be between 5 and 10, and final dose evaluation were thus done with D_{max}=873 Gy (D_{max}/D_E =9). The final DRC is shown in Supplementary Figure 9.

2.1.4 Dose rate evaluation and US-ESR age calculation

For the dose rate calculations, the following parameters were used: an alpha efficiency of 0.13 ± 0.02[18], Monte-Carlo beta attenuation factors[19], recently published dose-rate conversion factors[20]. For the calculation of the external sediment dose rate, the data of OSL sample PD40 (Supplementary Table 16) were used. The total external dose rate of 438 ± 27 μGy/a consists of 254 ± 25 μGy/a cosmic dose rate (for the actual depth of 25 cm below surface), 180±10 μGy/a external gamma dose rate, plus the external beta dose rate was corrected for the tooth configuration, resulting in 4 μGy/a.

Combined US-ESR ages were calculated with DATA[21] using the US model defined by Grün et al[22]. Further details about this dating method applied to fossil teeth may be found in Duval[23]. The other details of the age result of 103+10/-9 ka are shown in Supplementary Table 14.

2.2 Results and discussion

2.2.1 U-series dating of the Al Wusta-1 phalanx

Some scans show elevated ^{232}Th levels (see Supplementary Figure 6B, around cycle 250), which is the result of probing some pores that may be filled with detrital material. However, all ^{238}U/^{232}Th elemental ratios are well above 50. Supplementary Figure 6E shows that the calculated ages of the cycles with lower U/Th ratios are not affected by detrital ^{230}Th, which would systematically increase the results.

All age calculations are based on closed system assumptions, they are thus apparent age estimates. U/Th ages were calculated using the Isoplot 3.75 Excel add-on[24]. Note that this program does not calculate asymmetric errors. All reported errors are 2-σ. We did not use the diffusion-adsorption decay (DAD) model of Sambridge and colleagues[25] as there is evidence of at least two discrete U-uptake phases.

All data steams have in common that the outer domains yield younger lower apparent ages than those further inside the bone (Supplementary Figure 7A). This is clearly associated with higher U concentrations (Supplementary Figure 7B and C). This indicates a second discrete phase of U-accumulation, which overprinted the original isotopic signature. The more U was taken up at that later phase, the younger becomes the apparent U-series age. For each of the holes, the apparent age plateaus after an initial increase. These age plateaux systematically increase from Hole 1 to Hole 7 (see Supplementary Figure 7A). Interestingly, there is a reverse trend with older plateau ages associated with slightly higher U-concentrations (Supplementary Figure 7D). This is could be related to a process where the domains, which had accumulated more U during an initial uptake phase, were relatively less affected by any subsequent U-migration processes.

To conclude, the age plateaux of hole #7 of 87.6 ± 2.5 ka represents the minimum age of the finger bone. The true age of the bone may be older because (i), the age plateaux of holes #1 to 6 are affected by later U-uptake phases, and it is not possible to ascertain whether the age plateau of hole #7 was not affected; (ii), the observed, complex U-migration processes may have commenced a considerable time after the initial burial.

2.2.2 Combined US-ESR dating of the fossil tooth

Apparent U-series age results obtained for the dental tissues are close to those obtained in the human phalanx: 83.5 ±8.1 ka in the enamel and 65.0 ± 2.1 ka in dentine. These results suggest that the tooth sample is at least 83 ka old.

The combined US-ESR age calculation yields a result of 103+10/-96 ka. This ESR result agrees with OSL sample PD40 (98.6 ± 7 ka) within error.

SI 3: Optically stimulated luminescence (OSL) dating of Al Wusta.

3.1 Sample collection and preparation

Trenches were dug through the marl beds into the underlying aeolian sand (Unit 1) at Al Wusta. Three samples (PD15, PD17 and PD41, Supplementary Figure 13) were collected from Unit 1 sands underlying the southern marl outcrop, upon which the AW-1 phalanx and the majority of the animal fossils were found. A fourth sample (PD40, Supplementary Figure 13) was taken from Unit 3. PD40 and PD41 were taken from the same trench. OSL samples were collected by hammering opaque tubes into cleaned section faces. In the laboratory, quartz was extracted from the portion of each sample which had not been exposed to sunlight. Samples were initially wet-sieved to isolate the 212-180 μm size fraction, and carbonates and organic matter were subsequently removed using 1M HCl and H_2O_2 respectively. The samples were then re-sieved at 180 μm and quartz was extracted from the >180 μm fraction using density separations at 2.62 and 2.70 g/cm^3 and a subsequent HF acid etch (23M HF for 60 min followed by a 10M HCl rinse). Since Nefud quartz samples are prone to feldspar contamination, an additional one week H_2SiF_6 treatment followed by an HCl rinse was also performed. Etched samples were re-sieved at 150 μm, to remove partially dissolved grains, and stored in opaque containers prior to measurement.

3.2 Luminescence measurements

3.2.1 Equipment

All OSL measurements presented here were carried out using a Risø TL/OSL-DA-15 automated dating system[26], fitted with a single-grain OSL attachment[27,28]. Optical stimulation

of single-grains used a 10 mW Nd: YVO_4 solid-state diode-pumped green laser (532 nm) focussed to yield a nominal power density of 50 W/cm^2, following[26]. All infra-red (IR) stimulation was carried out using an IR (870 nm) laser diode array yielding a power density of 132 mW/cm^2. OSL passed through 7.5 mm of Hoya U-340 filter and was detected using an Electron Tubes Ltd 9235QB15 photomultiplier tube. Irradiation was carried out using a 40 mCi ^{90}Sr/^{90}Y beta source giving ~6 Gy/min. This source is calibrated relative to the National Physical Laboratory, Teddington ^{60}Co γ-source (Hotspot 800[29]). Due to the spatial inhomogeneity of beta emitters across the active face of our ^{90}Sr/^{90}Y beta source, it was necessary to calibrate the dose rate to each individual grain position on a single-grain disc[30] using the method of Armitage and colleagues[31].

3.2.2 Single-grain measurement and analysis

Measurements were made on 2800-3600 individual quartz grains per sample (Supplementary Table 15), using the single-aliquot regenerative-dose (SAR) method[32], to estimate the equivalent dose (D_e). Since optimum measurement conditions vary between samples[32,33], single-grain dose recovery tests[34,35] were performed on two of the four samples (PD15 and PD17) using a known dose of ~50 Gy. A preheating regime of 260 °C held for 10 seconds prior to measurement of the natural/regenerated dose, and 220 °C held for 10 seconds prior to measurement of the test dose, yielded dose recovery ratios (measured dose/known dose) of 1.01 ± 0.03 for both samples and was adopted for subsequent D_e measurements. Optical stimulation was carried out at 125 °C for 2 s using the green laser. The OSL signal was that recorded during the first 0.3 s of stimulation, with a background signal from the last 0.3 s of stimulation subtracted[36,37]. Dose response curves were fitted with a saturating exponential or a saturating-exponential-plus-linear function. The standard error associated with each

individual D_e determination was estimated by Monte Carlo simulation. Curve fitting, D_e determination and Monte Carlo simulation were performed using version 4.31.9 of the Luminescence Analyst software[38].

It has been observed widely that the majority of quartz grains from unheated sedimentary deposits do not yield a measureable OSL signal[39-41] or display luminescence characteristics which indicate that they are unsuitable for age determination. Consequently, single-grain dating studies must adopt criteria for rejecting uninformative grains[40]. In this study, grains were rejected where one or more of the following conditions are met: (1) the OSL signal from the grain is too low to distinguish it from the variability in the background signal, determined using the "Tn signal more than 3 sigma above BG" rejection criterion in Luminescence Analyst[38]; (2) the recycling ratio[42] differs from unity by greater than two standard errors; (3) the IR-depletion ratio[17] is greater than two standard errors below unity; (4) recuperation exceeds 5% of the natural signal and (5) the sensitivity-corrected natural luminescence intensity is greater than the saturation intensity of the measured growth curve (termed "oversaturation" in Supplementary Table 15). In addition, grains were rejected where their measured D_e was within measurement uncertainty of 0 Gy at 2σ. This last criterion excludes intruded modern grains, and has been found necessary for the analysis of samples from similar contexts elsewhere in the Nefud Desert[43]. These rejection criteria were applied in order, and only the first cause of rejection is recorded in Supplementary Table 15. Of the 17,900 grains measured, only 265 displayed acceptable luminescence properties, a yield of 1.5%. The majority of grains (94%) were rejected due to low OSL signal intensity. Despite rigorous attempts to remove feldspar from the quartz fraction, fewer grains were accepted than failed the IR-depletion ratio criterion. This phenomenon has been observed in other single-grain studies on Nefud "quartz" e.g Petraglia and colleagues[43].

To determine the age of a sample from a single-grain dataset it is necessary to calculate a single value for the burial dose (D_b). Since the OSL samples presented here were taken from aeolian sand where complete resetting of the OSL signal prior to deposition may be assumed, and the small number of intruded grains were rejected prior to analysis, D_b was calculated for all samples using the central age model (CAM)[44]. Overdispersion (OD) values for the Al Wusta samples ranged from 16 ±3% to 26 ±3% (PD17 and PD40 respectively), which is consistent with values reported from well-bleached undisturbed sediments[33,45,46], supporting the use of the CAM to derive estimates of D_b. Equivalent dose distributions for each sample are presented in Supplementary Figure 10.

3.3 Environmental dose rate calculations

For HF acid etched sand-sized quartz grains, the environmental dose rate consists of external beta, gamma and cosmic ray components. Beta dose rates were measured using a Risø GM-25-5 low-level beta counting system[47] using MgO and Volkagem loess[48] standards, while gamma dose rates were measured using an EG&G Ortec digiDart-LF gamma-spectrometer using the "threshold" method. Dose rates were corrected for the effects of HF etching[49], grain size[50] and a water content of 5 ± 2.5%. The 2σ uncertainty on water content encompasses completely dry conditions (0%) and saturation for 25% of the burial period (10%), representing the full range of reasonable mean water content scenarios of a freely draining aeolian sand. Cosmic ray dose rates were calculated using site location (27.4°N, 39.4°E, 925 m elevation) and present day sediment burial depths[51]. For samples other than PD40, the overburden was assumed to consist of 40 cm of sand (the target sampling depth below the base of the marl) containing 5% water by mass (assumed bulk density 1.74 g/cm^3), with the remainder of the overburden depth being carbonates also containing 5% water by mass

(measured bulk density 1.36 g/cm^3). For PD40, the entire overburden was assumed to be sand with an assumed bulk density of 1.74 g/cm^3. Using these assumptions, cosmic rays contribute between 33 % (PD15) and 44% (PD40) of the total calculated dose rate, meaning that accurate estimation of the cosmic ray dose rate is more important for these samples than is normally the case. Therefore, the assumptions regarding burial depth require detailed consideration. Firstly, it was assumed that Unit 2 was deposited instantaneously above PD15-17 and PD41, while the full depth of Unit 3a was deposited instantaneously above PD40. This assumption allows the cosmic dose rate to be regarded as constant throughout the sample's burial period. For Unit 2, this assumption must approximate reality since the OSL ages for samples below Unit 2 are indistinguishable from those above. For unit 3 geologically instantaneous deposition cannot be demonstrated, but seems likely based on the interpretation that this deposit represents the encroachment of fluvial sedimentation during the final drying of Al Wusta lake (SI Section 5). Uncertainties on the cosmic ray dose rate were set at ±10%. Assuming that the overlying sediments were deposited rapidly, mean overburden during a sample's burial period is unlikely to have been lower than that in the present day. Consequently, cosmic ray dose rates calculated as described above are either accurate or overestimates of mean burial dose rates. Cosmic ray dose rate overestimation will occur where appreciable reduction in the depth of overlying sediments has occurred since burial. In the case of samples overlain by carbonate beds (all except PD40), the cohesive nature of these sediments suggests that limited removal of overlying carbonates has occurred since burial. Conversely, the coarse surface lag (Unit 3b) above Unit 3a (Sample PD40) suggests that some overburden loss due to deflation has occurred (SI Section 5). It is difficult to estimate the quantity of material lost due to this process, but the sensitivity of the true cosmic ray dose rate to deflation may be estimated. In the present case, the lower (-10%) boundary of the estimated cosmic ray dose rate would be achieved by adding ~40 cm of sand (bulk

density 1.74 g/cm^3) to the burial depth of the shallow samples (PD17 and 40), or ~70 cm to the burial depth of the deeper samples (PD15, 16, 41). However, this calculation represents the worst-case scenario, since it implies greater overburden throughout the burial period, followed by instantaneous removal of ~40/~70 cm of sand immediately prior to sampling. If a more realistic model, assuming continuous deflation throughout the burial period is used, then the lower boundary of the estimated cosmic ray dose rate is achieved after removal of 80 cm of sand overlying the shallow samples, and 140 cm of sand overlying deeper samples. These considerations suggest that the ±10% (1σ) uncertainties assumed for our cosmic ray dose rates encompass reasonable variations in overburden density over time.

Dose rates and sample ages are presented in Supplementary tables 16 and 17 respectively. All analyses were carried out in the Royal Holloway Luminescence Laboratory by SA and R C-W.

SI 4 Site chronology and Bayesian model.

The combination of different numerical dating methods enables us to provide ages for AW-1 and associated sediment and fossils. The chronostratigraphic evidence available may be summarized as follows (Supplementary Figures 11 and 12):

- The human phalanx was found on the surface of Trench 1, on an exposure of Unit 3b. Direct U-series dating of AW-1 itself provides an age of 87.6 ± 2.5 ka (2σ confidence level). This result should be regarded as a minimum age for the fosil..
- A hippopotamus tooth (WU1601) was collected from Trench 1 within Unit 3a, one metre away from AW-1 (Supplementary Figure 14). U-series dating of the dental tissues provides apparent ages of 83.5 ± 8.1 ka (enamel) and 65.0 ± 2.1 ka (dentine) (2σ). These minimum age results are consistent with that obtained for AW-1, suggesting that both fossils are coeval.
- Combined US-ESR dating of WU1601 yields an age of 103 +10/-9 ka (1σ), indicating a relatively early uranium uptake in dental tissues (p=-0.83 and -0.53 for enamel and dentine, respectively). This age estimate is compatible with the minimum age results derived from U-series dating of AW-1 and WU1601.
- The OSL sample collected from PD40 section within the same Unit 3a provides an age of 98.6 ± 7.0 ka (PD40). This estimate is consistent with the US-ESR age obtained for WU-1601 and the minimum age of ~88 ka obtained for AW-1.
- Three OSL samples collected from Unit 1 provides ages of 85.3 ± 5.6 ka (PD17), 92.2 ± 6.8 ka (PD41) and 92.0 ± 6.3 ka (PD15). These ages are internally consistent and a weighted mean age of 89.3±3.6 ka may be derived. Because Unit 1 is stratigraphically located below Unit 3a, these results provide a maximum possible age for Unit 3 and the associated fossils.

The combination of these data suggests a 2σ time interval of 85.1 to 96.5 ka for AW-1 (86.5-92.9 ka at 1σ) based on the minimum and maximum age constraints derived from the direct U-series age (87.6-2.5 = 85.1 ka) and the weighted mean OSL age of Unit 1 (89.3+7.2=96.5 ka). This age range agrees well with the US-ESR age result obtained for WU1601 collected close to AW-1 (Supplementary Figure 14).

In order to further constrain the chronology of the deposits, all these data were incorporated into a Bayesian sequential phase model with phase 1 (underlying aeolian sand) corresponding to Unit 1 and Phase 2 (lake phase) to both Units 2 (no samples dated) and 3. We have not excluded shared systematic uncertainties (e.g. uncertainties shared between OSL ages) from the uncertainty term on individual ages. The exclusion of shared systematic uncertainties may be appropriate where: 1) a number of age estimates for a single event are being combined (e.g. 10 OSL ages for a single stratum) or 2) where the principal aim is to determine the duration of time represented in a phase of activity/deposition. However, we use the Bayesian sequential phase model to determine the timing of deposition of the AW1 specimen. Here the uncertainties on individual ages (whether shared or not) do represent the uncertainty on the timing (but not, in the case of shared uncertainties, the duration) of deposition. With this type of model removing systematic uncertainties would give a false sense of precision to the depositional age for AW1. Modelled ages indicate that deposition of Unit 1 ceased 93.1 ± 2.6 ka (Phase 1, PD15, 17, 41) and that Units 2 and 3 and all associated fossils were deposited between 92.2 ± 2.6 ka and 90.4 ± 3.9 ka (Phase 2, all other ages). The end date for phase 2 should be treated as a maximum value since no overlying material is present, precluding the possibility of further constraining the end of this phase. The timing of the lake phase is earlier than that indicated by other humidity records from the region. Given that the three samples from sands underlying the lake (arid phase indicators) are internally consistent, and coincide with the MIS 5c

insolation minimum, we propose that the subsequent lake phase correlates with the strengthened summer monsoon associated with the insolation peak at 84 ka (Fig. 6).

The code used to produce the Bayesian sequence model is as follows:

```
Plot()
 {
  Sequence()
  {
   Boundary("Start 1");
   Phase("1")
   {
    Date("PD41",N(calBP(92200),6800))
    {
    };
    Date("PD17",N(calBP(85300),5600))
    {
    };
    Date("PD15",N(calBP(92000),6300))
    {
    };
   };
   Boundary("End of sand");
   Boundary("Start of lake");
   Phase("2")
   {
    Date("PD40",N(calBP(98600),7000))
    {
    };
    Before("i")
    {
     Date("AW-1",N(calBP(87600),1250))
     {
     };
    };
    Before("ii")
    {
     Date("Hippo enamel",N(calBP(83500),4050))
     {
     };
    };
    Before("iii")
    {
     Date("Hippo dentine",N(calBP(65000),1050))
     {
     };
    };
    Date("US-ESR",N(calBP(103000),10000))
    {
    };
   };
   Boundary("End of lake");
  };
 };
```

SI 5. Stratigraphy, sedimentology and palaeoecology.

5.1 Results

5.1.1 Sedimentology

Unit 1 consists of loose, cross-bedded medium to coarse sands that contain evidence for bioturbation and iron-staining, this deposit underlies the sequence across the whole Al Wusta site (Supplementary Figures 13 and 14). The carbonate beds (Unit 2) exposed at Al Wusta are structureless and homogeneous, with some evidence for weak, horizontal laminations in PD16 sediments at depths between 70-40 cm. Carbonate content is high throughout all three sequences (typically >50%, Supplementary Figure 13), but the sediments have a low density typical of diatomite when dry. Shell fragments are rare but are present in the base of PD15 and PD16 and towards the top of PD16. These fragments are obvious in thin section but not in hand specimen and any picked remains could not be identified to specific taxa. During sieving of samples for isotopic analysis the coarse residue, >63µm, was examined and ostracod fossils were not observable. XRD whole rock analysis (that characterises the mineralogy of crystalline mineral composition, and consequently will not identify organics and non-crystalline biominerals, i.e. diatoms), indicate that the samples are dominated by calcite (>90%) with minor amounts of quartz (Supplementary Table 18 and Supplementary Figure15). Peaks that are attributable to evaporitic minerals such as gypsum and halite are present but the peak heights are so small that they are indistinguishable from background noise. Unit 3a consists of medium sands that are weakly horizontally laminated and contain fragments of eroded marls, occasional clasts and shells (*Melanoides tuberculata* and *Planorbis* sp). The upper part of Unit 3 (Unit 3b) is effectively desert pavement and has been

formed by the aeolian deflation of Unit 3a, concentrating clasts, shells, lithic and fossils at the land surface. The upper parts of Unit 3a contain calcite-cemented rhizolith that, as a result of progressive sediment deflation, now occur at the land surface as a cemented cap.

5.1.2 Micromorphology

All samples are dominated by homogeneous microsparite with some local zones of spar and micrite (Supplementary Figure 16a). Most sediments are massive with no clear sedimentary structures except for the sediments in PD16 (40-70 cm) which show evidence for finely laminated calcite, with laminations reflecting alternations between fine-grained micrite, coarser microspar and organics (Supplementary Figure 16b). Towards the top of PD17 laminations of allogenic quartz grains occur but these are infrequent (30-40 cm). Where quartz grains occur, their surfaces show signs of etching and replacement with calcite.

Organic remains are present in either an amorphous form or showing clear signs of cellular preservation. Diatoms and sponge spicules are visible in many slides (Supplementary Figure 16c) and the latter are typically most abundant at the sample levels with the lowest % carbonate values. Iron staining occurs towards the top of PD15 (40-50 cm) and towards the base of PD16 (0-10 cm). There is no evidence for neomorphism and negligible evidence for pore-infilling of secondary cement.

5.1.3 $\delta^{18}O$ and $\delta^{13}C$ analysis

The $\delta^{18}O$ and $\delta^{13}C$ values of the sub-samples from the four sampling locations (PD15, 16, 17 and 40) are shown in Supplementary Figure 17 Data from all four sections show very similar

$\delta^{18}O$ values), although there is a significant scatter in each dataset. Greater variation occurs within the mean $\delta^{13}C$ values, although the standard deviations of each dataset are again large. Although the dataset from each sampling locality is small PD15 (n = 8), PD 16 (n = 15), PD17 (n = 7) and PD40 (n = 12) it is sufficient to show the following patterns: 1) there is no co-variance in $\delta^{18}O$ and $\delta^{13}C$ values at any site or within the whole dataset level (r^2 ca 0.2) and 2) there is no consistent pattern of variation upwards through the profiles. With regard to the second point, while there is a clear trend at site PD40 of increasingly positive values upwards through the profile the reverse is true of PD16. Interpretation of these conflicting signals is problematic because it is unclear whether the deposits in each sequence are absolutely contemporaneous. One sample of calcite rhizolith was analysed from the calcrete capping PD40. This sample has the highest $\delta^{18}O$ value of the dataset, but it is the $\delta^{13}C$ value that is most significant as the high value (-1.12‰) implies that the vegetation that became established after the lake basin infilled/desiccated was a C4 grassland.

5.1.4 Diatoms

The diatom flora at PD15 and PD16 are shown in Supplementary Figures 18 and 19. Both sites show very similar species assemblages. The diagrams are divided into statistically significant zones based on a comparison with the broken-stick model using the program BSTICK version 1[52]. The species diagrams of each site can be divided into three statistically significant zones, the main characteristics of which are outlined below, along with the main environmental implications of these assemblages:

PD15

Zone I

This zone comprises planktonic species (*Lindavia rossi, Cyclotella krammeri* and *Lindavia ocellata*) which is illustrated by the high planktonic: benthic ratio. The CA and DCCA axis 1 scores decrease slightly in this zone. The log concentration, however, increases in this section meanwhile there is a minor decrease in the F index.

Zone II

This section reflects a change in species from mainly planktonic taxa to an increase in benthic taxa (*Cymbella affinis* and *Nitzschia angustata*) and periphytic (*Staurosirella lapponica* and *Ulnaria ulna (agg.)*). The increase in benthic and periphytic taxa is notable in the habitat composition diagram. The CA and DCCA axis 1 sample scores both decline considerably. There is also a decrease in the log concentration and the F index remains low.

Zone III

Aulacoseira italica and *Aulacoseira granulata* are the dominant taxa of this zone. The sample at 40 cm does not contain any benthic taxa therefore the planktonic: benthic ratio cannot be calculated for this level which is reflected in the habitat composition diagram. There is an increase in the CA axis 1 sample scores meanwhile a decrease in the DCCA axis 1 sample scores and log concentration occurs. The F index, which is a dissolution index, shows that the level of preservation is high for this sample in comparison to the rest of the profile.

pH

The assemblage reflects increasing pH as *Lindavia ocellata* usually occurs in mesotrophic lakes[53], whereas *Staurosirella lapponica, Stephanodiscus hantzschii, Aulacoseira granulata* and *Aulacoseira italica* are indicative of eutrophic lakes[54,55]. *Staurosirella lapponica* and

Stephanodiscus hantzschii are good indicators of high alkalinity lakes meanwhile *Aulacoseira granulata* and *Aulacoseira italica* are characteristic of carbonate rich lakes.

Lake depth

The planktonic: benthic ratio and the habitat summary show that zone I is the deepest as planktonic (e.g. *Lindavia rossi* and *Cyclotella krammeri*) and tychoplanktonic (e.g. *Lindavia ocellata*) taxa increase to reach a peak at 0cm[56,57]. The proportion of periphytic taxa increases throughout the zone II meanwhile benthic (e.g. *Cymbella affinis* and *Nitzschia angustata*) taxa reach a peak at 20 cm suggesting a decline in water depth which remains low for the remainder of the sequence. *Aulacoseira italica* and *Aulacoseira granulata*, which are periphytic and planktonic taxa respectively, dominate in zone III. *Aulacoseira granulata* suggests that lake levels were quite shallow5[58] up to a few metres and quite turbulent[55,59]. *Aulacoseira italica* accounts for 65% of the assemblage at 40 cm also suggesting shallower conditions as the habitat summary shows that this level comprises of periphytic and planktonic taxa with a small proportion of taxa with unknown ecology.

Salinity

There are very few saline tolerant species except for *Epithemia argus* which can be found in harsh conditions from saline to high alkaline, nutrient poor conditions. Due to its low abundance and the lack of other saline species salinity is not a major driver of this assemblage.

Phosphorous

The taxa (*Lindavia rossi, Cyclotella krammeri* and *Cyclotella ocellata*) show increasing nutrient enrichment from a mesotrophic lake, which suggests moderate phosphorous concentration to eutrophic conditions with high phosphorous concentrations characterised by *Stephanodiscus hantzschii*, *Aulacoseira granulata* and *Aulacoseira italica*[56-59].

PD16

Zone I

Stephanodiscus and *Aulacoseira* are the dominant taxa in this zone with small increases in *Fragilaria delicatissima, Staurosirella lapponica* and *Cymbella affinis*. There is an increase in the planktonic: benthic ratio at the 10 cm which remains stable until zone II. The PCA and DCCA axis 1 scores diverge at 0 cm; however, both show little change meanwhile the log concentration and the F Index both increase until 10 cm before decreasing.

Zone II

There is a large decline in *Aulacoseira italica* in this section, while a decrease in the periphytic taxa occurs with a contemporaneous increase in benthic taxa. The PCA axis 1 scores remain stable; meanwhile there is an increase in the DCCA axis 1 sample scores, fluctuations in the log concentration and an increase in preservation in this zone.

Zone III

Lindavia rossi, Cyclotella krammeri and *Lindavia ocellata* are the predominant taxa of this zone; however, *Aulacoseira italica and Lindavia ocellata* are the main taxa at 70 cm. The reduced abundance of benthic taxa is reflected by the increased planktonic: benthic ratio. The PCA and DCCA axis 1 sample scores also illustrate the change in composition. The log concentration and F Index both follow the same trend and decrease overall in this section.

pH

The assemblage shows generally declining pH from *Stephanodiscus hantzschii, Stephanodiscus parvus, Aulacoseira angustata, Staurosirella lapponica, Aulacoseira italica, Cymbella affinis, Lindavia ocellata, Cyclotellla krammeri* and *Lindavia rossi*. The interaction of other variables, for examples, depth, light and phosphorous can also affect the abundance of different taxa[56,61]. The taxa present in zones I and II are associated with higher pH consistent with lower water levels which can concentrates the pH. In zone III the taxa changes and reflects lower pH conditions coherent with higher water levels which dilutes the pH level and other nutrients[62,63].

Lake depth

The planktonic: benthic ratio and habitat summary shows that zone I and II consists of mainly benthic taxa and periphytic taxa suggesting lower water levels. Zone III comprises of mostly planktonic and tychoplanktonic species, indicating higher water levels. The PCA and DCCA axis 1 sample scores both show a big change in the composition and, over time, of the assemblage, reflecting the change in water level.

Salinity

Epithemia argus is the only saline species present in the diagram which indicates that assemblage is not significantly influenced by salinity.

Phosphorous

The response to nutrient enrichment, which is usually linked to phosphorous, follows the same trend as pH of decreasing nutrient status as reflected by the declining nutrient tolerant

taxa. Nutrient cycling within the lake is also affected by other variables (e.g. depth, light and pH) thus in zones I and II where there is lower water depth the phosphorous concentration increases enabling *Stephanodiscus hantzschii* and *Aulacoseira granulata* to thrive. Conversely in Zone III the assemblage consists of species with a low threshold for phosphorous which suggests a higher water level as the phosphorous becomes more dilute[62,63].

The overall change in the diatom assemblages can be assessed by the changes in the species composition of the sample (PCA or CA) and over time between the samples (DCCA). CA was used in PD15 which shows that there are substantial changes from 20 cm to the top of the core as the exploratory DCA axis 1 gradient length was ≥1.5 SD units. The DCCA also shows a corresponding high species turnover which suggests a large change in species composition between samples which the decrease in the planktonic:benthic ratio reflects. PCA was used in PD16 (gradient length of exploratory DCA was ≤1.5 SD units) that shows there are smaller species compositional changes within this site than PD15. The largest change occurs between 40-50 cm at PD15 which is simultaneous with a change in taxa reflected by the sudden increase in the DCCA axis 1 sample scores and the planktonic: benthic ratio. Although the changes appear larger in PD15 there are caveats to consider; the small sample size of 5 samples at this site may not be as representative of the environment as a larger dataset so the results may change if more samples were analysed at more frequent intervals. The planktonic:benthic ratio of PD15 is smaller than that of PD16 suggesting less fluctuation in the water level.

5.2 Interpretation

The proxy data outlined above allows the environment and hydrology of the Al Wusta lake beds to be reconstructed. This has implications for both the environment of the site itself but also for the regional palaeoclimate of the time.

5.2.1 Environment and hydrology of the Al Wusta lake beds

The loose and cross-bedded nature of the sands of Unit 1 are typical of aeolian dune sands and indicate that, prior to carbonate accumulation, the Al Wusta site was affected by active dune migration. Unit 2, characterised by massive carbonate beds and their microfabrics, is typical of the accumulation of authigenic carbonate marl on the bed of a lacustrine environment[64,65]. The precipitation of carbonate in the water column and its deposition out of suspension leads to the development of fine-grain marl beds. The structureless character of the beds is indicative of shallow water resulting in the sediment being oxidised and consequently bioturbated, or exposed to water column turbulence by surface winds. The preservation of laminations within PD16 most probably relates to short-term episodes of deeper water or more rapid rates of sedimentation. Despite being shallow there is no sedimentary evidence to indicate that the lacustrine environment underwent desiccation, as there is a complete absence of surface exposure features, and the character of the sediments are consistent throughout the entirety of the bed[64]. The shallow nature of the water is supported by the diatom assemblage which contains significant proportions of *Aulacoseira italica* and *Aulacoseira granulata* which indicates a few metres of water depth, with the latter being indicative of turbulent water conditions. While changes in the plantktonic/benthic ratio of the diatom assemblage suggest progressive changes in water level there is no evidence to indicate that the water level dropped to sub-aerially expose the lake beds. Consequently, the beds record the existence of a perennial water body.

The diatom flora is dominated by freshwater species with negligible evidence for salinity tolerant species. The lake was, therefore, a freshwater environment; an interpretation supported by the dominance of calcite in the lake XRD mineralogy traces and an absence of evaporitic minerals such as halite and gypsum.

A lack of covariance in $\delta^{18}O$ and $\delta^{13}C$ values is often used to indicate whether a lake basin was part of an open system (i.e. a system with an active inflow and outflow to the basin) or not. Generally, the absence of co-variance is indicative of open-system lake waters that are regularly recharged; this has the effect of limiting any in-basin modification of the isotopic signal by processes such as evaporation[66]. Such a scenario could be true of the Al Wusta lake beds as the persistence of freshwater conditions (as evidenced by the diatom assemblages) and the lack of evaporative minerals would indicate that this system never underwent sufficient evaporation to produce brackish or saline conditions. However, two points are important to consider here. Firstly, a number of studies exist that report closed lake systems that do not show co-variance in their isotopic signals[67]. The exact cause of this is not always clear, however, it highlights the fact that the absence of $\delta^{18}O$ and $\delta^{13}C$ co-variance at Al Wusta should not be used as definitive evidence of this site recording an open lake system. Secondly, it is important to acknowledge that, even when there is no isotopic covariance, the $\delta^{18}O$ of the water in open system lakes can still become enriched as a result of the evaporation of surface waters. However, as such systems have regular recharge this does not result in the waters becoming brackish or saline[68]. This is an important point as it is impossible to say whether minor or major evaporative enrichment in lake $\delta^{18}O$ water values occurred at Al Wusta, but the diatom and mineralogical evidence shows that if such evaporation did occur, it was not sufficient to cause the waters to become brackish.

In summary, the proxy evidence indicates that Unit 2 represents the deposition of marl in a perennial water body that was entirely fresh. At this time the Al Wusta lake basin was an accessible and permanent freshwater resource for any early humans in the region. The pattern in the $\delta^{18}O$ values seen at site PD40 (an increase in $\delta^{18}O$ values upward through the sequence) could reflect a trend to greater aridity during the accumulation of this sequence (with increasing values reflecting greater evaporation and hence greater aridity). However, as the reverse is true for PD16 it is difficult to know how robust this interpretation is.

The mean $\delta^{18}O$ values of this sequence (-2.4 to -1.9‰) reflect both the $\delta^{18}O$ value of the lake water and the temperature at which carbonate precipitation occurred[66]. Both of these are unknown, however, the nearest local isotopic datasetindicates that modern rainfall has a $\delta^{18}O$ value of -4.0 to -4.5‰[69]. If such values occurred at the time of marl development at Al Wusta then it is likely that either the temperature of mineralisation was surprisingly low (i.e. a carbonate with a mean $\delta^{18}O$ value of -2.2‰ precipitating from water with a mean $\delta^{18}O$ value of -4.25‰ would form in isotopic equilibrium at a temperature of ca 11^{o}C) or that significant isotopic enrichment, through evaporation, of the lake water had occurred. It is also important to consider, however, that the modern climate system that generates rainfall with a value of -4.0 to -4.5‰ is a function of a westerly dominated system. As most humid phases in the Arabian Peninsula are suggested to relate to increased monsoon strength[70], it is likely that the $\delta^{18}O$ value of the rainfall during the formation of the lake system at Al Wusta was significantly different, and most likely heavier, than modern day values. A strong south to north gradient in the $\delta^{18}O$ value of modern rainfall appears to exist in Arabia in the present day, with values in the southern part of this region being >0‰ in contrast with those in the north that are around 4‰[71]. Only a small northward shift in the air masses bringing rainfall

from a southerly source would, therefore, produce a significant increase in the $\delta^{18}O$ value of rainfall at Al Wusta.

Consequently, it is currently unclear whether the marl $\delta^{18}O$ value of ca -2.2‰ is a function of low water temperatures, isotopic enrichment, different air mass trajectory or a combination of all of these factors. Although many of the artefacts and fossils are found within Unit 3 it is important to stress that *in situ* artefacts are found with Unit 2 implying that humans were present in the landscape during the existence of the perennial freshwater lake body.

The deposits of Unit 3a are interpreted as waterlain sands based on the presence of freshwater molluscs, the horizontal laminations and the incorporation of ripped up fragments of the underlying marl. The sands are interpreted as reflecting the encroachment of fluvial sedimentation during the final phase of basin infilling, either as a result of desiccation or simply due to the progressive reduction in available accommodation space. It is considered that the former is more likely as the inclusion of ripped up marl fragments would imply that the upper surface of Unit 2 had dried out and fragmented prior to the deposition of Unit 3a. The waterlain sands are capped by a horizon of calcified rhizoliths that represent the final transition from sub-aqueous to terrestrial conditions at the site. The coarse surface lag (Unit 3b) reflects the winnowing of Unit 3a by aeolian processes and the formation of a desert pavement. The relatively resistant nature of the rhizolith horizon makes this layer resistant to aeolian erosion resulting in the occurrence of these features as a cemented cap at the top of the sequence.

The majority of the excavated Al Wusta artefacts and fossils are found in Unit 3a. As the sediments of this unit contain evidence of eroded and reworked marl from Unit 2 it is

possible that the archaeological and faunal material has been derived from Unit 2 and reworked into the fluvial sands. If this is the case then it supports the idea that human occupation at the site is associated with the existence of a perennial, freshwater lake. If the artefacts and fossils are *in situ* then it implies that occupation of the site must have persisted after the contraction of the lake basin and the desiccation of the water body.

5.2.2. Implications of the Al Wusta sequence for regional palaeoclimate

The proxy record of the Al Wusta sequence records the existence of a perennial, freshwater lake system. Regarding human migration into this region, it is important to establish whether the existence of such a system can be explained by local hydrogeology or by increased regional moisture (i.e. the occurrence of a humid phase). It is argued here, despite evidence from only a single site being presented, that an increase in mean annual precipitation is required to explain the development of the Al Wusta lake basin. This suggestion is based upon three main observations. Firstly, the fact that Unit 2 comprises well-developed marl beds means that the lake waters must have been fed by groundwater recharge. The presence of sufficient dissolved Ca^{2+} in the lake waters to produce extensive marl precipitation requires migration of the waters through an aquifer. While much of the underlying geology is quartz rich sands, these are interbedded with units of carbonate rich marls that reflect phases of lake activity that pre-date the formation of the Al Wusta sequence. It is likely that these beds are the source of the dissolved minerals that fed into the Al Wusta basin. Secondly, no groundwater fed lake systems currently exist in the Nefud as the water table is too low. Surface water bodies are, therefore, restricted to highly ephemeral recharge playas. Thirdly, the underlying sediments and bedrock in this region are highly permeable aeolian sands; no local impermeable strata exist that could generate a locally perched water table that would

explain the existence of a lake system at this site. It is, therefore, proposed that the genesis of a groundwater fed lake system at this locality requires a regional increase in mean annual rainfall and the persistence of a humid phase in the Nefud Desert.

5.2.3 Summary

The Al Wusta sequence records the evolution of the site across an entire humid phase from aeolian deposition (Unit 1) to the development of lacustrine conditions (Unit 2) to the progressive drying out of the lake basin and the reversion to terrestrial conditions (Units 3a and b). In particular, the diverse range of proxies discussed here indicate that the Unit 2 carbonate deposits at Al Wusta were deposited in a perennial shallow (a few metres of water depth) alkaline lake environment. This lake water body formed as a result of a humid phase and was fresh throughout its existence, making it a major resource for humans and fauna during this interval.

SI 6. Al Wusta vertebrate palaeontology, biogeography and taphonomy.

The Al Wusta vertebrate fossil assemblage (Supplementary Table 19; Supplementary Figure 19) is very fragmented, with few complete bones recovered. Fossil weathering is extensive and much of the cortical surfaces of the bones are missing, making skeletal element and taxonomic identification difficult. Of the 860 specimens, 305 are identifiable to skeletal element, with long bone shafts most common (Supplementary Table 20). Of the 12 distinct taxa identified, medium-sized bovids are most abundant, followed by small-sized bovids and *Hippopotamus*. *Hippopotamus* is represented solely by incisor and tusk fragments recovered *in situ*. *Kobus* sp. is represented by partial right M_2 and M_3 teeth (Supplementary Figure 20). The M_3 has a distally positioned lingual accessory cusp, simple and flattened U-shaped infundibulum, and a rounded buccally projecting hypoconulid. The occlusal length is within the range of *K. ellipsiprymnus*; nevertheless, the specimen is too fragmented to allow positive species identification. Rodentia is represented by two specimens, a maxilla fragment missing all molars, and an almost complete cranium including part of the mandible. Despite the completeness of this specimen, it is distorted, fragile and partially covered in matrix, making a more precise taxonomic identification difficult. Two isolated reptile teeth belonging to a species of *Varanus* were identified. The presence of *Struthio* is confirmed by numerous egg shell fragments recovered *in situ*. Additionally, two smaller-bodied species of birds are represented by incomplete long bone fragments.

While *Hippopotamus* is restricted to Africa today, during the Pleistocene it was common throughout parts of Europe and Asia[72,73]. Dispersals out of Africa led to localised speciation events in Europe and the Levant[74]; however, there is some debate surrounding the precise number of *Hippopotamus* species[75,76]. While it seems likely that the Al Wusta specimens

represent an out of Africa dispersal, it should be noted that *H. amphibius* has been identified at sites in Britain and Central Europe dated near the Middle to Late Pleistocene transition[72,77,78]. *Pelorovis* is common in East Africa throughout the Pleistocene and is also found at a few sites in North Africa but is absent from Europe and the Levant after the Early Pleistocene[79-81]. Both *Pelorovis* and *Hippopotamus* have been identified at other sites in Saudi Arabia[82,83] suggesting repeated dispersal events into the Arabian Peninsula during periods of climate amelioration. *Kobus* typically inhabit flood-plains and grasslands bordering water[84]. During the Middle and Late Pleistocene *Kobus* was restricted to Africa and mostly south of the Maghreb. Notable northern occurrences were reported from Algeria and Egypt, associated with the Last Interglacial[85,86], but is unknown from the Levant during this period. This may support a tendency toward longitudinal dispersals[87], in this case eastward dispersal out of Africa and into the Arabian Peninsula via the Southern Levant. *Struthio* is common in Africa, but has also been identified by eggshell fragments on the Indian subcontinent from as early as the Middle Miocene and as recently as 18 ka[87,88]. *Struthio* has been found at several sites in the Levant, and was extant in Southwest Asia until the 20th century.

Weathering of many specimens, particularly those collected from the surface at the western edge of the southern ridge at Al Wusta, suggests that they were likely exposed for a significant period of time post-fossilisation, with abrasion and polishing attributable to aeolian processes. Surface fossils included several refits recovered in close proximity, suggesting limited post-exposure transport. It is likely that such specimens became concentrated on the surface as a result of winnowing of the main fossiliferous layer. For these specimens, post-mortem weathering (i.e. prior to fossilisation) was impossible to determine due to the extensive fossil weathering of the cortical surfaces (i.e. following fossilization).

Specimens collected *in situ* were typically better preserved and lacked the abrasion and polishing common to the specimens from the surface. Pre-depositional weathering of these remains, on the other hand, was difficult to determine due to the fragmentary nature of the fossils and the fact that many specimens remain encrusted in carbonate. Despite the absence of large-bodied mammalian carnivores in the fossil assemblage, tooth pits potentially attributable to hyenas, large canids, or large felids are evident on some bones (Supplementary Figure 20H; Supplementary Table 21). Manganese staining is also present on numerous specimens. Two small bone fragments may have been burnt: one is blackened and the other one is dark brown in colour. However, their preservation is too poor to confidently rule out diagenetic discolouration. No additional bone surface modifications were observed, although this was not surprising considering that fine scale modifications are likely to have been removed during weathering.

Analysis of long bone circumference revealed a majority of type 1 shafts (75%), with type 2 and type 3 occurring much less frequently (12% and 13%, respectively). The type 3 and type 2 to type 1 index is 0.31, falling within the typical range identified for assemblages accumulated by carnivores and hominins[89]. While extensive fossil weathering may also have contributed to the production of type 1 shafts; nevertheless, there is evidence for large carnivores and hominins at Al Wusta and it is likely that they contributed to the production of type 1 shafts during prey processing and consumption. Furthermore, the under-representation of epiphyses (N = 11) at Al Wusta supports carnivore ravaging of long bone ends[90] although this may also be an artefact of other non-biological preservation biases. Additional support that bone breaking agents were, at least in part, responsible for the accumulation of bones is the presence of green breaks (N = 12). Unfortunately, the assemblage is too poorly preserved to determine a primary accumulator.

SI 7. Al Wusta lithic technology.

7.1 Introduction

The Al Wusta lithic (stone tool) assemblage consists of 380 artefacts, systematically collected in transects and piece plotted from the southern end of the site in close proximity to the marl beds and from excavations in 2016 and 2017 (Figure 1). Lithics continued to the north, but were not included in the analysis here, which is limited to material south of the Holocene playa (Figure 1). The assemblage is Middle Palaeolithic in its characteristics, with a focus on centripetal Levallois reduction, particularly of chert and quartzite. Retouched tools are predominantly side-retouched flakes. The lithics, all from the same spatially restricted area, also display similar raw materials, weathering and technology and are therefore treated here as a single assemblage. The Al Wusta lithic assemblage is a valuable reference point for late MIS 5 Arabia, and displays similar technological features to other contemporary Arabian asssemblages[43,91-93].

The Al Wusta lithic assemblage can be divided into the following categories (% in brackets shows % of total assemblage): 229 flakes (60.20%) [of which 36 are Levallois flakes, 9.47%], 55 chips and chunks (14.47%), 21 retouched flakes (5.52%), one hammerstone (0.26%), and 74 cores (19.47%). Our aim here is to describe the basic technological characteristics of this lithic assemblage, which we analysed using the methodology and terminology described by Scerri and colleagues[94-96] and Groucutt and colleagues[93,97].

The surface lithic assemblage was found closely associated with the marl deposits. Eleven lithics were excavated at the site, in the upper part of the marl and in the overlying *in situ*

sand layer. The excavated material demonstrates similar characteristics to the larger sample from the surface, and includes similar raw material (focus on local lacustrine chert), three Levallois cores, flakes with facetted platforms and a debordant flake. The density of lithics on the surface, together with the considerable variation in their size suggests that they are not extensively redeposited, and we suggest that they were made by hominins beside the late MIS 5 lakeshore and then deposited into the lake by gravity and low energy movement.

7.2 Raw materials

In terms of raw material composition, the most common material consists of a local lacustrine chert (65.09%), followed by quartzite (17.59%), ferruginous quartzite (11.02%), quartz (5.25%), argillaceous sandstone (0.52%), and other sandstone (0.52%). This raw material structure is unusual for the area. Al Wusta is the only identified Middle Palaeolithic assemblage in the region not dominated by quartzite, generally highly ferruginized[91,92,97-99]. It appears that suitable quartzite is rare in the environs of Al Wusta, with our survey of the area showing an absence of large beds of ferruginous quartzite (Figure 5c). Non-ferruginous forms of quartzite (e.g. Figure 5f) are relatively common in the assemblage, and appear to occur as rounded pebbles of fluvial or conglomerate origin. Aside from chert, other materials occur in low frequencies, such as quartz **(**Figure 5e), which occurs as small pebbles in the bedrock of the area, and a rare type of rock which can be described as argillaceous sandstone[99] (Figure 5A).

The dominant raw material consists of chert, which occurs with varying colours and textures. The most common is brown in colour (e.g. Figure 5d). Our surveys of the area show that this material has formed in lakebeds in the area, which form a raw material source when exposed

by subsequent erosion. We have conducted knapping experiments with this raw material, which shows that while variable, it is difficult material for knapping. The dominant chert at Al Wusta seems to be a particular poor quality form. The chert clasts are relatively small (always smaller than fist sized), have a very thick and undulating cortex, and frequently have inclusions. The material is also extremely hard, and has to be struck with considerable force to remove a flake. Despite these limitations, if knappers could access the inner part of the nodules, the chert is fine grained and appears to have reasonable properties of conchoidal fracture.

7.3 Core technology

The 74 residual Al Wusta cores are dominated by Levallois cores (54, 73%), with smaller numbers of non-Levallois multiple platform cores (12, 15.6%), double platform (bidirectional) cores (two, 2.7%), single platform cores (two, 2.7%), tested/minimally flaked cores (two, 2.7%), one radial core (i.e. a core flaked centripetally, but which is neither Levallois nor discoidal) (1.4%), and one core fragment (1.4%). It is clear, therefore, that reduction was dominated by use of the Levallois technique. Other methods appear more ad hoc in character. Multiple platform cores, for instance, tend to be small, having a mean weight of 19.3 g if one large outlier weighing 349.9 g is removed. This compares to the average weight for all cores of 34.9 g (with the same outlier also excluded). This suggests that multiple platform core reduction, the main non-Levallois reduction method, was employed on small clasts and/or on heavily reduced cores, which may have been Levallois cores earlier in reduction. There is no evidence of façonnage reduction, nor of blade production.

Of the 54 Levallois cores, 36 (66.7%) are preferential Levallois cores with centripetal preparation (e.g. Supplementary Figure 21a,b,d) and 13 (24.1%) are recurrent centripetal Levallois cores (e.g. Supplementary Figure 21C). The small number of pieces not in these categories are indeterminate Levallois cores where overshot removals have removed the whole debitage surface (9.2%). From the geometry of the cores and the morphology of platform surface these are clearly centripetal Levallois cores, but it is not clear if their final phase of reduction was recurrent or preferential in character. Finally, one example each of recurrent unidirectional and recurrent bidirectional Levallois cores were identified. Striking platforms are facetted on 87% of the Levallois cores. In most cases preferential scars on Levallois cores demonstrate the product of parallel sided and sometimes oval Levallois flakes, with a small number producing pointed products.

Preferential and recurrent cores are similar in many features, for instance they have a similar number of scars (average of 12.9 and 10.9 respectively) and a similar percentage of cortical cover (23% and 27%). However, in terms of size recurrent cores are typically smaller (14.3 g, σ 9.0) than preferential cores (36.9 g, σ 42.7). These data indicate that, as a general pattern and perhaps within a situation of interchangeable reduction between Levallois methods, larger cores were reduced preferentially and a recurrent method was used late in reduction. The predominant focus on centripetal Levallois reduction demonstrates a level of homogeneity to core reduction at the site.

7.4 Debitage

Lithic debitage (n=284) at Al Wusta can be classified as complete flakes (185, 65.1%), broken flakes (44, 15.5%) and chips/chunks (55, 19.4%). Our description here focusses on complete flakes.

The average length (technological), width (mid-point), thickness (mid-point), and weight of complete flakes are 29.8 mm (σ 11.9), 24.5 mm (σ 9.2), 8.46 mm (σ 4.2), and 13.1 g (σ 16.3) respectively. To aid comparability, if we exclude flakes which are less than 20 mm in length, these values become 32.25 mm (σ 11.3), 25.7 mm (σ 9.4), 9.3 mm (σ 4.3), and 14.6 (σ 16.9).

Other basic features for complete flakes >20 mm in length include an average cortical cover of 16.5% of the debitage surface, an average of 2.8 dorsal scars (σ 1.7), striking platforms are prepared (facetted or dihedral) in 41.6% percent of cases and striking platforms have average external platform values of 74.9° (σ 6.2). Dorsal scar patterns can be classified as: 31.5% unidirectional, 2.4% unidirectional convergent, 1.6% perpendicular, 3.1% crossed, 11.8% bidirectional, 13.4% subcentripetal, and 36.2% centripetal.

Complete Al Wusta Levallois flakes (e.g. Supplementary Figure 21E,G-K) are on average 33 mm in length, 25.5 mm in width and 7.4 mm thick. They are generally broadly parallel sided in shape. They most commonly (64.5%) have centripetal scar patterns, with a further 12.9% having subcentripetal scar patterns. The remaining Levallois flakes are characterised by unidirectional scar patterns (16.1%) and unidirectional convergent (6.5%). 74.2% of the Al Wusta Levallois flakes have prepared platforms.

Summarising these data, Al Wusta flakes are therefore typically small, quite commonly cortical and with various scar patterns but particularly unidirectional and centripetal. Levallois flakes are also small, and indicate a tendency to produce Levallois flakes by centripetal preparation and hard hammer percussion from prepared platforms. These

characteristics are consistent with the evidence from the cores in indicating that lithic technology at Al Wusta is focussed on centripetal Levallois reduction.

7.5 Retouched flakes

A total of 21 retouched flakes were found at Al Wusta (15 complete). Three of these have only distal retouch (e.g. Supplementary Figure 21m), seven are retouched along one lateral (e.g. Supplementary Figure 21n), seven are retouched on both laterals (e.g. Supplementary Figure 21l), and two are retouched on both laterals and distally (two more are fragments). Where it can be determined, 87.5% of striking platforms are facetted or dihedral.

Of the complete retouched pieces, they are mostly parallel sided and 66.7% have either cortical surfaces or unidirectional scar patterns. Their average length, width, thickness and weight are 33.6 mm (σ 11.5), 24.34 mm (σ 12.4), 10.7 mm (σ 2.4), and 15.9 g (σ 2.4). These are similar values to the overall flake population.

In most cases retouch is 'regular', while 33% of retouched flakes have notches as well as regular retouch. In all but one case, the retouch is continuous rather than clustered, and virtually all of the retouch is semi-abrupt. Retouch is always found on either the dorsal surface or on both surfaces, and never exclusively on the ventral surface. Index of Invasiveness (I of I)[100], values range from 0.094 to 0.5, averaging at 0.25. Geometric Index of Unifacial retouch (GIUR)[101] values range from 0.45 to 0.89 with an average of 0.69. The quite low values for I of I and high values for GIUR demonstrates that retouch was not horizontally extensive across the face of the flakes, but was vertically quite intensive.

The retouched component of Al Wusta therefore shows a focus on typical side retouched flakes ("scrapers") with prepared platforms, as is commonly the case for Middle Palaeolithic assemblages.

7.6 Al Wusta lithic technology in comparative context

The lithic assemblage of Al Wusta demonstrates a consistent approach to lithic technology, focussed on centripetal Levallois technology. Here we will briefly consider this technology in relation to sites elsewhere in Arabia and surrounding regions.

The corpus of Arabian sites which can be related to later MIS 5 by chronometric dating techniques is small, but increasing. These include the ~75 ka assemblage at JQ-1 at Jubbah[43,91], the ~ 100-60 ka assemblage from JSM-1 at Jubbah[91,95], and the ~85 ka assemblage from Mundafan Al Buhayrah in southwestern Arabia[93]. We emphasise the latter assemblage from Mundafan as the key example, with both good chronometric age estimates and a large and diagnostic lithic assemblage. Most Arabian Middle Palaeolithic assemblages remain undated, or have produced contradictory age estimates, which mean little can be said on their age with certainty. The available chronologically secure data indicate that mid to late MIS 5 sites demonstrate a focus on centripetal Levallois reduction, with both centripetally prepared preferential and recurrent centripetal Levallois methods employed. In all cases they lack bifacial façonnage technology and beaked ('Nubian') Levallois reduction. Levallois point production only occurs at marginal levels. Differences at these sites tend to correlate with raw material aspects. Both MDF-61 and JQ-1 appear to be located far (>10 km) from good raw material sources, and in both cases demonstrate highly reduced assemblages, both in terms of core reduction and high levels of retouch[93,99]. In terms of size aspects, lithics at Al

Wusta are relatively small for MP/MSA assemblages. They are much smaller than many Arabian sites, but also not as small as sites with highly reduced assemblages elsewhere in southwest Asia, such as Tor Faraj in Jordan and Warwasi in Iran[93,97,102]. We associate these small size aspects primarily with raw material factors at Al Wusta. The relatively high levels of retouch at Al Wusta likewise likely correlate with the limitations of raw material in the area, encouraging resharpening/edge rejuvenation of existing pieces.

In areas to the north and west of Arabia a number of assemblages date to mid to late MIS 5 and share similar technological characteristics with Al Wusta. In the Levant this is most clearly demonstrated by Qafzeh Cave, with its famous *Homo sapiens* fossils, dating to ~100-90 ka[101]. Moving into northeast Africa, sites such as 1017 and 34a have been attributed to later MIS 5 (~85-80 ka) on both stratigraphic grounds and with preliminary chronometric age estimates[104-106]. The technology of these sites again demonstrates a focus on centripetal Levallois reduction. The Bir Tarfawi and Bir Sahara palaeolakes feature broadly similar technology, and were repeatedly occupied during the wet phases of MIS 5[107]. In the Horn of Africa key evidence comes from a series of dated assemblages in the Aduma area[108]. These date to between ~100 and 80 thousand years ago, and as with sites such as Al Wusta demonstrate a focus on the centripetal reduction of small Levallois cores, and are also associated with *Homo sapiens* fossils. While these sites feature similar core reduction methods, in contrast to, for example, the unidirectional focus of MIS 4-3 Neanderthal assemblages in southwest Asia, further research is needed to understand similarities and differences in areas such as retouched tool technology.

While traditionally masked by variable analytical methodologies, differing regional nomenclatures and a lack of knowledge on areas such as Arabia, we interpret these findings

as indicating broad technological similarities across a large area in mid to late MIS 5[110]. However, East African sites appear to feature more of a focus on retouched point production (although this must be matched against these sites having large sample sizes compared to assemblages in places such as Arabia). In terms of core reduction methods, however, assemblages in East Africa, northeast Africa, the Levant and Arabia all appear to be similar in mid to late MIS 5. In line with available fossil evidence, we note that this pattern appears to be most ancient in East Africa[108,109]. In contrast to East Africa, areas such as the Nile Valley, the Levant and Arabia demonstrate highly variable MP/MSA records. This pattern suggests that at least in terms of visible (archaeologically preserved) aspects of material culture, the earlier phases of dispersal into southwest Asia did not relate to radical technological innovation. Phases of dispersal correlate with windows of climatic amelioration in the Saharo-Arabian arid belt, while further research is needed to understand the nature of demographic, social and behavioural changes in sub-Saharan Africa which might have triggered dispersals. Beyond these broad observations of similarities in contemporaneous similarities, detailed comparative studies of chronometrically constrained lithic assemblages are needed to clarify patterns of similarities and differences in lithic assemblages.

Supplementary References

1. Martinez-Navarro, B., *et al*. Early Pleistocene “hominid remains” from southern Spain and the taxonomic assigment of the Cueva Victoria phalanx. *J. Hum. Evol.* **48**, 517-523 (2005).
2. Martinez-Navarro, B, *et al*. Reply to Gilbert et al. (2008) on the supposed human phalanx from Cueva Victoria (Cartagena, Spain). *J. Hum. Evol*. **54**, 157-161 (2008).
3. Ruff, C. B. Body size, body shape, and long bone strength in modern humans. *J. Hum. Evol.* **38**, 269-90 (2000).
4. Pearson O. M, Lieberman D. E. The aging of Wolff's "law": ontogeny and responses to mechanical loading in cortical bone. *Am. J. Phys. Anthropol.* **125**, 63-99 (2004)
5. Ruff, C., Holt, B., Trinkaus, E. Who's afraid of the big bad Wolff?: "Wolff's law" and bone functional adaptation. *Am. J. Phys. Anthropol.* **129**, 484-98 (2006).
6. Ruff, C. B., Trinkaus, E., Walker, A., Larsen, C. S. Postcranial robusticity in Homo. I: Temporal trends and mechanical interpretation. *Am. J. Phys. Anthropol.* **91**, 21-53 (1993).
7. Rasband, W. S. *ImageJ*. Bethesda, Maryland, USA: U.S. National Institutes of Health, http://imagej.nih.gov/ij/ (1997-2016).
8. Doube, M. et al. BoneJ: Free and extensible bone image analysis in ImageJ. *Bone* **47**, 1076-9 (2010).
9. Ruff, C.B. in *Biological Anthropology of the Human Skeleton* (Katzenberg M.A., Saunders, S.R.) 183-206 (Wiley, 2007).
10. Ruff, C. Sexual dimorphism in human lower limb bone structure: relationship to subsistence strategy and sexual division of labor. *J. Hum. Evol.* **16**, 391-416 (1987).

11. Shaw, C. N, Stock, J. T. Intensity, repetitiveness, and directionality of habitual adolescent mobility patterns influence the tibial diaphysis morphology of athletes. *Am. J. Phys. Anth.* **140**, 149-59 (2009).

12. Grün, R., Eggins, S., Kinsley, L., Mosely, H., Sambridge, M. Laser ablation U-series analysis of fossil bones and teeth. *Palaeogeogr., Palaeoclimatol., Palaeoecol.* **416,** 150-167 (2014).

13. Benson, A., Kinsley, L., Defleur, A., Kokkonen, H., Mussi, M., Grün, R., 2013. Laser ablation depth profiling of U-series and Sr isotopes in human fossils. *J. Arch. Sci.* **40**, 2991-3000 (2013).

14. Grün, R. Methods of dose determination using ESR spectra of tooth enamel. *Radiat. Meas.* **32**, 767-772 (2000).

15. Duval, M., Grün, R., Falguères, C., Bahain, J.J., Dolo, J.M. ESR dating of Lower Pleistocene fossil teeth: Limits of the single saturating exponential (SSE) function for the equivalent dose determination. *Radiat. Meas*. **44,** 477-482 (2009).

16. Duval, M., Guilarte Moreno, V., Grün, R. ESR dosimetry of fossil enamel: some comments about measurement precision, long-term signal fading and dose–response curve fitting. *Rad. Prot. Dosim*. **157**, 463-476 (2013).

17. Duval, M., Grün, R. Are published ESR dose assessments on fossil tooth enamel reliable? *Quatern. Geochron.* **31**, 19-27 (2016).

18. Grün, R., Katzenberger-Apel, O. An alpha irradiator for ESR dating. *Ancient TL* **12**, 35-38 (1994).

19. Marsh, R. E. *Beta-gradient Isochrons Using Electron Paramagnetic Resonance: Towards a New Dating Method in Archaeology.* (MSc thesis, McMaster University, Hamilton, 1999).

20. Guérin, G., Mercier, N., Adamiec, G.. Dose rate conversion factors: update. *Ancient TL* **29**, 5-8 (2011).

21. Grün, R. The DATA program for the calculation of ESR age estimates on tooth enamel. *Quatern. Geochron*. **4**, 231-232 (2009).

22. Grün, R., Schwarcz, H.P., Chadam, J. ESR dating of tooth enamel: Coupled correction for U-uptake and U-series disequilibrium. *Int. J. Radiat. Appl. Instrum. Nucl. Tracks. Radiat. Meas*. **14**, 237-241 (1988).

23. Duval, M. in *Encyclopaedia of Scientific Dating* (eds Rink, W.J., Thompson, J.W.) 239-246 (Springer, 2015).

24. Ludwig, K. R. *User's manual for Isoplot 3.75*. Berkeley Geochronology Center, Special Publication **5**, 1-75 (2012).

25. Sambridge, M., Grün, R., Eggins, S. U-series dating of bone in an open system: The diffusion-adsorption-decay model. *Quatern. Geochron*. **9**, 42-53 (2012).

26. Bøtter-Jensen, L., Andersen, C. E., Duller, G. A. T., Murray, A. S. Developments in radiation, stimulation and observation facilities in luminescence measurements. *Radiat. Meas*. **37**, 535-541 (2003).

27. Duller, G. A. T., Bøtter-Jensen, L., Murray, A. S. Combining infrared- and green-laser stimulation sources in single-grain luminescence measurements of feldspar and quartz. *Radiat. Meas.* **37**, 543-550 (2003).

28. Duller, G. A. T., Bøtter-Jensen, L., Murray, A. S., Truscott, A. J. Single grain laser luminescence (SGLL) measurements using a novel automated reader. *Nucl. Instr. Meth. Phys. Res.* **155**, 506-514 (1999).

29. Armitage, S., Bailey, R. The measured dependence of laboratory beta dose rates on sample grain size. *Radiat. Meas.* **39**, 123-127 (2005).

30. Ballarini, M., Wintle, A. G., Wallinga, J. Spatial variation of dose rate from beta sources as measured using single grains. *Ancient TL* **24**, 1-7 (2006).

31. Armitage, S .J., Jasim, S. A., Marks, A. E., Parker, A. G., Usik, V. I., Uerpmann, H. - P. The Southern Route "Out of Africa": Evidence for an Early Expansion of Modern Humans into Arabia. *Science* **331**, 453-456 (2011).

32. Murray, A. S., Wintle, A. G. Luminescence dating of quartz using an improved single-aliquot regenerative-dose protocol. *Radiat. Meas.* **32**, 57-73 (2000).

33. Jacobs, Z. et al. Ages for the Middle Stone Age of southern Africa: Implications for human behavior and dispersal. *Science* **322**, 733-735 (2008).

34. Roberts, R. G., Galbraith, R. F., Olley, J. M., Yoshida, H., Laslett, G. M. Optical dating of single and multiple grains of quartz from Jinmium rock shelter, northern Australia: Part II, results and implications. *Archaeometry* **41**, 365-395 (1999).

35. Wallinga, J., Murray, A., Duller, G. A. T. Underestimation of equivalent dose in single-aliquot optical dating of feldspars caused by preheating. *Radiat. Meas*. **32**, 691-695 (2000).

36. Jacobs, Z., Duller, G.A.T., Wintle, A.G. Interpretation of single grain Dedistributions and calculation of De. *Radiat. Meas*. **41**, 264-277 (2006).

37. Thomsen, K.J., Murray, A.S., Bøtter-Jensen, L. Sources of variability in OSL dose measurements using single grains of quartz. *Radiat. Meas.* **39**, 47-61 (2005).

38. Duller, G. A. T. Assessing the error on equivalent dose estimates derived from single aliquot regenerative dose measurements. *Ancient TL* **25**, 15-24 (2007).

39. Duller, G. A. T., Bøtter-Jensen, L., Murray, A. S. Optical dating of single sand-sized grains of quartz: Sources of variability. *Radiat. Meas.* **32**, 453-457 (2000).

40. Jacobs, Z., Duller, G. A. T., Wintle, A. G. Optical dating of dune sand from Blombos Cave, South Africa: II - Single grain data. *J. Hum. Evol*. **44**, 613-625 (2003).

41. Thomsen, K. J., Murray, A. S., Bøtter-Jensen, L., Kinahan, J. Determination of burial dose in incompletely bleached fluvial samples using single grains of quartz. *Radiat. Meas*. **42**, 370-379 (2007).

42. Duller, G. A. T. Distinguishing quartz and feldspar in single grain luminescence measurements. *Radiat. Meas*. **37**, 161-165 (2003).

43. Petraglia, M. D. et al. Hominin Dispersal into the Nefud Desert and Middle Palaeolithic Settlement along the Jubbah Palaeolake, Northern Arabia. *PLoS ONE* **7**, e49840 (2012).

44. Galbraith, R. F., Roberts, R. G., Laslett, G. M., Yoshida, H., Olley, J. M. Optical dating of single and multiple grains of quartz from Jinmium rock shelter, northern Australia: Part I, experimental design and statistical models. *Archaeometry* **41**, 339-364 (1999).

45. Armitage, S. J., King, G. E. Optically stimulated luminescence dating of hearths from the Fazzan Basin, Libya: A tool for determining the timing and pattern of Holocene occupation of the Sahara. *Quat. Geochronol*. **15**, 88-97 (2013).

46. Tribolo, C., Mercier, N., Rasse, M., Soriano, S., Huysecom, E. Kobo 1 and L'Abri aux Vaches (Mali, West Africa): Two case studies for the optical dating of bioturbated sediments. *Quat. Geochronol.* **5**, 317-323 (2010).

47. Bøtter-Jensen, L., Mejdahl, V. Assessment of beta dose-rate using a GM multicounter system. *Int. J. Rad. Appl. Instrum. B.* **14**, 187-191 (1988).

48. De Corte, F. et al. Preparation and characterization of loess sediment for use as a reference material in the annual radiation dose determination for luminescence dating. J. Radioanal. *Nucl. Chem.* **272**, 311-319 (2007).

49. Hong, D. *Luminescence stimulated from quartz by green light: developments relevant to dating*. (PhD thesis, University of Edinburgh, 1988).

50. Mejdahl, V. Thermoluminescence dating: Beta- dose attenuation in quartz grains. *Archaeometry* **21**, 61-72 (1979).

51. Prescott, J. R., Hutton, J. T. Cosmic ray and gamma ray dosimetry for TL and ESR. *Int. J. Rad. Apple. Instrum.* **14**, 223-227 (1988).

52. Bennett K. D. Determination of the Number of Zones in a Biostratigraphical Sequence. *New Phytologist* **132**, 155-170 (1996).

53. Wagner B, *et al*. A 40,000-year record of environmental change from ancient Lake Ohrid (Albania and Macedonia). *J. Paleolimnology* **41**, 407-430 (2009).

54. Bennion, H., Simpson, G. The use of diatom records to establish reference conditions for UK lakes subject to eutrophication. *J. Paleolimnology* **45,** 1-20 (2011).

55. Rosenberg, T. M. *et al.* Middle and Late Pleistocene humid periods recorded in palaeolake deposits of the Nafud desert, Saudi Arabia. *Quatern. Sci. Rev.* **70**, 109-123 (2013).

56. Saros, J. E., Anderson, N. J. The ecology of the planktonic diatom Cyclotella and its implications for global environmental change studies. *Bio. Rev. Camb. Philos.* **90**, 522-541 (2015).

57. Wunsam, S., Schmidt, R., Klee, R. Cyclotella-taxa (Bacillariophyceae) in lakes of the Alpine region and their relationship to environmental variables. *Aquat. Sci.* **57**, 360-386 (1995).

58. Verschuren, D., Laird, K. R., Cumming, B. F. Rainfall and drought in equatorial east Africa during the past 1,100 years. *Nature* **403**, 410-414 (2000).

59. Wolin, J. A., Stone, J. R. in *The Diatoms Applications to the Environmental and Earth Sciences* (eds Stomer, F., Smol, J.P.) 174-185 (Cambridge University Press, Cambridge, 2010)

60. McGowan, S., Grauert, M., Anderson, N. J. A late Holocene record of landscape degradation from Heygsvatn, the Faroe Islands. *Palaeogeography Palaeoclimatology Palaeoecology* **264**(1-2) 11-24 (2008).

61. Phillips, G., Pietilainen, O. P., Carvalho, L., Solimini, A., Solheim, A. L., Cardoso, A. C Chlorophyll-nutrient relationships of different lake types using a large European dataset. *Aquatic Ecology* **42**(2) 213-226 (2008).

62. Alonso-Zarza, A. M. Palaeoenvironmental significant of palustrine carbonates and calcretes in the geological record. *Earth Sci. Rev.* **60**, 261-298 (2003).

63. Verrecchia, E. P. in *Geochemical Sediments and Landscapes* (eds Nash, D. J., McLaren, S. J.) 298-329 (Blackwell, Oxford, 2007).

64. Talbot, M. R. A review of the palaeohydrological interpretation of carbon and oxygen isotopic ratios in primary lacustrine carbonates. *Chem. Geol.* **80**, 261-279 (1990).

65. Li, H .C., Ku, T. L. $\delta^{13}C$-$\delta^{18}O$ covariance as a paleohydrological indicator for closed-basin lakes. *Palaeogeogr. Palaeoclimatol. Palaeoecol.* **133**, 69-80 (1997).

66. Leng, M.J. and Marshall, J.D. Palaeoclimate interpretation of stable isotope data from lake sediment archives. *Quatern. Sci. Rev.* **23**, 811–831 (2004).

67. Holmes, J.A., et al. Holocene palaeolimnology of Kajemamm Oasis, Northern Nigeria: an isotopic study of ostracodes, bulk carbonate and organic carbon. *J. Geol. Soc*., **154**, 311-319 (1997).

68. Marshall, J.D., et al. A high resolution late glacial isotopic record from Hawes Water, Northwest England. Climatic oscillations: calibration and comparison of palaeotemperature proxies. *Palaeogeorg., Palaeoclimatol., Palaeoecol*. **185,** 25-40 (2002).

69. Rozanski, K., Araguas-Araguas, L., Gonfiantini, R. Isotopic Patterns in Modern Global Precipitation. In: Swart, P.K., Lohmann, K.C., McKenzie, J., Savin, S. (eds).

Climate Change in Continental Isotopic Records. Geophysical Monograph 78, American Geophysical Union, 1-36 (1993).

70. Parton, A., et al. Orbital-scale climate variability in Arabia as a potential motor for human dispersals. *Quatern. Int.* **382,** 82-97 (2015).
71. Fleitmann, D., Matter, A., Pint, J.J., Al-Shanti, M. The speleothem record of climate change in Saudi Arabia. Saudi Geological Survey report, SGS-OF-2004-8 (2004).
72. Eltringham, S. K. *The Hippos: Natural History and Conservation* (Academic Press, London, 1999)
73. Estres, R. D. *The Behaviour Guide to African Mammals*. (University of California Press, Berkeley, 1991).
74. Belmaker, M. In *Out of Africa I: The First Hominin Colonization of Eurasia* (eds. Fleagle, J. G., Shea, J. J., Grine, F. E., Baden, A. L., Leakey, R. E.) 183-205 (Springer, 2010).
75. Martínez-Navarro, B. in *Out of Africa I: The First Hominin Colonization of Eurasia* (eds. Fleagle, J. G., Shea, J. J., Grine, F. E., Baden, A. L. & Leakey, R. E) 207-224 (Springer, New York, 2010).
76. Martínez-Navarro, B., Rook, L., Segid, A., Yosief, D., Farretti, M. P., Shoshani, J., Techle, T. M., Libsekal, Y. The large fossil mammals from Buia (Eritrea): systematics, biochronology and paleoenvironments. *Riv. Ital. Paleontol. S.***110,** 61-88 (2004).
77. Shreeve, D. C. A new record of Pleistocene hippopotamus from River Severn terrace deposits, Gloucester, UK-palaeoenvironmental setting and stratigraphical significance. *P. Geologist. Assoc.* **120**, 58-64 (2009).
78. van Kolfschoten, Th. The Eemian mammal fauna of central Europe. *Geol. Mijnbouw-N. J. G.* **79,** 269-281 (2000).

79. Tchernov, E. The Afro-Arabian Component in the Levantine Mammalian Fauna – A Short Biogeographical Review. *Isr. J. Zool.* **38,** 155-159 (1992).

80. Geraads, D. Plio-Pleistocene Mammalian Biostratigraphy of Atlantic Morocco. *Quaternaire*. **13,** 43-53 (2002).

81. Michel, P., Wengler, L. *Un Site Palaeontologique Avec Des Vestiges Archeologiques: La Carriere Doukkala II* (Region De Temara – Maroc Atlantique). **5,** 11-41 (1993).

82. Stimpson, C. et al. Middle Pleistocene vertebrate fossils from the Nefud Desert, Saudi Arabia: Implications for biogeography and palaeoecology. *Quatern. Sci. Rev.* **143**, 13-36 (2016).

83. McClure, H. A. *Late Quaternary Palaeoenvironments of the Rub' al Khali.* (PhD Thesis, Univeristy College, London, 1984).

84. O'Regan, H. J., Turner, A., Bishop, L. C., Elton, S., Lamb, A. L. Hominins without fellow travellers? First appearances and inferred dispersals of Afro-Eurasian large mammals in the Plio-Pleistocene. *Quatern. Sci. Rev.* **30**, 1343-1352 (2011).

85. Hadjouis, D. Présence du genera *Kobus* (Bovidae, Artiodactyla) dans le Pléstocenène Supérieur D'Algérie. *L'Anthropologie*. **90,** 317-320 (1986).

86. Kowalski, K., Neer, W. V., Bockenski, Z., Mlynarsko, M., Rzabik-Kowalska, B., Szyndlar, Z., Gautier, A., Close, A. E., Wendorf, F. A Last Interglacial Fauna from the Eastern Sahara. *Quat. Res.* **32,** 335-341 (1989).

87. Blinkhorn, J., Achyuthan, H., Petraglia, M. D. Ostrich expansion into India during the Late Pleistocene: Implications for continental dispersal corridors. *Palaeogeogr., Palaeoclimatol., Palaeoecol.* **417**, 80-90 (2015).

88. Jain, S., Rai, N., Kumar, G., Pruithi, P. A., Thangaraj, K., Bajpai, S., Pruthi, V. Ancient DNA Reveals Late Pleistocene Existence of Ostriches in Indian Sub-Continent. *PLoS ONE*. **12,** e0164823 (2017).

89. Domínguez-Rodrigo, M., Egeland, C. P., Barba, R. in *Deconstructing Olduvai: A Taphonomic Study of the Bed I Sites* (eds. Dominguqes-Rodrigo, M., Barba, R. & Egelend, C. P.) 23-32 (Springer, New York, 2007)

90. Cruz-Uribe, K. Distinguishing hyena from hominid bone accumulations. *J. F. Archaeol.* **18,** 467–486 (1991).

91. Petraglia, M. D. et al. Middle Palaeolithic occupation on a Marine Isotope Stage 5 lakeshore in the Nefud Desert, Saudi Arabia. *Quatern. Sci. Rev*. **30**, 1555-1559 (2011).

92. Scerri, E. M. L. et al. Middle to Late Pleistocene human habitation in the western Nefud Desert. *Quatern. Int*. **382**, 200-214 (2015).

93. Groucutt, H. S. et al. Human occupation of the Arabian Empty Quarter during MIS 5: evidence from Mundafan al-Buhayrah. *Quatern. Sci. Rev.* **119**, 116-135 (2015).

94. Scerri, E. M. L., Drake, N. A., Jennings, R., Groucutt, H. S. Earliest evidence for the structure of *Homo sapiens* populations in Africa. *Quatern. Sci. Rev*. **101**, 207-2016 (2014).

95. Scerri, E. M. L., Groucutt, H. S., Jennings, R. P., Petraglia, M. D. Unexpected technological heterogeneity in northern Arabia indicates complex Late Pleistocene demography at the gateway to Asia. *J. Hum. Evol*. **75**, 125-142 (2014).

96. Scerri, E. M. L., Gravina, B., Blinkhorn, J., Delagnes, A. Can lithic attribute analyses identify discrete reduction trajectories? A quantitative study using refitted lithic sets. *J. Arch. Method Theory* **23**, 669-691.

97. Groucutt, H. S. et al. Late Pleistocene lakeshore settlement in Arabia: Middle Palaeolithic technology from Jebel Katefeh, Jubbah. *Quatern. Int.* **382**, 215-236.

98. Jennings, R. P., Parton, A., Clark-Balzan, L., White, T. S., Groucutt, H. S., Breeze, P., Parker, A. G., Drake, N. A., Petraglia, M. D. Human occupation of the northern Arabia interior during early Marine Isotope State 3. *J. Quat. Sci*. **31**, 953-966 (2017).

99. Groucutt, H. S. et al. Middle Palaeolithic raw material procurement and early stage reduction at Jubbah, Saudi Arabia. *Arch. Res. Asia*. **9**, 44-62 (2017).

100. Clarkson, C. An Index of Invasiveness for the measurement of unifacial and bifacial retouch: a theoretical, experimental, and archaeological verification. *J. Arch. Sci.* **29,** 65-75 (2002).

101. Kuhn, S. L., A geometric index of reduction for unifacial stone tools. *J. Arch. Sci.* **17**, 583-593 (1990).

102. Groucutt, H.S. Middle Palaeolithic point technology, with a focus on the site of Tor Faraj (Jordan, MIS 3). *Quatern. Int*. **350**, 205-226.

103. Hovers, E. *The Lithic Assemblages of Qafzeh Cave* (Oxford University Press, Oxford, 2009).

104. Marks, A. E. in *The Prehistory of Nubia, Vol. 1* (ed Wendorf, F.) 315-391 (SMU Press, Dallas, 1968).

105. Goder-Goldberger, M. The Khormusan: Evidence for an MSA East African industry in Nubia. *Quatern. Int*. **300,** 182-194 (2013).

106. Rose, J. I., Marks, A. E. “Out of Arabia” and the Middle-Upper Palaeolithic transition in the southern Levant. *Quartär* **61**, 49-85 (2014).

107. Wendorf, F., Schild, R., Close, A. E., and associates. Egypt *During the Last Interglacial: The Middle Paleolithic of Bir Tarfawi and Bir Sahara East*. (Plenum, New York,1993).

108. Yellen, J. et al. The archaeology of Aduma Middle Stone Age sites in the Awash Valley, Ethiopia. *Paleoanthropology* **2005**, 25-100 (2005).

109. Shea, J. J. 2008. The Middle Stone Age archaeology of the Lower Omo Valley Kibish Formation: Excavations, lithic assemblages, and inferred patterns of early *Homo sapiens* behaviour. *J. Hum. Evol*. **55**, 448-485 (2008)

110. Groucutt, H. S. et al. Stone tool assemblages and models for the dispersal of *Homo sapiens* out of Africa. *Quatern. Int.* **382**, 8-30 (2015).

111. Horwitz, L.K., Smith, P., Faerman, M., Boaretto, E., Segal, I. The application of biometry LA-ICP-MS to provenance isolated bones: a study of hominin remains from Oumm-Qatafa Cave, Judean Desert. *Archaeol. Anthropol. Sci.* **3**, 245-62 (2011).

112. Walker, M. J., Ortega, J., López, M. V., Parmová, K. & Trinkaus, E. Neanderthal postcranial remains from the Sima de las Palomas del Cabezo Gordo, Murcia, Southeastern Spain. *Am. J. Phys. Anthropol***. 144**, 505-515 (2011).

113. Lorenzo, C, Arsuaga, J, Carretero, J.M. Hand and foot remains from the Gran Dolina Early Pleistocene site (Sierra de Atapuerca, Spain). *J. Hum. Evol*. **37,** 501-522 (1999).

114. Larson, S.G. et al. Descriptions of the upper limb skeleton of Homo floresiensis. *J. Hum. Evol.* **57**, 555-570 (2009).

115. Mersey, B., Jabbour, R.S., Brudvik, K., Defleur, A. Neandertal hand and foot remains from Moula-Guercy, Ardeche, France. *Am. J. Phys. Anthropol*. **152**, 516-529 (2013).

116. Semal, P., et al. New data on the late Neanderthals: direct dating of the Belgian Spy Fossils. *Am. J. Phys. Anthropol*. **138**, 421-428 (2009).

117. Trinkaus, E. *The Shanidar Neanderthals*. (Academic Press, New York, 1983).

118. Trinkaus E. *The Krapina Human Postcranial Remains: Morphology, Morphometrics and Paleopathology*. (University of Zagreb, Zagreb, 2016)

119. Sládek, V, Trinkaus, E, Hillson, S.W., Holliday, T.W. The people of the Pavlovian. Skeletal catalogue and osteometrics of the Gravettian fossil hominids from Dolni Vestonice and Pavlov. Dolni Vestonice Studies, Svazek 5 (2000).

120. Trinkaus, E., Buzhilova, A.P., Mednikova, M.B., Dobrovolskaya, M.V. *The people of Sunghir: burials, bodies, and behavior in the earlier Upper Paleolithic.* (Oxford University Press, Oxford, 2014).

121. Shang, H., Trinkaus, E. *The early modern human from Tianyuan Cave, China* (Texas A & M University Press, 2010)

122. McCown, T.D., Keith, A. The Stone Age of Mount Carmel: The Fossil Human Remains from the Levallois-Mousterian, Vol. II. (Clarendon Press, Oxford, 1939).

123. Trinkaus, E., Svoboda, J.A., Wojtal, P., Nyvltova Fisakova, M., Wilczynski, J. Human remains from the Moravian Gravettian: morphology and taphonomy of additional elements from Dolni Vestonice II and Pavlov 1. *Int. J. Osteoarchaeol.* **20**, 645-669 (2010).

124. Trinkaus, E., Bailey, S.E., Zilhao, J. Upper Paleolithic human remains from the Gruta do Caldeirao, Tomar, Portugal. *Revista Portuguesa de Arquelologia* **4**, 5-17 (2001).

Supplementary Table 1. Calliper measurements of AW-1 phalanx following measurement scheme of Horwitz and colleagues[111], proximal radio-ulnar maximum breadth following[112.]

Measurement	**Measurement no.[111]**	**Value (mm)**	**Notes**
Maximum length	1	32.25	
Inter-articular length	2	30.21	
Midshaft dorso-palmar breadth	3	6.25	Measured just distal to the pathology, which lies across midshaft (actual measurement location at <1mm distal to true midshaft).
Midshaft radio-ulnar breadth	4	8.53	
Proximal joint surface dorso-palmar height	5	8.03	Proximal joint surface damaged, estimate.
Proximal joint surface radio-ulnar breadth	6	11.92	
Proximal radio-ulnar maximum breadth	n/a	14.98	
Distal joint surface dorso-palmar height	7	5.25	
Distal joint surface radio-ulnar breadth	8	8.72	Distal joint surface incomplete, estimate.
Midshaft circumference	9	14	

Supplementary Table 2. Comparative sample for linear metric analysis of Al Wusta-1 intermediate phalanx.

Taxon	Specimen	IP ray	total sample	Source of data
A. afarensis	AL 333x-18	IP2-4	n=5	measured directly from fossils by TLK
	AL 333-32	IP2-4		
	AL 333-46	IP2-4		
	AL 333-88	IP2-4		
	AL 333-149	IP2-4		
A. africanus	StW 331	IP2-4	n=1	measured directly from fossils by TLK
A. sediba	MH2	IP3, IP4	n=2	measured directly from fossils by TLK
Swartkrans (*A. robustus*/early *Homo*)	SKX 13476	IP2-4	n=6	measured directly from fossils by TLK
	SKX 5019	IP2-4		
	SKX 5021	IP2-4		
	SKX 9449	IP2-4		
	SKX 36712	IP2-4		
	SKX 35439	IP2-4		
H. antecessor	ATD6-28	IP3-4	n=2	published values from Lorenzo et al.[112]
	ATD6-53	IP3-4		
H. naledi	Hand 1	IP2, IP3, IP4	n=5	measured directly from fossils by TLK
	UW 101-1646	IP3		
	UW 101-1647	IP4		
H. floresiensis	LB6/9	IP?	n=2	published values from Larson et al.[113]
	LB1/48	IP?		
H. neanderthalensis	Amud 1	IP2, IP3?	min. n=12 individuals n=27 IPs	measured directly from fossils by TLK
	Kebara 2	IP2, IP3, IP4		measured directly from fossils by TLK
	Tabun 1	IP2, IP4?		measured directly from fossils by TLK
	Moula Guercy M-G1-154	IP2-4		published values from Mersey et al.[114]
	Spy 430a	IP3		published values from Semal et al.[115]

	Spy 390a	IP3		
	Spy 484a	IP4		
	Shanidar 3	IP3, IP4		published values from Trinkaus[116]
	Shanidar 4	IP2, IP3, IP4		
	Shanidar 5	IP3, IP4		
	Shanidar 6	IP3		
	Krapina 205.1	IP3-4		published values from Trinkaus[117]
	Krapina 205.2	IP3-4		
	Krapina 205.3	IP3-4		
	Krapina 205.4	IP3-4		
	Krapina 205.5	IP3-4		
	Krapina 205.6	IP3-4		
	Krapina 205.7	IP3-4		
	Krapina 205.8	IP3-4		
	Krapina 205.10	IP2		
	Krapina 205.12	IP3-4		
	Krapina 205.13	IP3-4		
	Krapina 205.14	IP2		
	Krapina 205.15	IP2		
	Krapina 205.17	IP2		
	Krapina 205.18	IP2		
early *H. sapiens*	Dolni Vestonice 3	IP2-3	n=17 individuals	published values from Sladek et al.[118]
	Dolni Vestonice 13	IP2-3, IP4	n=33 IPs	
	Dolni Vestonice 14	IP3		
	Dolni Vestonice 15	IP2, IP3		
	Dolni Vestonice 16	IP2, IP3, IP4		
	Dolni Vestonice 34	IP2-3		
	Ohalo II H2	IP2, IP3, IP4		measured directly from fossils by TLK
	Qafzeh 9	IP2		measured directly from fossils by TLK
	Qafzeh 8	IP2, IP3, IP4		measured directly from fossils by TLK
	Barma Grande 2	IP3, IP4		measured directly from fossils by NBS

	Arene Candide 2	IP2, IP3, IP4		measured directly from fossils by NBS
	Sunghir 1	IP2, IP3, IP4, IP5		published values in Trinkaus et al.[119]
	Tianyuan 1	IP2?		published values in Shang and Trinkaus[120]
	Skhul IV	IP3, IP4, IP5		published values in McCown and Keith[121]
	Pavlov 33	IP?		published values in Trinkaus et al.[122]
	Caldeirao 9	IP2-4		published values in Trinkaus et al.[123]
	Cueva Victoria CV-0*	IP2		published values in Martinez-Navarro et al.[1]
recent *H. sapiens*		IP2-4	n=22 individuals	measured directly from specimens by TLK
Pan (*P. troglodytes* & *P. paniscus*)		IP2-5	n=67 IPs n=8 individuals	measured directly from specimens by TLK
Gorlla (*G. gorilla* & *G. beringei*)		IP2-5	n=34 IPs n=8 individuals	measured directly from specimens by TLK
Cercopithecids		IP2-5	n=34 IPs n=11 IPs	measured directly from specimens by TLK

*The taxonomic association of this specimen with *H. sapiens* is questionable[1,2]

Supplementary Table 3. Results from Mann-Whitney U pairwise comparisons with Bonferroni correction (α = 0.003) of all shape ratios (i.e. divided by the total length of the phalanx). All breadth measurements are radio-ulnar dimensions and all height measurements are dorsopalmar dimensions. All significant pairwise comparisons are in bold text.

			Cercopiths	*Gorilla*	*Pan*	Neandertal	early *H. sapiens*	*H. sapiens*
base breadth	above	**Cercopiths**	x	0.007	**0.000**	0.079	0.110	0.018
prox. articular breadth	below	***Gorilla***	**0.001**	x	**0.000**	**0.000**	0.133	0.869
		Pan	**0.000**	0.000	x	**0.000**	**0.000**	**0.000**
		Neandertal	0.196	0.000	**0.000**	x	**0.000**	**0.000**
		early *H. sapiens*	0.130	0.009	**0.000**	**0.001**	x	0.125
		H. sapiens	0.033	0.022	**0.000**	**0.000**	0.368	x
prox. shaft breadth	above	**Cercopiths**	x	**0.001**	**0.000**	**0.000**	**0.000**	**0.000**
midshaft breadth	below	***Gorilla***	0.526	x	**0.000**	0.180	**0.000**	0.481
		Pan	**0.000**	**0.000**	x	0.123	0.011	**0.000**
		Neandertal	0.886	0.418	**0.000**	x	0.011	0.404
		early *H. sapiens*	0.088	0.052	**0.000**	0.009	x	**0.000**
		H. sapiens	**0.001**	**0.000**	**0.000**	**0.000**	**0.000**	x
midshaft height	above	**Cercopiths**	x	**0.000**	**0.000**	0.866	0.014	**0.000**
distal shaft breadth	below	***Gorilla***	0.032	x	**0.000**	**0.000**	**0.001**	**0.000**
		Pan	**0.000**	**0.000**	x	**0.000**	**0.000**	**0.000**
		Neandertal	0.048	0.356	0.076	x	0.005	**0.000**
		early *H. sapiens*	**0.000**	**0.000**	**0.002**	**0.003**	x	0.359
		H. sapiens	0.005	0.625	**0.000**	0.481	**0.000**	x
distal shaft height	above	**Cercopiths**	x	**0.000**	**0.000**	0.004	**0.000**	0.020
prox. articular height	below	***Gorilla***	0.200	x	**0.000**	0.640	**0.002**	**0.000**
		Pan	**0.000**	**0.000**	x	0.087	0.010	**0.000**
		Neandertal	0.988	0.164	**0.000**	x	0.026	0.043
		early *H. sapiens*	0.318	0.885	**0.000**	0.120	x	**0.000**
		H. sapiens	0.217	0.674	**0.000**	0.083	0.876	x

Supplementary Table 4. Landmarks used in geometric morphometric analyses of Al Wusta-1 phalanx and the comparative samples.

Landmark	Description
1	Mid-point of distal articulation (distal view, dorsal up)
2	Furthest left point on distal head (dorsal view)
3	Furthest right point on distal head (dorsal view)
4	Furthest proximal point on midline of proximal articulation (proximal view, dorsal up)
5	Mid-point of ridge between two articulations on proximal face (proximal view, dorsal up)
6	Furthest left point on proximal base (dorsal view)
7	Furthest right point on proximal base (dorsal view)
8	Deepest point on left proximal articulation (proximal view, dorsal up)
9	Deepest point on right proximal articulation (proximal view, dorsal up)
10	Centre of trochlea
11	Place where triangular raised region merges with central ridge on proximal palmar surface (palmar view)
12	Most dorsal point on proximal base (dorsal view)
13	Most palmar point of left proximal articulation (proximal view, dorsal up)
14	Most palmar point of right proximal base (proximal view, dorsal up)
15	Furthest point left of the distal trochlea (palmar view)
16	Furthest left point of the proximal articular surface (proximal view, dorsal up)
17	Furthest right point of the proximal articular surface (proximal view, dorsal up)
18	Most palmar point at the mid-line of the proximal articular surface (proximal view, dorsal up)

Supplementary Table 5. Sample used in comparative primate geometric morphometric analyses.

Institutions: Duckworth: Duckworth Collection, University of Cambridge; NHM Vienna: Vienna Natural History Museum; Uni. of Florence: University of Florence; GAUG: Johann-Friedrich-Blumenbach-Institut für Zoologie und Anthropologie der Georg-August-Universität Göttingen; Uni. of Kent: University of Kent; Tel Aviv Uni.: Tel Aviv University; MPNBR: Museo Preistorico Nazionale dei Balzi Rossi, Italy; MAF: Museo Archeologico del Finale, Italy; NHM: Natural History Museum, London; MRAC: Musée Royal de l Afrique Centrale, Tervuren; MPI-EVA: Max Planck Institute, Leipzig; Powell Cotton: Powell Cotton Collection.

Group	Sample number	Institution
Al Wusta	1	
Colobus badius preussi total	7	Powell Cotton
Gorilla gorilla total	20	Powell Cotton
Mandrillus leucophaeus	4	Powell Cotton
Mandrillus sphinx	2	Powell Cotton
Mandrillus total	6	
Pan paniscus	4	MRAC
Pan troglodytes	4	Powell Cotton, MPI-EVA
Pan total	8	
Papio anubis neumanni total	4	
Krapina	17	NESPOS
Regourdou	3	NESPOS
Kebara 2	3	Tel Aviv Uni.
Tabun C1	2	NHM
Neanderthal total	25	
Qafzeh	4	Tel Aviv Uni.
Ohalo	3	Tel Aviv Uni.
Barma Grande	2	MPNBR
Arene Candide	3	MAF
Early *H. sapiens* total	12	
Australian	3	Duckworth
Inuit	1	Duckworth
Kerma	3	Duckworth
Maiden Castle	3	Duckworth
Egyptian Nubian	19	NHM Vienna
Fuegian	3	Uni. of Florence
Siracusian	5	Uni. of Florence
German	13	GAUG
Canterbury	11	Uni. of Kent
Holocene *H. sapiens* total	61	

Supplementary Table 6. Procrustes distances from primate and hominin mean shapes to Al Wusta-1.

Mean Shape	Distance to AW-1
Holocene *H. sapiens*	0.080184
Early *H. sapiens*	0.084209
Mandrillus	0.093510
Gorilla	0.101452
Papio	0.106864
H. neanderthalensis	0.119294
Pan	0.119404
Colobus	0.150987

Supplementary Table 7. Details of the comparative sample of intermediate phalanges from Neanderthals and Pleistocene and Holocene *Homo sapiens* used for geometric morphometric analyses of known side and digit, and cross sectional geometric analyses.

Institutions: Duckworth: Duckworth Collection, University of Cambridge; NHM Vienna: Vienna Natural History Museum; Uni of Florence: University of Florence; GAUG: Johann-Friedrich-Blumenbach-Institut für Zoologie und Anthropologie der Georg-August-Universität Göttingen; Uni of Kent: University of Kent; Tel Aviv Uni: Tel Aviv University; MPNBR: Museo Preistorico Nazionale dei Balzi Rossi, Italy; MAF: Museo Archeologico del Finale, Italy; NHM: Natural History Museum, London.

Group	**Specimen/Group**	**Institution**	**Lefts (n)**			**Rights (n)**			**Sample**
			2nd	**3rd**	**4th**	**2nd**	**3rd**	**4th**	**total**
Holocene *H. sapiens*	Australian	Duckworth		1		1	1	2	**5**
Holocene *H. sapiens*	Kerma	Duckworth	1	1				1	**3**
Holocene *H. sapiens*	Inuit	Duckworth		1			1		**2**
Holocene *H. sapiens*	Maiden Castle	Duckworth		1		1		1	**3**
Holocene *H. sapiens*	Egyptian Nubian	NHM Vienna	2		2	5	6	4	**19**
Holocene *H. sapiens*	Fuegian	Uni of Florence	1		1	1	1		**4**
Holocene *H. sapiens*	Siracusian	Uni of Florence	2	1	1	2	1	2	**9**
Holocene *H. sapiens*	German	GAUG	1	2	2	3	3	2	**13**
Holocene *H. sapiens*	Canterbury	Uni of Kent	1	1	2	2	3	2	**11**
Pleistocene *H. sapiens*	Ohalo 2	Tel Aviv Uni	1		1				**2**
Pleistocene *H. sapiens*	Qafzeh 8	Tel Aviv Uni	1	1	1	1	1	1	**6**
Pleistocene *H. sapiens*	Qafzeh 9	Tel Aviv Uni	1			1	1		**3**
Pleistocene *H. sapiens*	Barma Grande 2	MPNBR		1	1		1	1	**4**
Pleistocene *H. sapiens*	Arene Candide 2	MAF	1	1	1	1	1	1	**6**
Neanderthal	Kebara 2	Tel Aviv Uni	1	1	1	1		1	**5**
Neanderthal	Tabun C1	NHM	1		1				**2**
		Total	**14**	**12**	**14**	**19**	**20**	**18**	**91**

Supplementary Table 8. Procrustes Distances between Al Wusta-1 and other hominin groups with sides pooled.

	Holocene *H. sapiens*	Pleistocene *H. sapiens*	Neanderthal
AW-1	0.078	0.084	0.099

Supplementary Table 9. Procrustes distances between Al Wusta-1 and its nearest neighbours with sides pooled. Specimen numbers refer to Figure 2.

Nearest neighbour	Side	Ray	Procrustes Distance
1) Maiden Castle EU.1.3.70_Sk20	Left	3rd	0.084
2) Egyptian NHMW K24_2	Right	3rd	0.061
3) Canterbury NGB_89_Sk15_1247	Left	3rd	0.072

Supplementary Table 10. Procrustes distances between Al Wusta-1 and comparative groups and ray numbers across groups, analysing left and right hands separately.

Phalanx side	Holocene *H. sapiens*	Pleistocene *H. sapiens*	Neanderthals
Right	0.080	0.090	0.119
Left	0.076	0.081	0.098
	2nd Ray	**3rd Ray**	**4th Ray**
Right	0.095	0.076	0.083
Left	0.092	0.068	0.084

Supplementary Table 11. Procrustes distances between Al Wusta-1 and its nearest neighbours, analysing left and right hands separately.

Nearest neighbour	Side	Ray	Procrustes Distance
Egyptian NHMW K24 3 HP3MR	Right	3rd	0.061
Canterbury NGB 89 Sk15 1247 HP3ML	Left	3rd	0.072

Supplementary Table 12. **U-series results on Al Wusta-1**. All errors are 2-σ. Individual results do not contain errors of standard measurement (correlated errors), mean values incorporate errors of standard.

3675#1	U (ppm)	Th (ppb)	U/Th	$^{230}Th/^{238}U$	$^{230}Th/^{238}U$ error	$^{234}U/^{238}U$	$^{234}U/^{238}U$ error	Age (ka)	Age error (ka)
1	49.99	16	307	0.7293	0.0066	1.6887	0.0053	59.1	0.7
2	48.60	11	425	0.7310	0.0085	1.6817	0.0046	59.6	0.9
3	46.10	14	339	0.7537	0.0052	1.6798	0.0045	62.1	0.6
4	43.85	16	270	0.7724	0.0061	1.6899	0.0073	63.6	0.7
5	34.79	226	154	0.7744	0.0063	1.6801	0.0048	64.3	0.7
6	23.25	290	80	0.7950	0.0107	1.6829	0.0130	66.4	1.4
7	19.12	166	115	0.7851	0.0094	1.6861	0.0051	65.2	1.1
8	15.34	118	131	0.7791	0.0109	1.6895	0.0107	64.4	1.3
9	14.22	106	135	0.7522	0.0088	1.6807	0.0092	61.9	1.0
10	14.65	129	114	0.7574	0.0093	1.6882	0.0173	62.1	1.3
11	15.29	100	152	0.7622	0.0084	1.6794	0.0101	63.1	1.0
12	14.58	89	164	0.7559	0.0082	1.6895	0.0074	61.9	0.9
13	12.02	81	148	0.7474	0.0089	1.6828	0.0099	61.3	1.1
14	10.84	69	157	0.7516	0.0102	1.6798	0.0106	61.9	1.2
15	11.08	54	207	0.7598	0.0103	1.6808	0.0118	62.7	1.3
16	11.22	48	235	0.7585	0.0115	1.6772	0.0106	62.8	1.3
17	11.20	47	240	0.7558	0.0111	1.6871	0.0104	62.0	1.3
18	10.85	58	188	0.7606	0.0107	1.6933	0.0090	62.2	1.2
19	10.08	48	211	0.7558	0.0135	1.6884	0.0104	61.9	1.5
20	9.01	51	177	0.7572	0.0119	1.6952	0.0093	61.7	1.3
21	7.81	70	111	0.7489	0.0133	1.6825	0.0098	61.5	1.5
22	7.30	80	92	0.7311	0.0123	1.6858	0.0116	59.5	1.4
23	6.57	72	91	0.7275	0.0124	1.6769	0.0088	59.5	1.4
24	6.27	65	96	0.7251	0.0161	1.6833	0.0093	59.0	1.7
25	6.19	67	92	0.7361	0.0120	1.6666	0.0159	60.9	1.5
26	5.34	68	78	0.7338	0.0216	1.6691	0.0154	60.6	2.4
27	5.33	61	87	0.7405	0.0132	1.6833	0.0150	60.6	1.6
28	5.55	51	109	0.7351	0.0107	1.6971	0.0165	59.3	1.3
29	5.63	46	124	0.7527	0.0136	1.6880	0.0109	61.6	1.5
30	5.28	37	143	0.7333	0.0169	1.6821	0.0168	59.9	1.9
MEAN VALUES									
1-30				0.7547	0.0129	1.6843	0.0152	62.0	1.6

3675#2	U (ppm)	Th (ppb)	U/Th	$^{230}Th/^{238}U$	$^{230}Th/^{238}U$ error	$^{234}U/^{238}U$	$^{234}U/^{238}U$ error	Age (ka)	Age error (ka)
1	57.79	16	3687	0.5955	0.0200	1.6802	0.0107	46.3	1.9
2	57.29	9	6263	0.6742	0.0066	1.6675	0.0068	54.5	0.7
3	53.84	7	8207	0.7077	0.0114	1.6700	0.0061	57.8	1.2
4	47.64	5	9152	0.7705	0.0068	1.6852	0.0127	63.7	1.0
5	45.61	5	9414	0.7969	0.0088	1.6784	0.0077	66.9	1.1
6	42.56	4	1079	0.7910	0.0122	1.6714	0.0172	66.6	1.7
7	40.59	3	1267	0.7948	0.0084	1.6845	0.0094	66.3	1.1
8	38.07	2	1570	0.7810	0.0075	1.6844	0.0088	64.8	0.9
9	37.47	2	1760	0.7814	0.0125	1.6748	0.0196	65.4	1.7
10	37.71	2	1541	0.7671	0.0079	1.6749	0.0174	63.8	1.2
11	33.73	2	1364	0.7640	0.0067	1.6755	0.0094	63.5	0.9
12	30.04	3	1166	0.7767	0.0112	1.6806	0.0097	64.6	1.3
13	30.55	3	1109	0.7883	0.0082	1.6952	0.0125	65.1	1.1
14	29.63	3	1097	0.7787	0.0085	1.6844	0.0086	64.6	1.0
15	23.02	22	1060	0.7867	0.0099	1.6800	0.0076	65.7	1.2
16	17.81	33	540	0.8032	0.0098	1.6839	0.0093	67.3	1.2
17	14.64	22	660	0.8113	0.0091	1.6941	0.0118	67.6	1.2
18	12.94	30	425	0.7987	0.0076	1.6783	0.0112	67.1	1.0
19	10.54	39	272	0.7877	0.0106	1.6873	0.0097	65.4	1.3
20	8.24	48	171	0.7746	0.0125	1.6877	0.0069	64.0	1.4
21	6.20	61	102	0.7546	0.0143	1.6917	0.0102	61.6	1.6
22	5.00	31	160	0.7692	0.0162	1.6939	0.0166	63.1	1.9

23	4.40	17	256	0.7668	0.0163	1.6926	0.0146	62.9	1.9
24	3.90	12	319	0.7495	0.0165	1.6929	0.0151	61.0	1.9
25	3.57	11	329	0.7547	0.0183	1.6891	0.0145	61.8	2.1
26	2.97	10	296	0.7577	0.0177	1.6826	0.0146	62.4	2.0
27	2.63	9	282	0.7240	0.0209	1.6951	0.0197	58.3	2.3
28	2.34	8	299	0.6894	0.0234	1.6955	0.0151	54.8	2.4
29	2.16	7	300	0.6274	0.0259	1.6883	0.0174	49.0	2.6
30	1.85	6	331	0.6463	0.0358	1.6758	0.0322	51.3	3.7
MEAN VALUES									
5-26				0.7837	0.0135	1.6814	0.0154	65.3	1.7

3675#3	U (ppm)	Th (ppb)	U/Th	$^{230}Th/^{238}U$	$^{230}Th/^{238}U$ error	$^{234}U/^{238}U$	$^{234}U/^{238}U$ error	Age (ka)	Age error (ka)
1	58.44	18	3325	0.6462	0.0124	1.6700	0.0073	51.6	1.3
2	56.93	8	7353	0.6569	0.0049	1.6696	0.0153	52.6	0.8
3	55.96	6	9673	0.6594	0.0066	1.6702	0.0096	52.9	0.8
4	47.14	5	9675	0.6976	0.0087	1.6696	0.0108	56.7	1.0
5	41.59	35	1201	0.7572	0.0132	1.6680	0.0139	63.1	1.6
6	37.40	11	3388	0.8065	0.0132	1.6908	0.0192	67.3	1.8
7	38.25	7	5596	0.7945	0.0094	1.6807	0.0074	66.5	1.1
8	38.32	5	7199	0.7931	0.0102	1.6773	0.0157	66.5	1.4
9	38.60	5	8198	0.8012	0.0106	1.6876	0.0156	66.9	1.4
10	37.61	2	1640	0.7850	0.0062	1.6900	0.0124	65.0	0.9
11	35.79	3	1383	0.7851	0.0086	1.6803	0.0087	65.5	1.0
12	35.59	2	1452	0.7800	0.0088	1.6783	0.0102	65.1	1.1
13	36.60	2	1522	0.7671	0.0057	1.6745	0.0088	63.8	0.8
14	32.65	2	1478	0.7566	0.0063	1.6792	0.0075	62.5	0.8
15	30.15	3	1155	0.7659	0.0103	1.6884	0.0125	63.0	1.3
16	27.97	3	1025	0.7703	0.0085	1.6835	0.0129	63.7	1.1
17	25.75	4	6415	0.7698	0.0120	1.6816	0.0171	63.8	1.6
18	24.69	3	8744	0.7781	0.0090	1.6691	0.0107	65.3	1.1
19	22.23	3	8589	0.7997	0.0127	1.6868	0.0087	66.8	1.5
20	19.33	3	6449	0.8015	0.0108	1.6820	0.0131	67.2	1.4
21	14.70	10	1482	0.7975	0.0083	1.6827	0.0059	66.7	1.0
22	8.99	19	471	0.7862	0.0162	1.6855	0.0115	65.3	1.9
23	5.23	11	497	0.7627	0.0172	1.6863	0.0158	62.8	2.0
24	5.05	6	827	0.7796	0.0105	1.7064	0.0110	63.5	1.2
25	5.18	8	667	0.7626	0.0118	1.6977	0.0141	62.2	1.4
26	5.43	8	653	0.7599	0.0196	1.6880	0.0132	62.4	2.2
27	5.14	5	1090	0.7318	0.0161	1.6956	0.0179	59.1	1.9
28	4.91	4	1297	0.7474	0.0144	1.6741	0.0193	61.7	1.8
29	4.70	3	1664	0.7497	0.0153	1.6738	0.0139	62.0	1.8
30	4.32	2	1859	0.7433	0.0144	1.6836	0.0160	60.8	1.7
MEAN VALUES									
5-30				0.7821	0.0135	1.6827	0.0154	65.0	1.7

3675#4	U (ppm)	Th (ppb)	U/Th	$^{230}Th/^{238}U$	$^{230}Th/^{238}U$ error	$^{234}U/^{238}U$	$^{234}U/^{238}U$ error	Age (ka)	Age error (ka)
1	59.50	39	1524	0.6319	0.0102	1.6640	0.0054	50.4	1.0
2	61.70	14	4513	0.6370	0.0064	1.6770	0.0311	50.4	1.3
3	55.83	9	6523	0.6833	0.0087	1.6684	0.0049	55.3	0.9
4	46.15	6	8275	0.7477	0.0088	1.6755	0.0096	61.7	1.1
5	40.88	6	6811	0.8026	0.0100	1.6834	0.0081	67.3	1.2
6	37.30	5	6899	0.8437	0.0085	1.6773	0.0067	72.3	1.1
7	35.26	3	1049	0.8453	0.0054	1.6879	0.0048	71.8	0.7
8	36.35	3	1420	0.8305	0.0077	1.6833	0.0067	70.4	1.0
9	35.68	3	1253	0.8276	0.0079	1.6798	0.0080	70.3	1.0
10	33.76	2	1598	0.8366	0.0057	1.6846	0.0066	71.0	0.8
11	33.52	2	1678	0.8263	0.0069	1.6815	0.0104	70.0	1.0
12	32.93	2	1780	0.8117	0.0072	1.6814	0.0039	68.4	0.8
13	32.85	2	2134	0.8043	0.0070	1.6824	0.0086	67.5	0.9
14	31.36	2	1722	0.7961	0.0074	1.6893	0.0078	66.2	0.9

15	29.38	2	1603	0.7894	0.0074	1.6852	0.0093	65.7	1.0
16	28.26	1	1957	0.7801	0.0083	1.6719	0.0087	65.4	1.0
17	26.76	2	1245	0.7734	0.0080	1.6847	0.0066	64.0	0.9
18	24.71	2	1468	0.7655	0.0083	1.6735	0.0099	63.7	1.0
19	23.88	2	1269	0.7582	0.0097	1.6864	0.0156	62.3	1.3
20	22.21	7	3326	0.7556	0.0095	1.6836	0.0122	62.1	1.2
21	12.10	13	896	0.7489	0.0105	1.6782	0.0087	61.7	1.2
22	8.43	8	1063	0.7651	0.0101	1.6788	0.0119	63.4	1.2
23	7.16	5	1313	0.7567	0.0115	1.6846	0.0139	62.2	1.4
24	6.07	7	897	0.7675	0.0137	1.6901	0.0140	63.1	1.6
25	4.01	7	563	0.7555	0.0175	1.6847	0.0138	62.1	2.0
26	3.58	4	845	0.7533	0.0170	1.6764	0.0173	62.3	2.0
27	3.27	4	821	0.7348	0.0249	1.6763	0.0192	60.3	2.8
28	2.97	3	1072	0.7227	0.0224	1.6744	0.0174	59.1	2.5
29	2.59	2	1655	0.7398	0.0209	1.6773	0.0148	60.8	2.3
30	2.21	2	1242	0.7129	0.0255	1.6696	0.0139	58.3	2.7
MEAN VALUES									
5-30				0.8017	0.0137	1.6820	0.0152	67.2	1.7

3675#5	U (ppm)	Th (ppb)	U/Th	$^{230}Th/^{238}U$	$^{230}Th/^{238}U$ error	$^{234}U/^{238}U$	$^{234}U/^{238}U$ error	Age (ka)	Age error (ka)
1	74.45	19	3962	0.5473	0.0042	1.6540	0.0049	42.7	0.4
2	68.19	8	8411	0.5574	0.0083	1.6487	0.0099	43.8	0.8
3	56.73	6	9114	0.6294	0.0134	1.6630	0.0063	50.2	1.3
4	47.30	6	7446	0.6985	0.0155	1.6621	0.0083	57.2	1.6
5	42.32	4	1050	0.7863	0.0120	1.6734	0.0149	66.0	1.6
6	38.37	3	1119	0.8324	0.0086	1.6852	0.0112	70.5	1.2
7	35.55	2	1465	0.8375	0.0101	1.6859	0.0067	71.0	1.2
8	33.52	2	1625	0.8548	0.0093	1.6904	0.0107	72.7	1.3
9	33.30	3	1090	0.8778	0.0072	1.6882	0.0107	75.5	1.1
10	32.28	2	1476	0.8746	0.0062	1.6817	0.0094	75.6	1.0
11	33.75	2	1990	0.8530	0.0068	1.6894	0.0165	72.6	1.3
12	32.58	2	2007	0.8570	0.0077	1.6872	0.0078	73.2	1.0
13	30.24	1	2053	0.8603	0.0106	1.6888	0.0099	73.5	1.4
14	27.27	2	1585	0.8684	0.0082	1.6860	0.0068	74.6	1.1
15	25.94	2	1567	0.8557	0.0082	1.6852	0.0112	73.2	1.2
16	24.93	1	2556	0.8451	0.0130	1.6847	0.0118	72.0	1.7
17	24.91	1	2502	0.8222	0.0100	1.6866	0.0063	69.3	1.2
18	23.05	1	3626	0.8358	0.0113	1.6888	0.0117	70.7	1.5
19	21.56	1	2173	0.8262	0.0080	1.6915	0.0091	69.4	1.0
20	20.31	1	1552	0.8322	0.0095	1.6917	0.0167	70.1	1.4
21	19.72	1	2411	0.8187	0.0146	1.7064	0.0278	67.7	2.2
22	19.69	1	2830	0.8080	0.0074	1.6861	0.0113	67.7	1.0
23	18.82	1	3367	0.8073	0.0079	1.6746	0.0132	68.3	1.2
24	18.26	1	1927	0.8028	0.0075	1.6792	0.0105	67.5	1.0
25	17.53	1	2329	0.8008	0.0102	1.6882	0.0064	66.8	1.2
26	16.43	1	1982	0.8079	0.0103	1.6917	0.0077	67.4	1.2
27	14.39	1	1501	0.8072	0.0094	1.6860	0.0132	67.6	1.3
28	10.81	1	8682	0.8119	0.0101	1.6874	0.0129	68.1	1.3
29	9.63	1	6644	0.8100	0.0107	1.6954	0.0113	67.4	1.3
30	9.14	1	8014	0.8081	0.0137	1.6825	0.0139	67.9	1.7
MEAN VALUES									
6-30				0.8392	0.0144	1.6874	0.0153	71.1	1.9

3675#6	U (ppm)	Th (ppb)	U/Th	$^{230}Th/^{238}U$	$^{230}Th/^{238}U$ error	$^{234}U/^{238}U$	$^{234}U/^{238}U$ error	Age (ka)	Age error (ka)
1	76.83	11	7262	0.4753	0.0142	1.6530	0.0051	36.2	1.3
2	67.12	6	1086	0.5164	0.0068	1.6578	0.0123	39.7	0.7
3	63.03	7	9262	0.5360	0.0068	1.6572	0.0039	41.5	0.6
4	53.40	6	9030	0.6315	0.0155	1.6663	0.0084	50.3	1.6
5	47.14	4	1266	0.7257	0.0141	1.6735	0.0110	59.5	1.6
6	42.65	3	1293	0.7690	0.0090	1.6757	0.0050	64.0	1.0

7	40.02	3	1340	0.8297	0.0122	1.6803	0.0178	70.5	1.7
8	38.80	2	1670	0.8562	0.0078	1.6840	0.0100	73.3	1.1
9	36.41	2	2159	0.8708	0.0134	1.6868	0.0158	74.8	1.9
10	35.03	2	1790	0.8810	0.0087	1.6841	0.0106	76.2	1.2
11	34.68	2	1756	0.8966	0.0128	1.6925	0.0148	77.5	1.8
12	33.32	2	1818	0.9060	0.0089	1.6809	0.0091	79.4	1.3
13	30.97	2	1775	0.9079	0.0085	1.6863	0.0109	79.3	1.3
14	28.12	2	1582	0.8927	0.0089	1.6786	0.0083	78.0	1.2
15	25.78	2	1359	0.8953	0.0098	1.6778	0.0098	78.3	1.4
16	23.78	1	1965	0.8768	0.0109	1.6750	0.0130	76.3	1.6
17	21.87	1	2389	0.8852	0.0132	1.6860	0.0115	76.6	1.7
18	20.16	1	2144	0.8767	0.0125	1.6867	0.0105	75.5	1.6
19	19.88	1	2676	0.8574	0.0109	1.6881	0.0119	73.2	1.5
20	18.92	1	2179	0.8605	0.0097	1.6928	0.0105	73.2	1.3
21	17.80	1	1407	0.8454	0.0062	1.6846	0.0087	72.0	0.9
22	16.52	1	1433	0.8354	0.0126	1.6931	0.0158	70.4	1.7
23	16.42	1	2041	0.8389	0.0125	1.6902	0.0100	70.9	1.5
24	13.49	1	1810	0.8522	0.0131	1.6874	0.0123	72.6	1.7
25	12.28	1	1640	0.8742	0.0148	1.6841	0.0112	75.4	1.9
26	12.87	1	1602	0.8535	0.0161	1.7026	0.0164	71.9	2.1
27	11.94	1	8285	0.8409	0.0082	1.6995	0.0103	70.6	1.1
28	9.69	2	5389	0.8488	0.0108	1.6870	0.0103	72.2	1.4
29	8.40	2	4912	0.8500	0.0137	1.6845	0.0140	72.5	1.8
30	7.84	1	7437	0.8594	0.0136	1.6788	0.0122	74.0	1.8
MEAN VALUES									
5-30				0.8739	0.0150	1.6859	0.0154	75.2	2.0

3675#7	U (ppm)	Th (ppb)	U/Th	$^{230}Th/^{238}U$	$^{230}Th/^{238}U$ error	$^{234}U/^{238}U$	$^{234}U/^{238}U$ error	Age (ka)	Age error (ka)
1	121.03	24	5024	0.3769	0.0033	1.6413	0.0025	28.0	0.3
2	115.97	15	7838	0.3748	0.0040	1.6423	0.0033	27.8	0.3
3	108.17	10	1073	0.4193	0.0081	1.6487	0.0030	31.4	0.7
4	86.57	9	9184	0.4735	0.0067	1.6484	0.0031	36.1	0.6
5	71.74	10	6855	0.5251	0.0146	1.6540	0.0038	40.6	1.3
6	57.44	13	4434	0.6336	0.0108	1.6660	0.0045	50.5	1.1
7	50.64	91	554	0.6722	0.0060	1.6690	0.0056	54.2	0.6
8	47.15	517	91	0.6413	0.0102	1.6627	0.0040	51.4	1.0
9	43.06	307	140	0.6922	0.0108	1.6750	0.0103	55.9	1.2
10	39.06	133	295	0.7215	0.0081	1.6787	0.0107	58.8	1.0
11	36.80	67	552	0.7133	0.0051	1.6666	0.0068	58.5	0.6
12	30.29	51	594	0.8452	0.0279	1.6882	0.0095	71.8	3.2
13	28.00	31	895	0.9252	0.0086	1.6917	0.0068	81.0	1.2
14	26.21	23	1162	0.9647	0.0104	1.7002	0.0094	85.3	1.5
15	23.79	17	1392	0.9813	0.0111	1.6944	0.0076	87.9	1.6
16	22.45	19	1199	0.9855	0.0112	1.6979	0.0067	88.1	1.5
17	21.92	22	982	0.9827	0.0079	1.6945	0.0066	88.0	1.2
18	21.01	17	1246	0.9752	0.0084	1.6878	0.0098	87.6	1.3
19	19.25	22	866	0.9940	0.0088	1.6967	0.0067	89.3	1.3
20	18.50	43	426	0.9641	0.0113	1.6841	0.0127	86.5	1.8
21	17.60	22	801	0.9799	0.0115	1.6883	0.0095	88.2	1.7
22	17.30	30	573	0.9743	0.0093	1.6958	0.0069	86.9	1.3
23	17.07	23	738	0.9737	0.0103	1.6907	0.0068	87.2	1.4
24	16.51	22	765	0.9703	0.0129	1.6869	0.0082	87.0	1.8
25	15.15	14	1054	0.9627	0.0098	1.6961	0.0058	85.4	1.3
26	13.61	8	1714	0.9810	0.0110	1.6945	0.0084	87.8	1.6
27	12.93	10	1267	0.9869	0.0123	1.6882	0.0095	89.1	1.8
28	11.39	19	614	0.9928	0.0109	1.6940	0.0073	89.4	1.5
29	7.08	76	93	0.9768	0.0133	1.6930	0.0112	87.4	1.9
30	5.92	53	112	0.9350	0.0144	1.6934	0.0148	82.1	2.1
MEAN VALUES									
15-30				0.9778	0.0168	1.6923	0.0153	87.6	2.5

Supplementary Table 13. U-series results on sample WU1601. All errors are 2-σ.

3672	U (ppm)	Th (ppb)	U/Th	$^{230}Th/^{238}U$	$^{230}Th/^{238}U$ error	$^{234}U/^{238}U$	$^{234}U/^{238}U$ error	Age (ka)	Age error (ka)
MEAN VALUES									
Enamel	0.83±0.28			0.8346	0.0533	1.5042	0.0329	83.5	8.1
Dentine	109±6			0.7295	0.0173	1.5742	0.0124	65.0	2.1

Supplementary Table 14. Combined US-ESR age results obtained for sample WU1601.

See Methods and Supplementary Information 2 for discussion.

Internal dose rate (μGy/a)	Beta dose rate dentine (μGy/a)	Beta dose rate sediment (μGy/a)	Gamma dose rate (μGy/a)	Cosmic dose rate (μGy/a)	Total dose rate (μGy/a)	Enamel thickness (μm)	Removed surface layer(μm) on each side	D_E (Gy)	p-parameter		US-ESR age (ka)
									enamel	dentine	
241±75	260±48	4±0	180±10	254±25	939±93	3244±100	Ext.: 176±50; Int.:181±50	97.1±1.9	-0.83	-0.53	103±10/-9

Supplementary Table 15. **The number of single grains which were measured, rejected after application of the criteria outlined in Supplementary section 3.2, and accepted for inclusion in the calculation of D_b**. Samples indicated (DR) represent dose recovery data.

Sample	PD15 (DR)	PD17 (DR)	PD15	PD17	PD40	PD41
Total number of grains measured						
	2500	2500	3600	3400	2800	3100
Grains rejected for the following reasons						
T_n signal <3*background	2358	2363	3373	3223	2606	2951
Poor recycling ratio	11	25	34	21	16	30
Depletion by IR	51	48	79	50	73	55
Recuperation	36	29	58	53	28	17
Oversaturation	3	1	0	5	12	7
$D_e < 2\sigma$ above 0 Gy	0	0	6	6	2	5
Sum of rejected grains						
	2459	2466	3550	3358	2737	3065
Acceptable individual D_e values						
	41	34	50	42	63	35

Supplementary Table 16. Sample depths, water content and dose rate for Al Wusta samples.

Sample	Depth (m)	Moisture (%)	Dose rate (Gy/ka)			Total dose rate, (Gy/ka)
			Beta	Gamma	Cosmic	
PD15	0.95±0.10	5±2.5	0.15±0.01	0.27±0.02	0.209±0.021	0.62±0.03
PD17	0.70±0.10	5±2.5	0.16±0.01	0.24±0.01	0.222±0.022	0.62±0.03
PD40	0.65±0.10	5±2.5	0.10±0.01	0.18±0.01	0.219±0.022	0.50±0.03
PD41	1.20±0.10	5±2.5	0.10±0.01	0.25±0.01	0.198±0.020	0.54±0.03

Supplementary Table 17. OSL Summary dating results and ages. Uncertainties in the age estimates are based on the propagation, in quadrature, of errors associated with individual errors for all measured quantities. In addition to uncertainties calculated from counting statistics, errors due to (1) beta source calibration (3 %); (2) single-grain instrument reproducibility (1.5 %); (3) dose rate conversion factors (3 %) and attenuation factors (3 %) have been included.

Sample	**D_b calculation method (n)**	**D_b (Gy)**	**OD (%)**	**Total dose rate, D_r (Gy/ka)**	**Age (ka)**
PD15	CAM (50)	57.4±3.0	22±4	0.62±0.03	92.0±6.3
PD17	CAM (42)	53.0±2.5	16±3	0.62±0.03	85.3±5.6
PD40	CAM (63)	49.6±2.5	26±3	0.50±0.03	98.6±7.0
PD41	CAM (35)	50.2±2.8	20±4	0.54±0.03	92.2±6.8

Supplementary Table 18. Quantification of bulk mineralogy from XRD data. Note that in all cases calcite makes up at least 85% of the crystalline mineral fraction. Gypsum and halite are below the detection limit of the instrumentation except in PD15-30. The absence of any saline tolerant diatom species at this level makes it unlikely that halite was precipitating in this system and it is more likely that this reflects aeolian dust blown onto the exposure. There is no evidence for Halite in any of the thin sections.

Sample ID	Calcite %	Quartz %	Gypsum %	Halite %
PD15_10	93.9	3.5	1.6	1
PD15_30	92.4	2	0.8	4.7
PD15_40	96.7	1.7	0.7	0.9
PD15_50	97.4	1.8	0.7	0.2
PD16_30	95.9	2.2	1.5	0.3
PD16_40	96.6	1.7	1.4	0.3
PD16_80	97.3	1.4	1.1	0.2
PD17_20	93.8	3.3	1.3	1.6
PD17_30	96.7	1.8	0.9	0.6
PD17_40	87.3	11	0.7	1

Supplementary Table 19. Taxonomy of Al Wusta vertebrate fossils.

Class	Order	Family	Taxon	Common name
Reptilia	Squamata	Varanidae	*Varanus*	Monitor lizard
Aves			Aves gen. et sp. indet. (small)	Small bird
			Aves gen et sp. indet (medium)	Medium bird
	Struthioniformes	Struthionidae	*Struthio* sp.	Ostrich
Mammalia	Primates	Hominidae	*Homo sapiens*	Human
	Rodentia		Myomorpha gen. et sp. indet.	Rodent
	Artiodactyla	Hippopotamidae	*Hippopotamus* sp.	Hippopotamus
		Bovidae	cf. *Pelorovis*	Pelorovis
			cf. *Kobus* sp.	Kobus
			Large bovid gen. et sp. indet.	Large bovid
			Medium bovid gen. et sp. indet.	Medium bovid
			Small bovid gen. et sp. indet.	Small bovid

Supplementary Table 20. Number of Identified Specimens for small, medium and large-sized fossil vertebrates from Al Wusta.

Element	Small	Medium	Large
Horn core	2	1	-
Crania	2	-	-
Mandible	2	4	-
Isolated teeth	5	10	2
Vertebrate	2	7	4
Ribs	7	12	4
Scapula	-	1	-
Pelvis	-	2	1
Humerus	2	3	2
Femur	-	-	-
Radius	-	2	-
Tibia	2	-	-
Carpals/Tarsals	2	4	1
Metapodials	1	-	2
Phalanges	1	2	3
Long bone shaft	11	46	7

ones

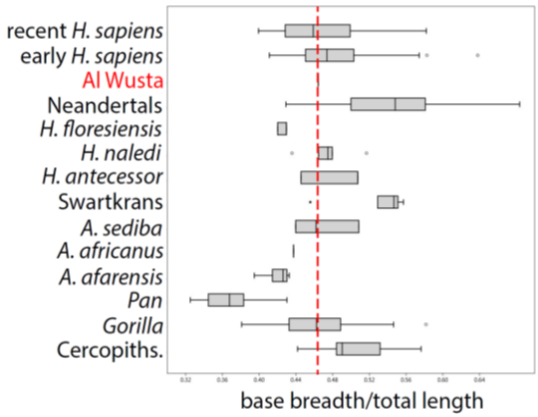

base breadth/total length

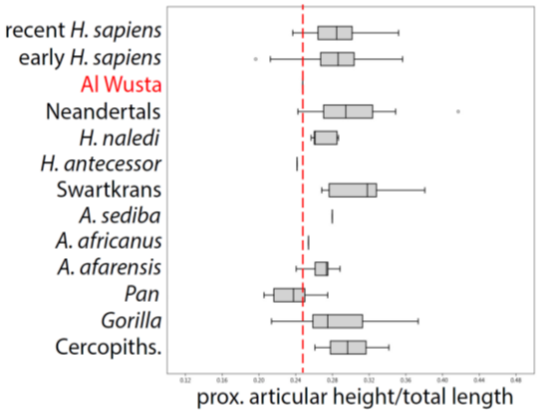

prox. articular height/total length

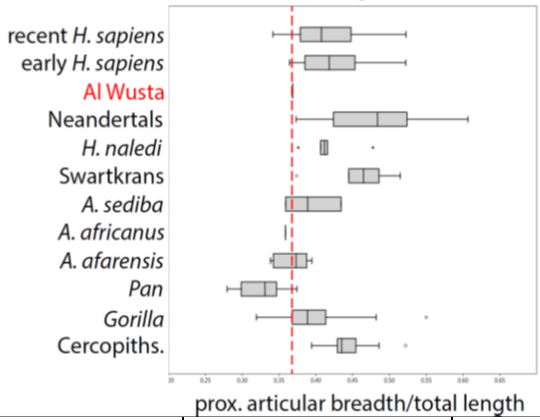

prox. articular breadth/total length

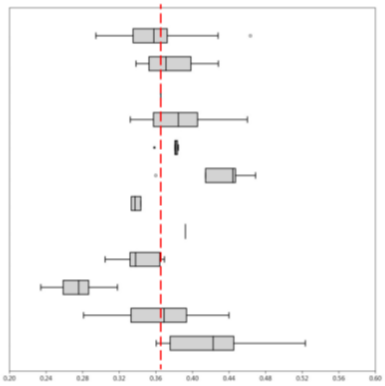
prox. shaft breadth/total length

263 1.7 1.2

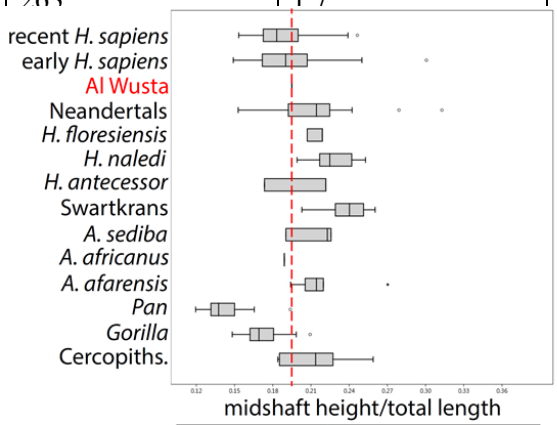

midshaft height/total length

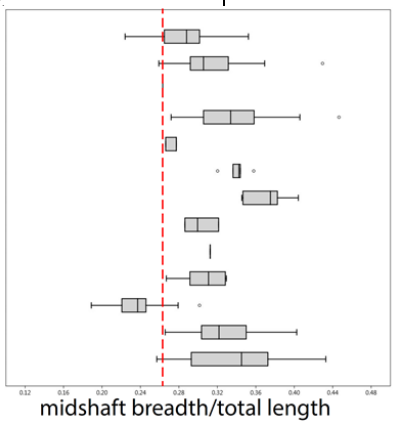
midshaft breadth/total length

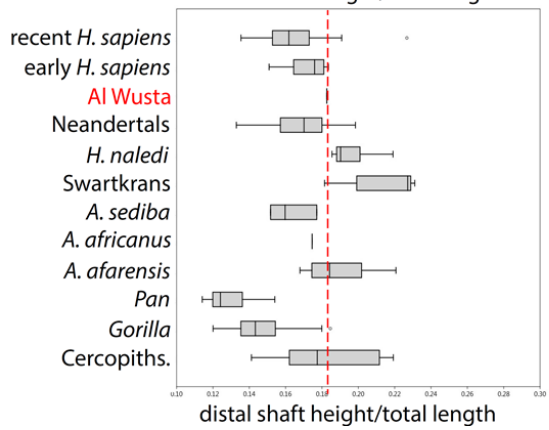

distal shaft height/total length

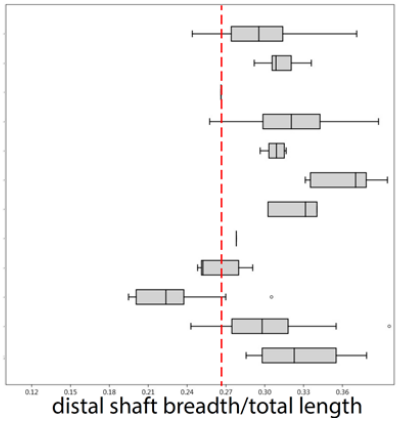
distal shaft breadth/total length

1. **AW-1 geometric morphometric analysis (see main text for methods and summary results)**

Supplementary Figure 1. Box-and-whisker plots of intermediate phalanx shape ratios of Al Wusta 1 and a sample of primates, including hominins. Al Wusta-1 is highlighted in red.

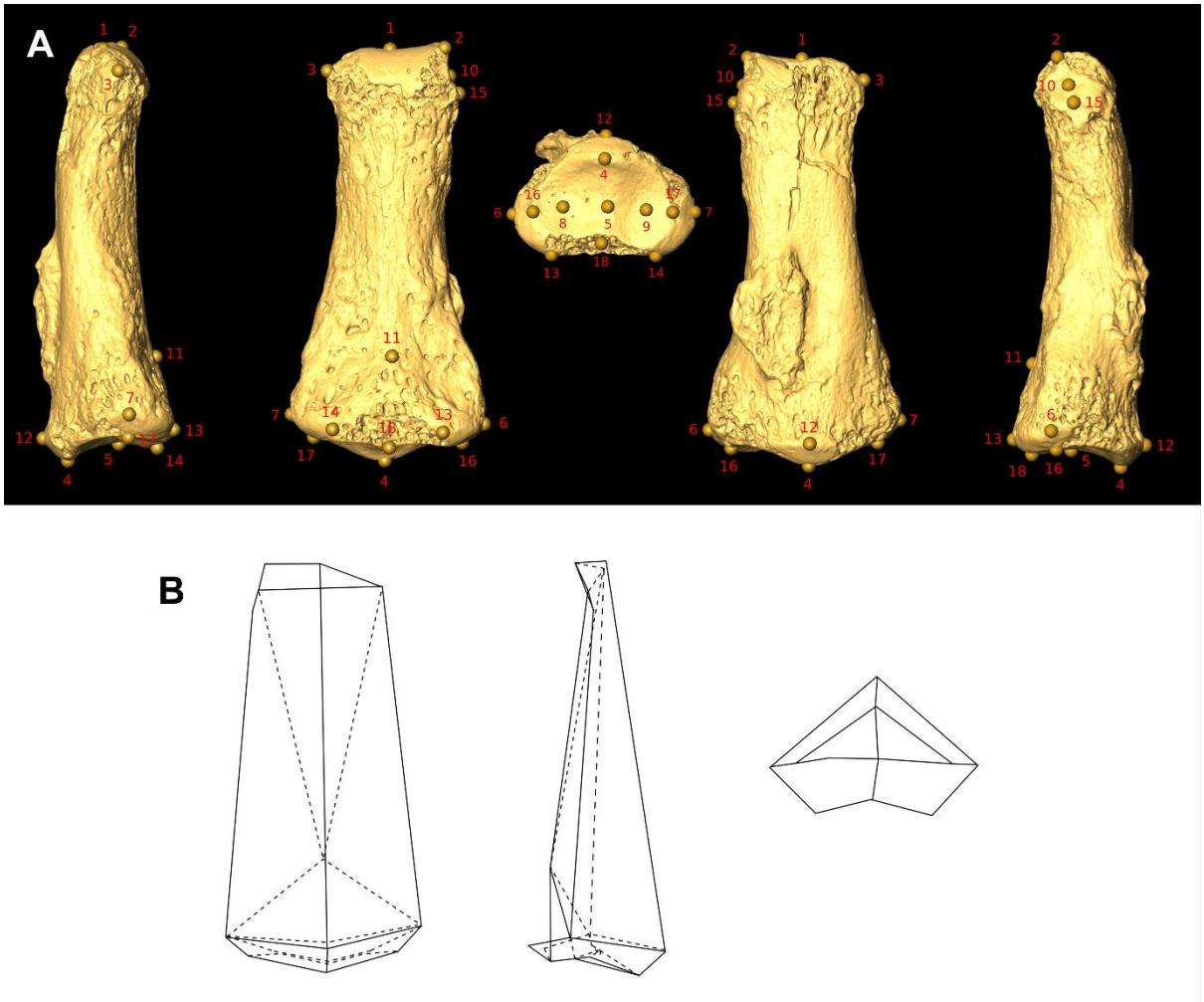

Supplementary Figure 2. Landmarks and wireframes used in geomorphomteric analyses. A: Landmarks used to analyse phalanx shape using GMM. Landmarks numbered as in Supplementary Table 4 (AW-1 shown); B: Wireframes composed of straight lines connecting landmarks shown in A. Dorsal (left), lateral (middle) and proximal (right) views. Dotted lines connect landmarks not visible when bone is present, some lines omitted in proximal view for ease of visualisation.

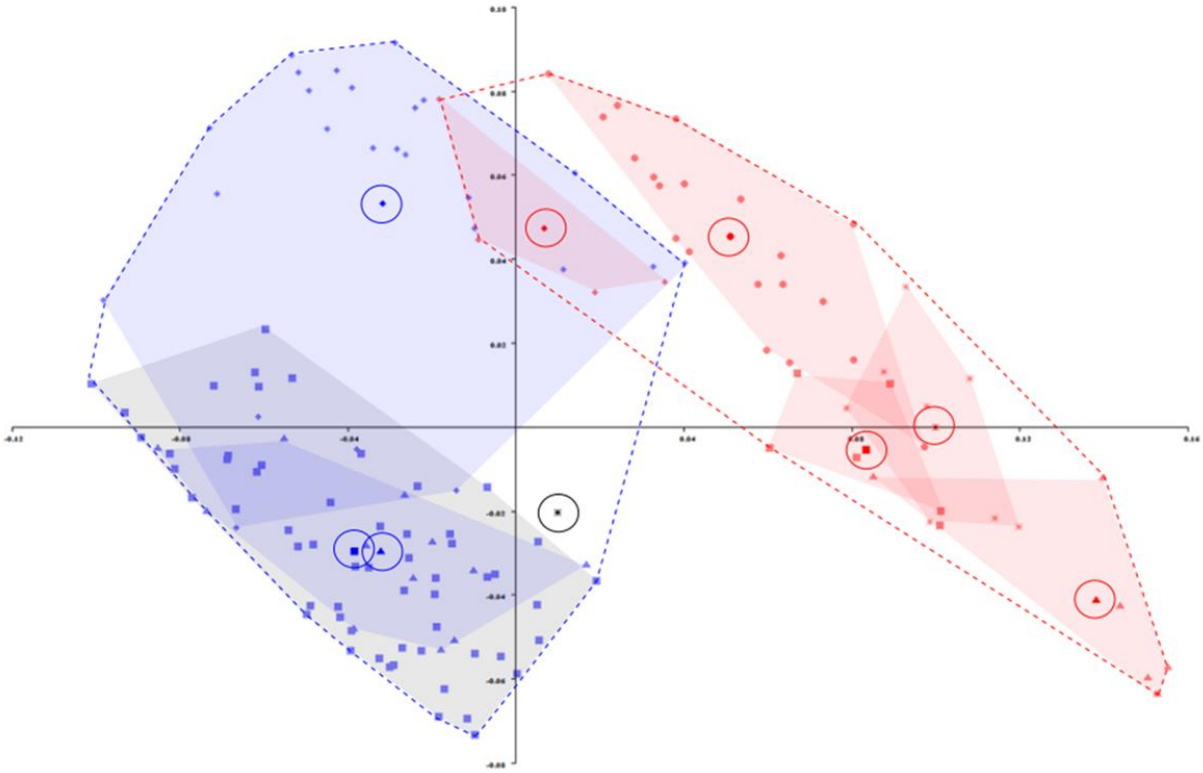

Supplementary Figure 3. Scatterplot of the first two principal component (PC) scores of the geometric morphometric analysis of the Al Wusta-1 phalanx and a sample of primates, including hominins. Non-human primates in red; *Colobus*: triangles, *Pan*: stars, *Mandrillus*: squares, *Gorilla*: circles, *Papio*: diamonds. Hominins in blue; Neanderthals: diamonds, Holocene *H. sapiens*: squares, early *H. sapiens*: triangles. AW-1 in black. Data presented are the same as Figure 3, but filled convex hulls (for visualisation of data spread only) show hominins (blue) and non-human primates (red) generic groups of non-human primates and different groups of hominins. Circled shapes show means for groups (see Supplementary Table 6).

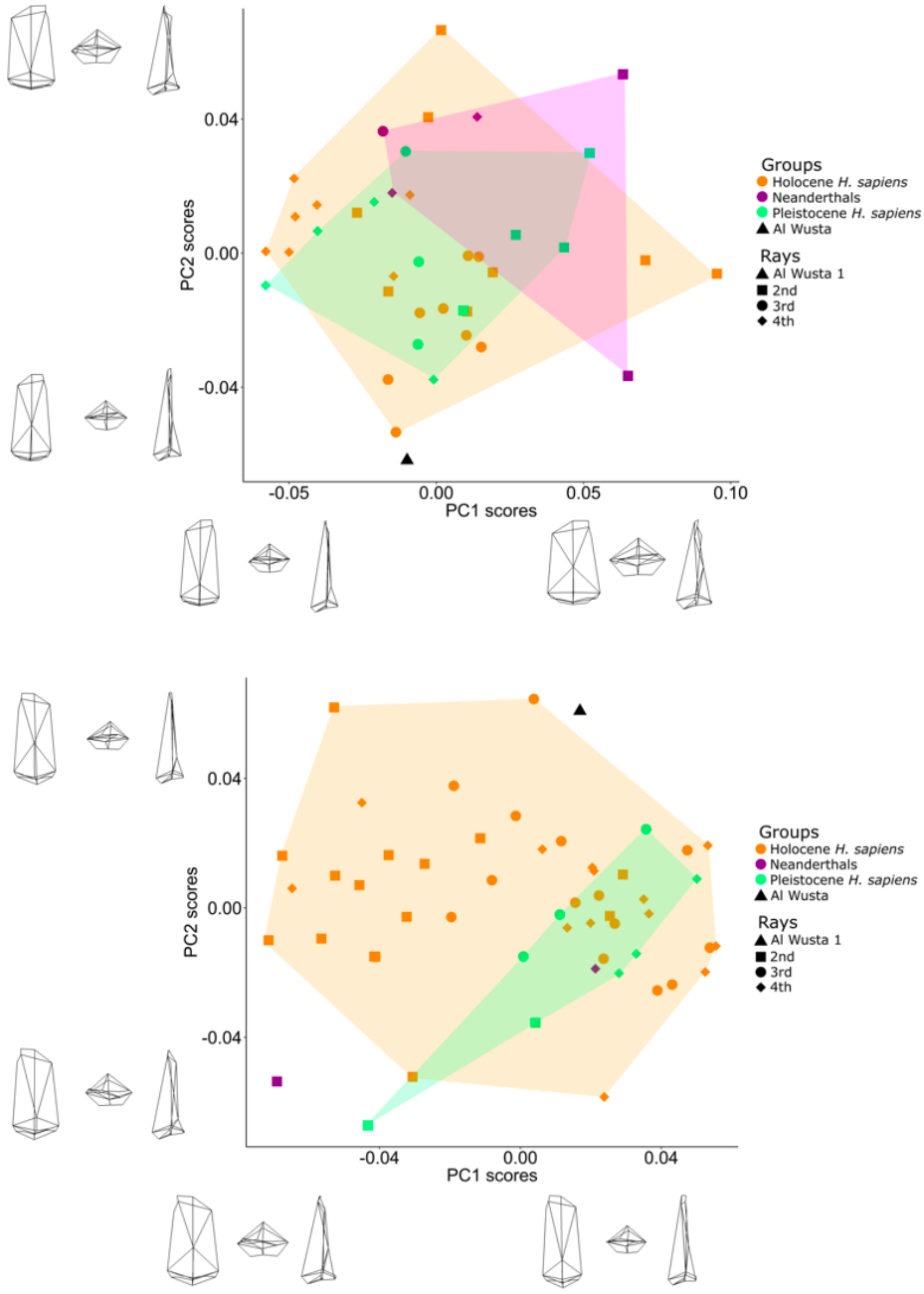

Supplementary Figure 4. Scatterplots of PC1 and PC2 scores from GMM analyses of left (top) and right (bottom) intermediate phalanges from a sample of Neanderthals and modern humans, and Al Wusta-1. Wireframes (see Supplementary Figure 2) show configurations at extremes of PC axes in dorsal (left), proximal (middle) and sagittal (right) views. Convex hulls added post-hoc for ease of visualisation.

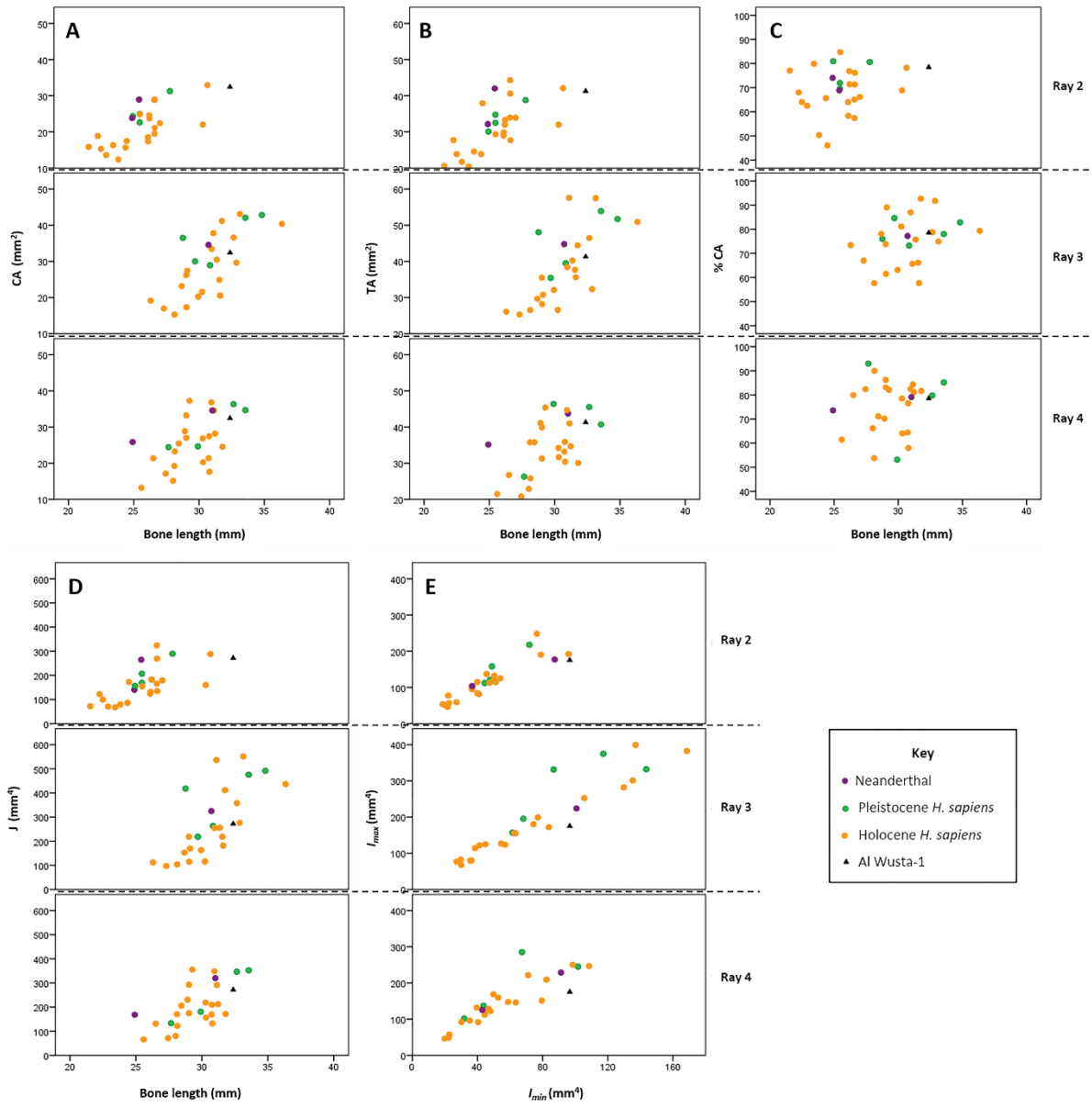

Supplementary Figure 5. Scatterplots of cross-sectional geometric properties of Al Wusta-1 and comparative modern human and Neanderthal intermediate manual phalanges from rays 2-4. Plots against bone length: A = cortical area; B = total area; C = percent cortical area; D = *J*. Plot against I_{min}: E = I_{max}.

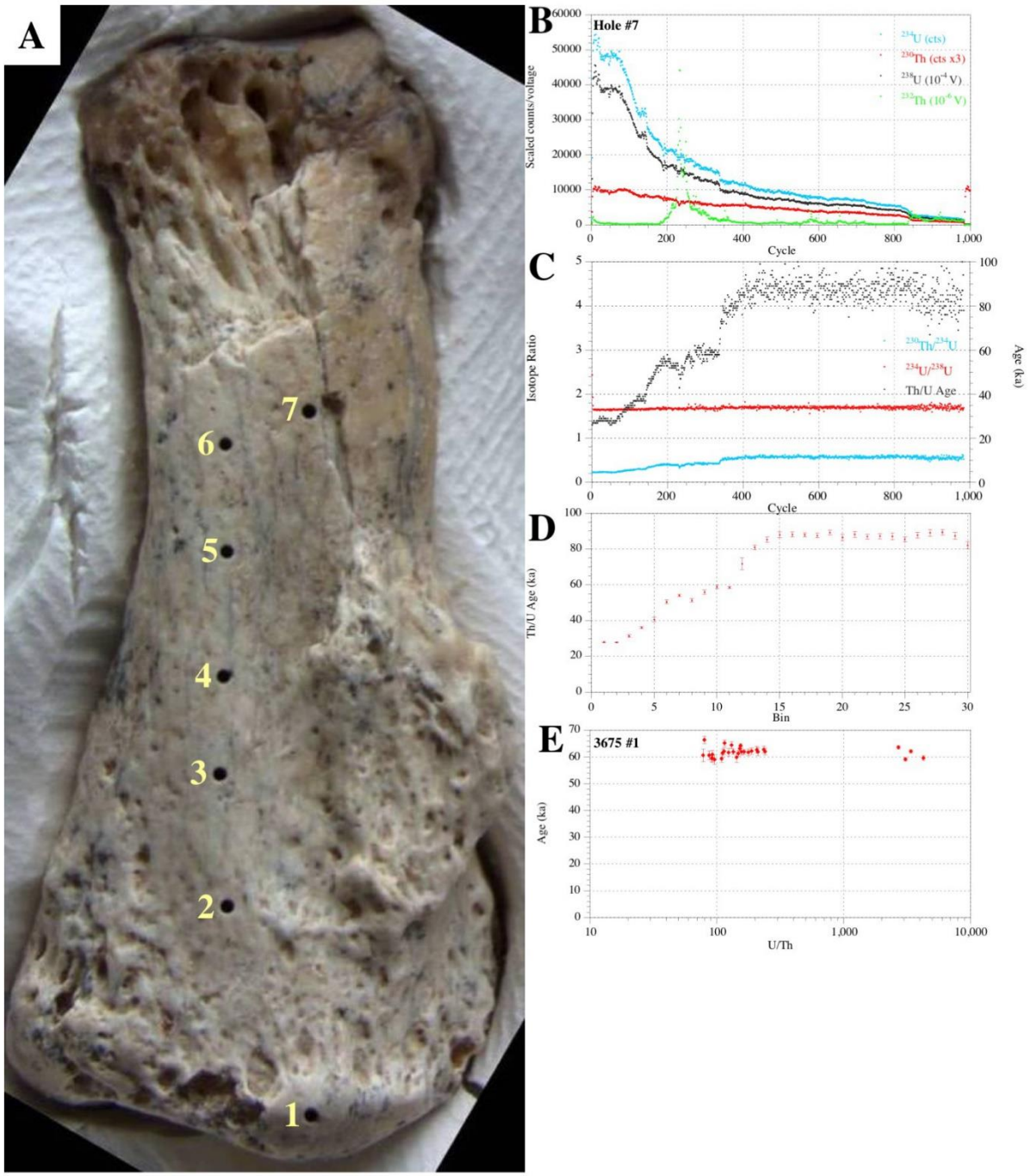

Supplementary Figure 6. AW-1 phalanx laser ablation sampling and data streams. A: Image of AW-1 (dating code 3675) with location of the laser ablation analysis holes; B: Data streams for ^{238}U, ^{234}U, ^{230}Th and ^{232}Th; C: $^{230}Th/^{234}U$ and $^{234}U/^{238}U$ activity ratios and calculated closed system age estimates; D: Average age estimates for 30 bins of 33 cycles each; E: Plot of apparent age vs elemental U/Th.

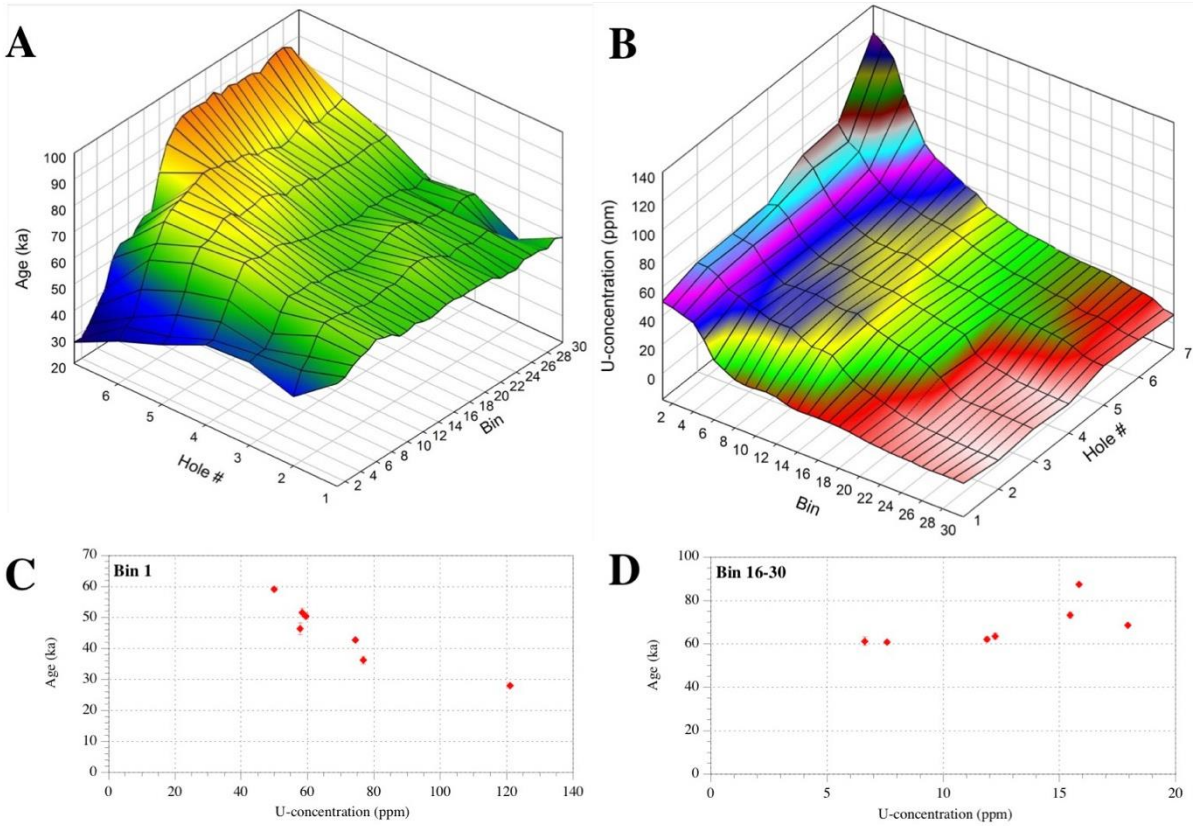

Supplementary Figure 7. Uranium concentrations and age estimates. A: Plot of all average age estimates; B: U-concentrations (these are not corrected for diminishing U-yields from deeper domains in the hole). Note the different aspect compared to A; C: Age vs U-concentration for outside (bin 1); D: Age vs U-concentration for the age plateaux (bins 16-30).

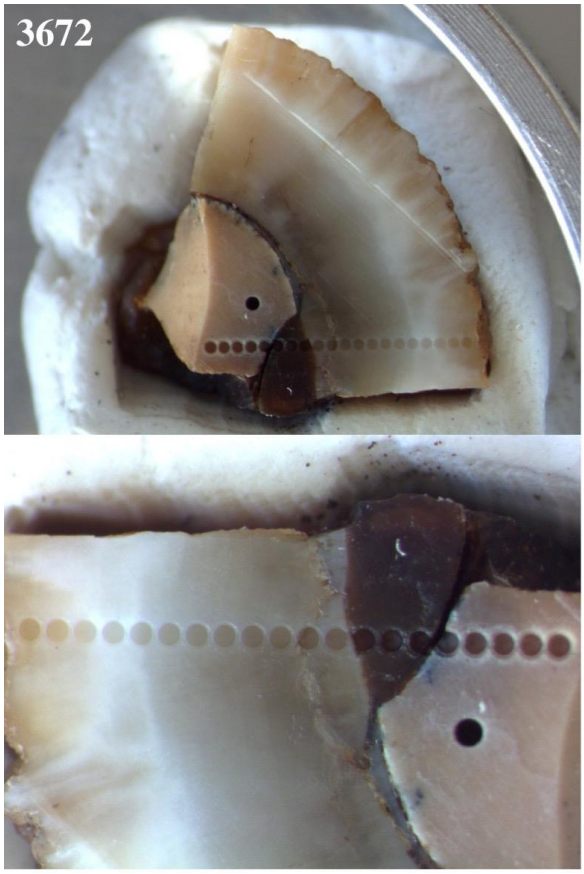

Supplementary Figure 8. Image of sample WU1601 with location of the laser ablation analysis holes.

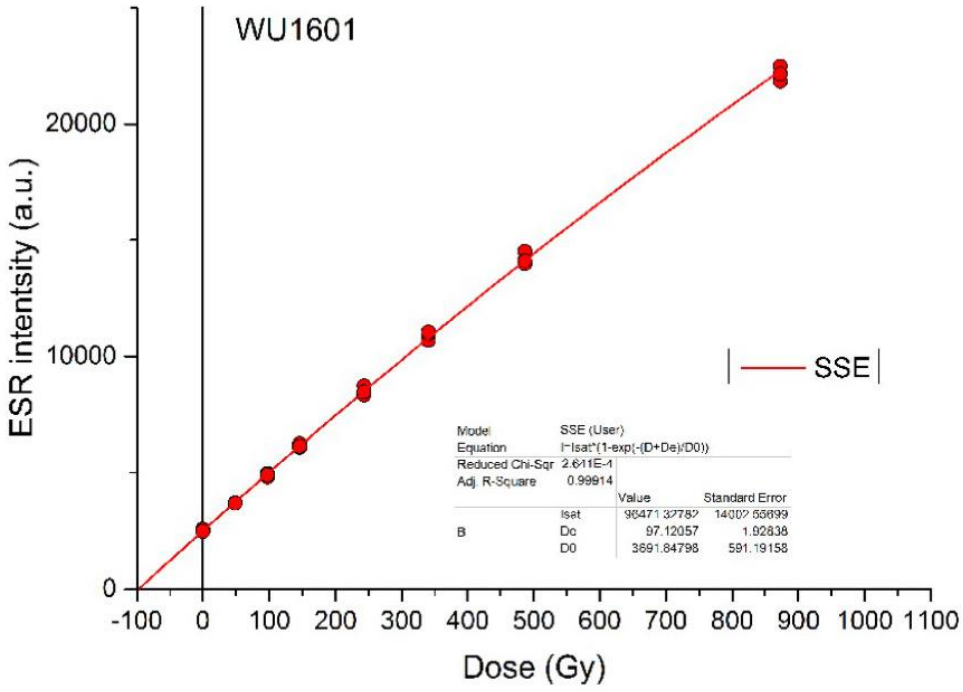

Supplementary Figure 9. ESR Dose response curve (DRC) obtained for WU1601. Final D_E values were calculated for each sample by pooling all the ESR intensities derived from the three repeated measurements in a single DRC. Fitting was performed with a SSE function and data weighting by $1/I^2$.

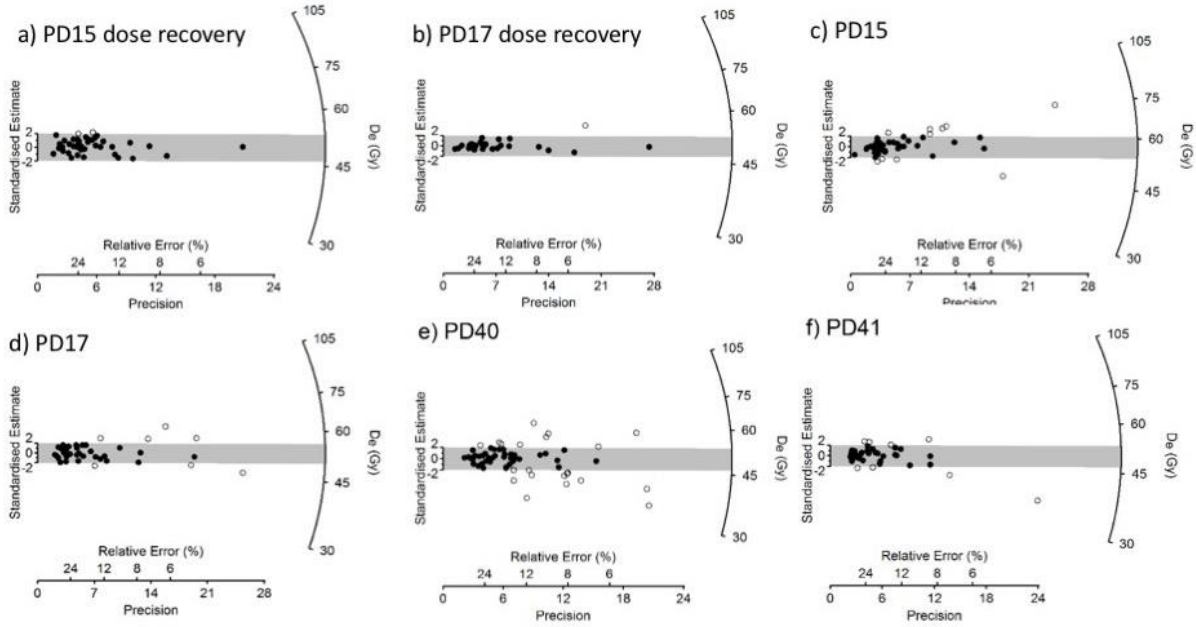

Supplementary Figure 10. OSL radial plots. Radial plots of the single-grain dose distributions for Al Wusta samples. For panels a and b the grey band is centred on the dose administered (49.8 Gy) in the dose recovery experiment. In panels c to f, the grey bar is centered on D_b determined with the Central Age Model. All points that lie within the grey band are consistent (at 2 standard errors) with either the administered dose (a,b) or D_b (c-f), and are shown as closed symbols. Open symbols denote equivalent doses which are greater than 2 standard errors from the administered dose (a,b) or D_b (c-f).

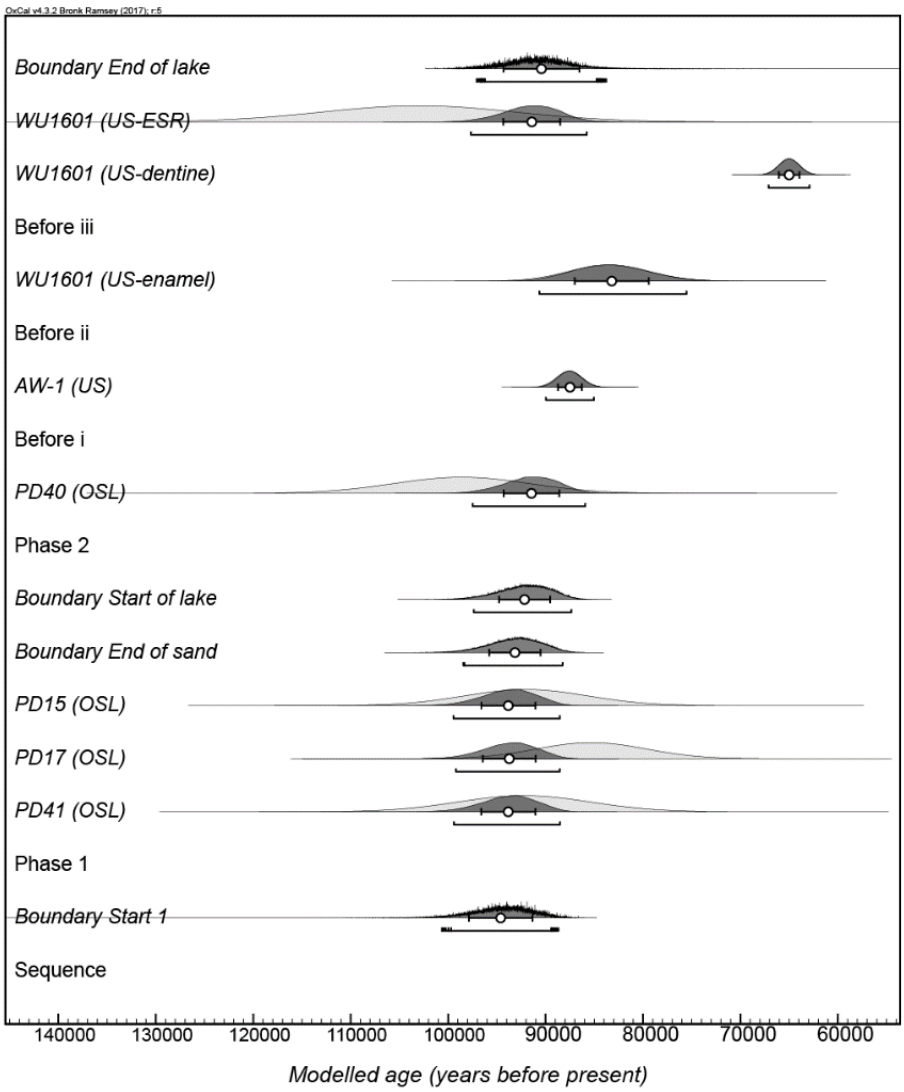

Supplementary Figure 11. Modelled ages for stratigraphic Units 1 (aeolian sand underlying the site) and 3 (waterlain sands and associated fossils overlying lacustrine marls). Two sequential phases were defined. Sample codes end with the age determination method in parentheses. The ages WU1601 (US-dentine), WU1601 (US-enamel) and AW-1 (US) are minimum age estimates, and the age model accounts for the fact that U-series ages are conventionally reported with 2 s uncertainties whereas OSL and ESR ages are reported with 1 s uncertainties. *A posteriori* densities are shown in darker shade while the likelihoods are shown in a lighter shade. Open circles underneath the *a posteriori* densities represent the mean age estimate, with 1σ uncertainty bars, while the lower bar represents the 95.4 % range.

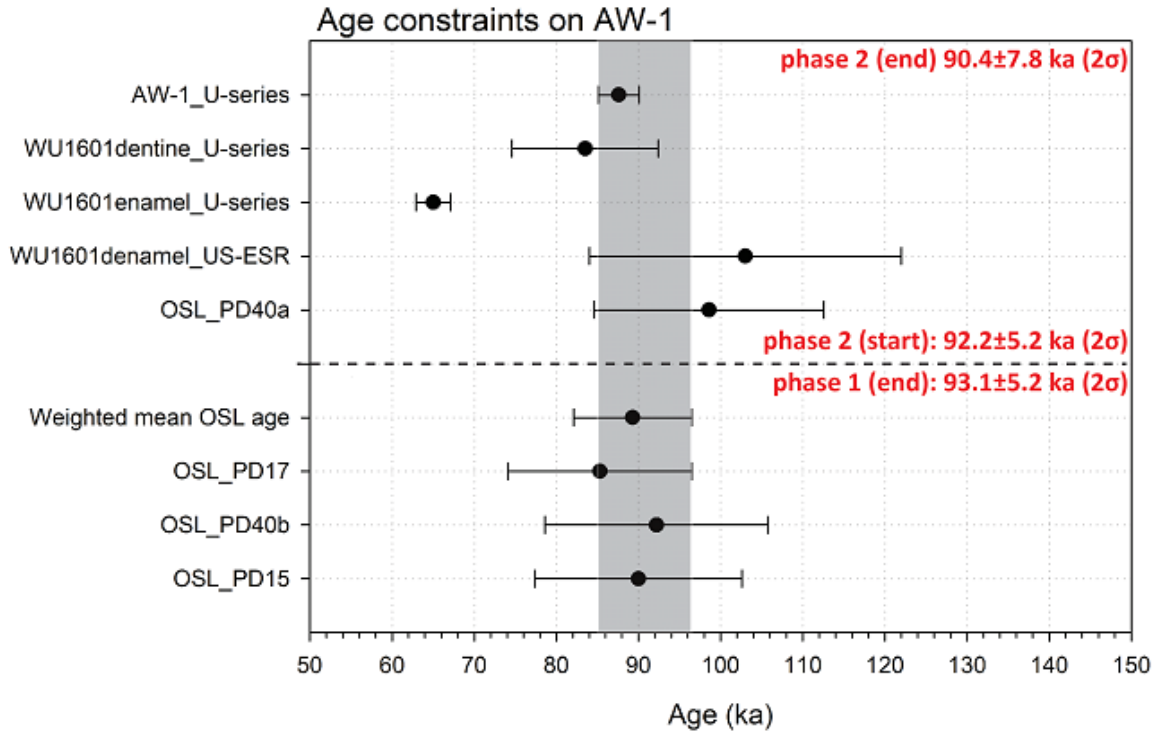

Supplementary Figure 12. Overview of the available age constraints for AW-1. In red, the modelled ages of the phase boundaries

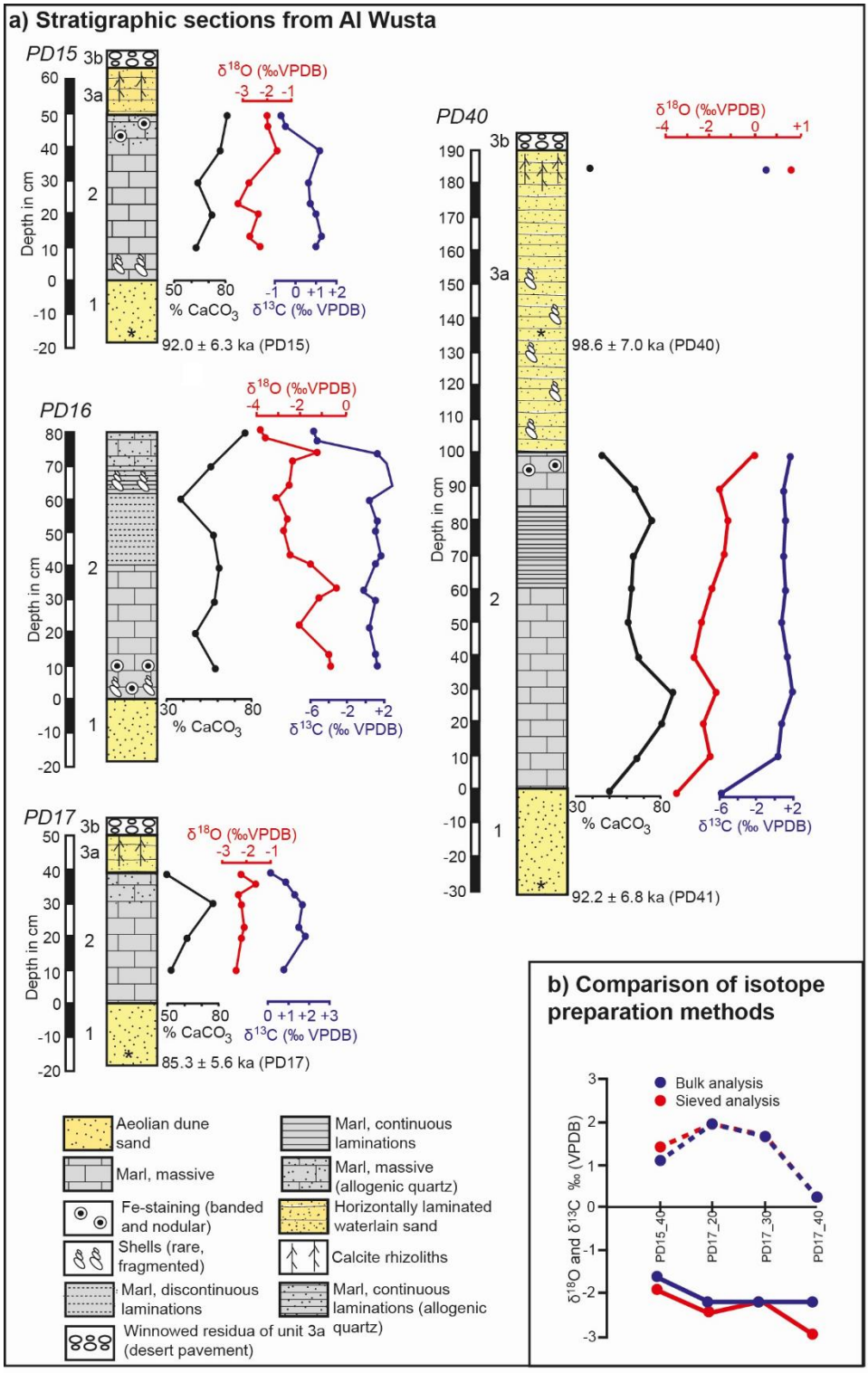

Supplementary Figure 13. Stratigraphic sections from Al Wusta. A: stratigraphic logs of lacustrine marl deposits showing the main sedimentary units and stratigraphic variations in O and C isotopes and % $CaCO_3$. To avoid wasted space at the base of each stratigraphic section, OSL ages are not presented at their true depth below the sand-marl interface. B: Diagram summarising the difference in isotope values derived from aliquots of the same sample using different preparation techniques (dashed line = carbon isotope values, solid line = oxygen isotope values), although sieving of samples is often desirable the indurated nature of many samples makes such an approach impractical.

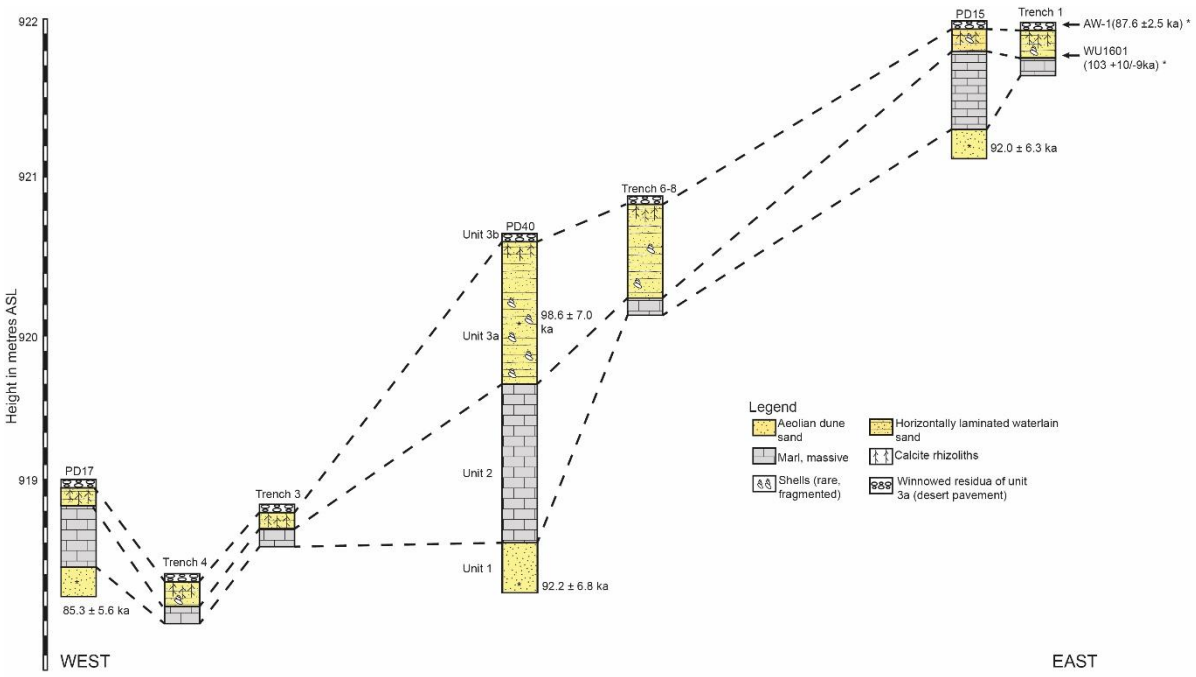

Supplementary Figure 14. Composite stratigraphic diagram showing the relationship between different sections across the site.

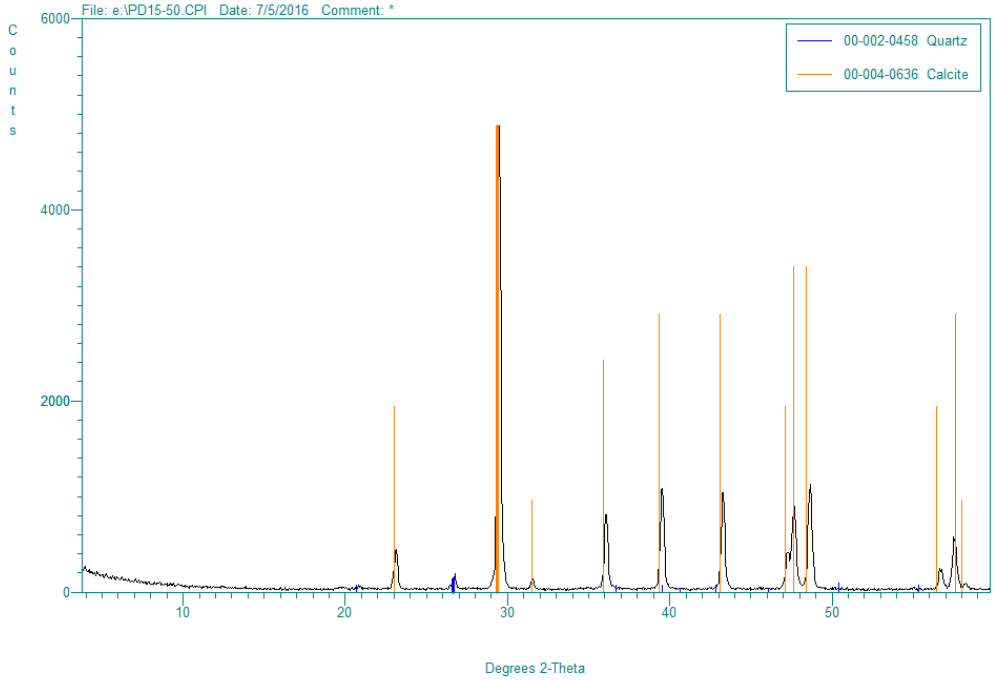

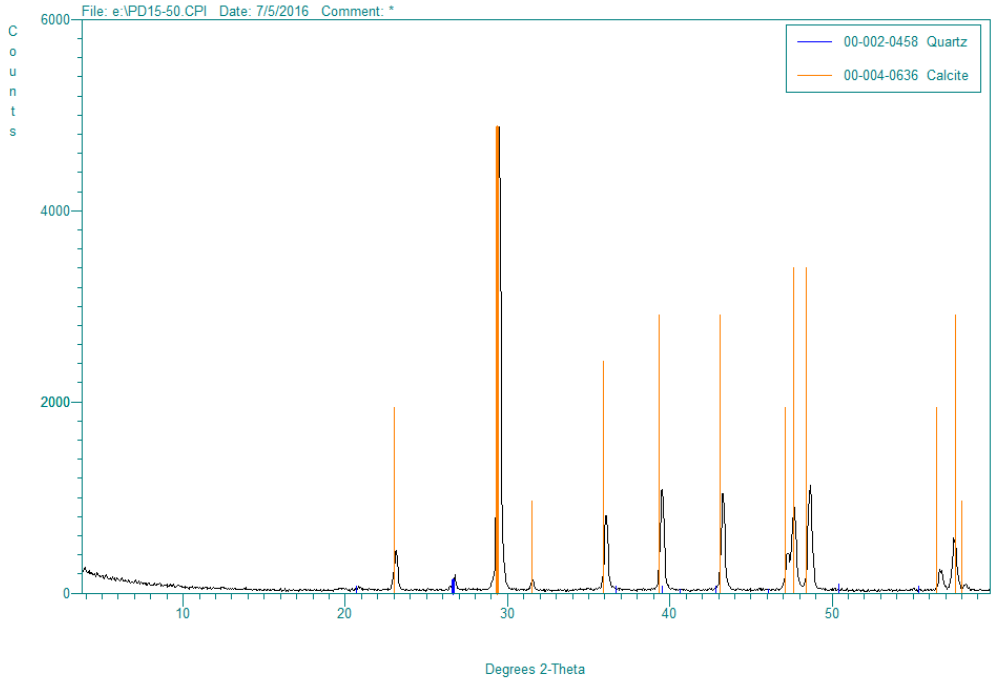

Supplementary Figure 15. XRD traces from PD15-50 (top) and PD17-40 (bottom).

Calcite peaks (orange) dominate with secondary quartz peaks (blue).

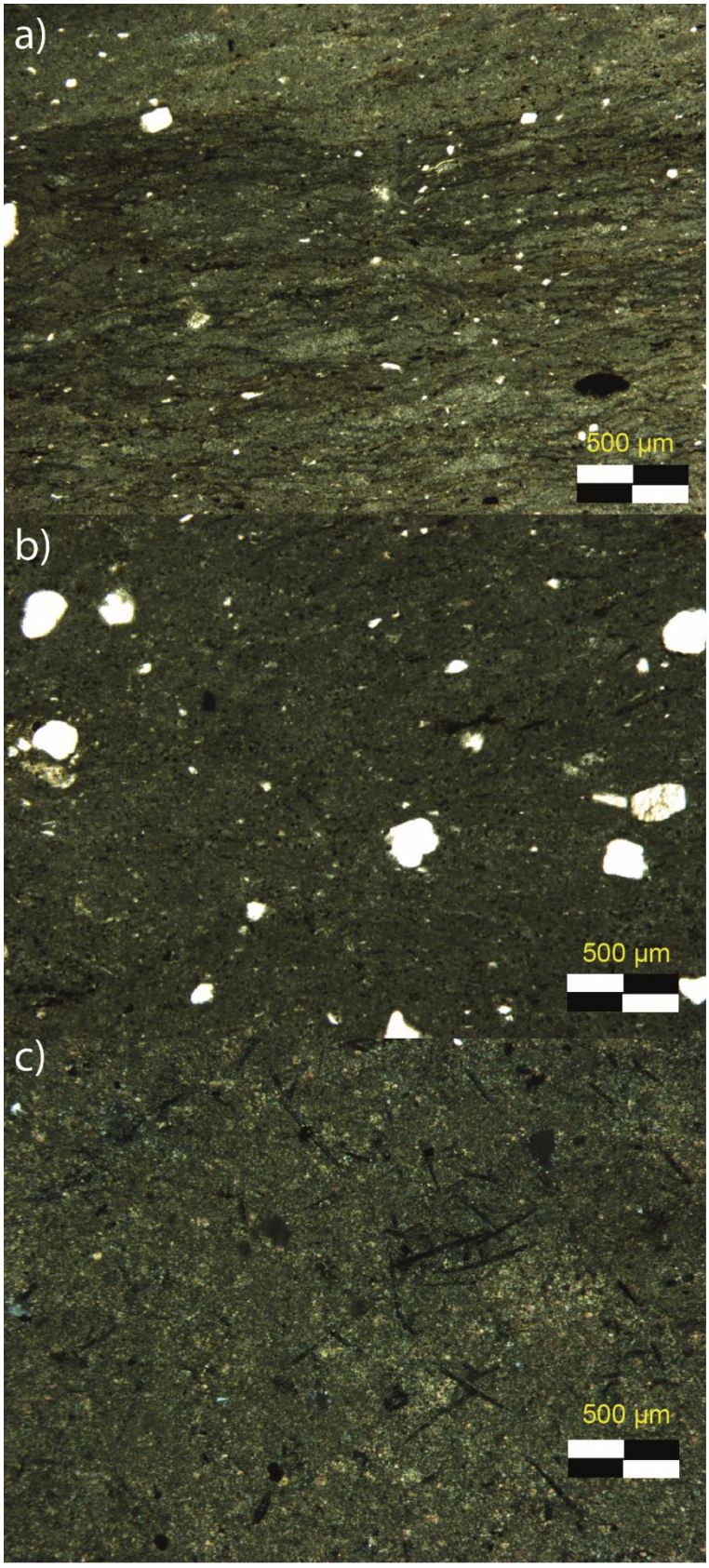

Supplementary Figure 16. Representative photo-micrographs of Al Wusta lake sediments. A) Finely laminated microsparite with silt-sized quartz grains (Allogenic). B) Massive microsparite with sand sized quartz grains (allogenic). C) freshwater sponge spicules in a microsparite/sparite massive matrix.

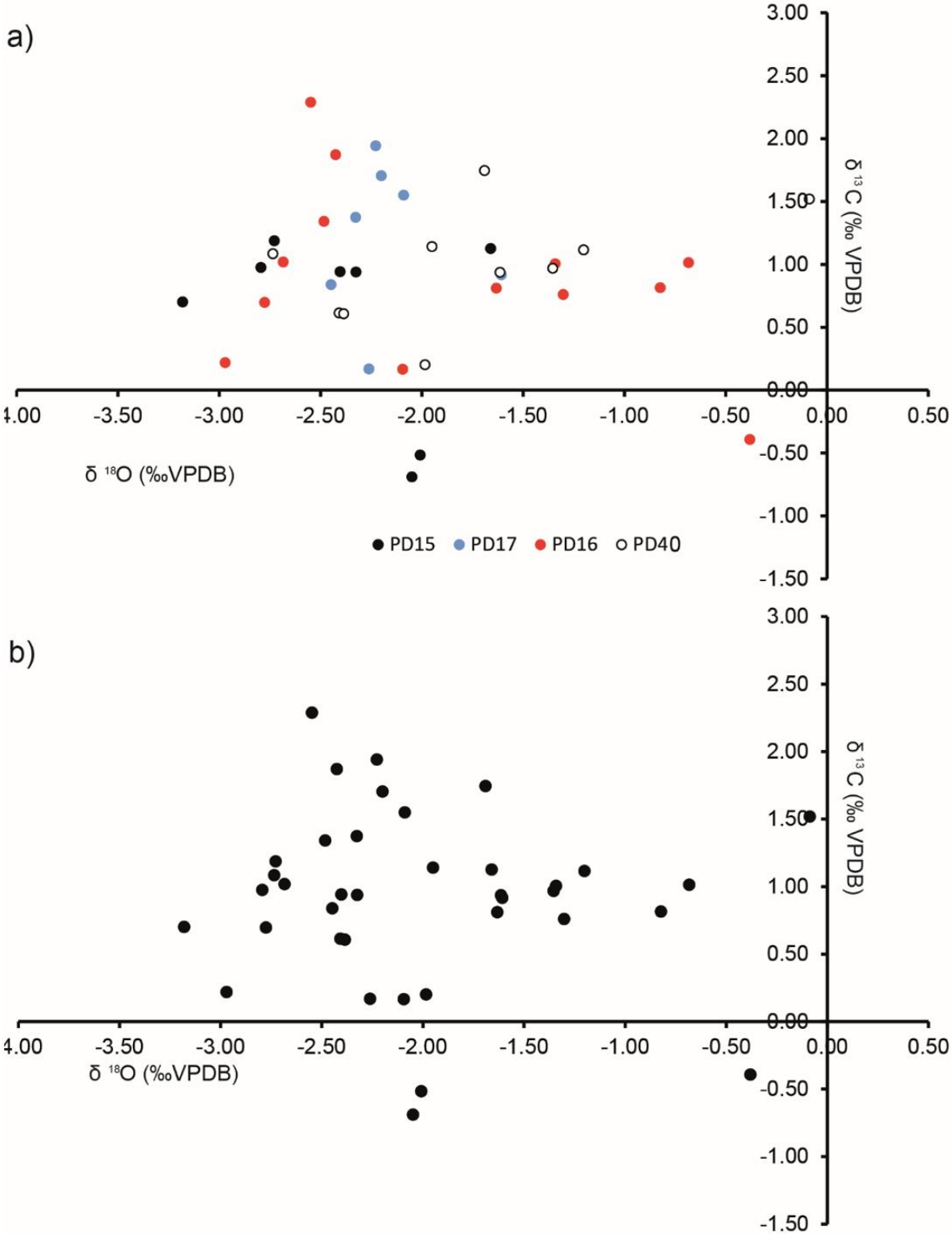

Supplementary Figure 17. Al Wusta carbonate isotopic data shown by sampling location (a) and as a single dataset (b). The overall r^2 value is 0.0521, while for each site the value is PD15 = 0.121, PD17 = 0.001, PD16 = 0.132, PD40 = 0.072. The three outlying samples are not shown but are included in the r^2 calculation.

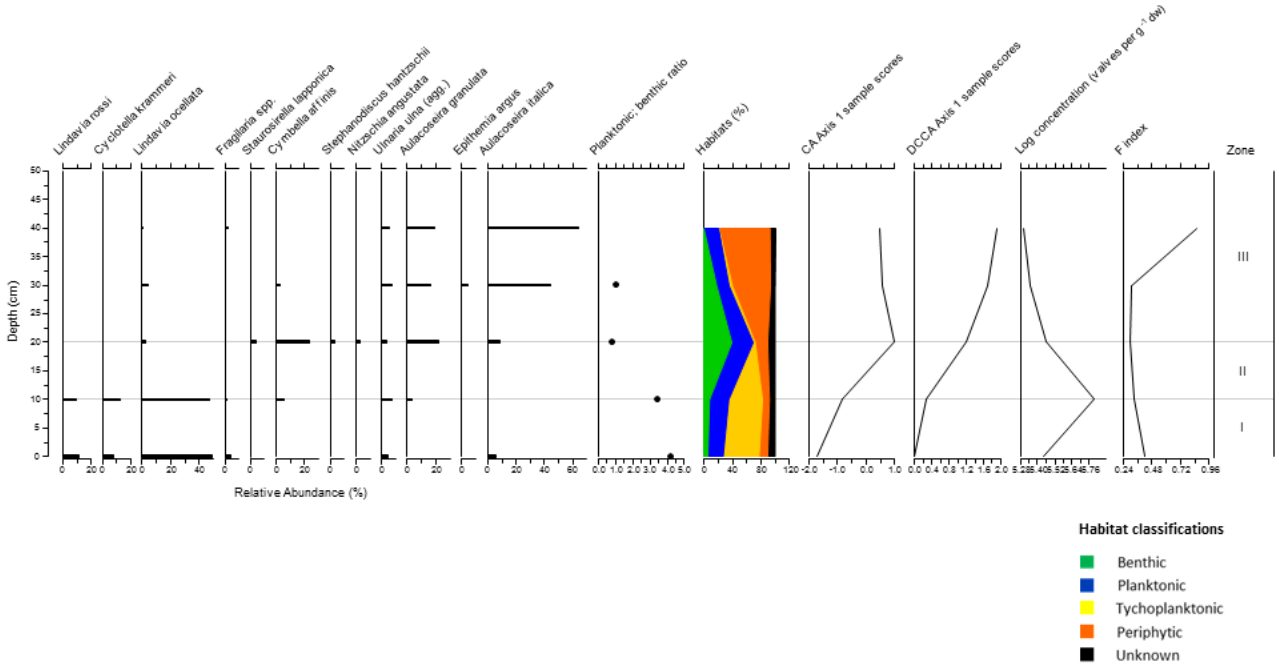

Supplementary Figure 18. Summary diagram of Al Wusta Pit 1 PD 15 diatomite diatom assemblage. All taxa with relative abundances of ≥3%. The diatoms are ordered according to their weighted averaging distribution and divided up into assemblage zones derived from the optimal-sum-of squares partitioning using the program ZONE[52]. The statistically significant zones were deduced by comparison with the Broken-stick model using the program BSTICK version 1[52]. The planktonic: benthic ratio is shown with the habitat summary, Correspondence Analysis and Detrended Canonical Correspondence Analyses axis 1 sample scores (abbreviated to CA and DCCA respectively), log concentration, F-index which ranges from 0 (most dissolved) to 1 (most pristine).

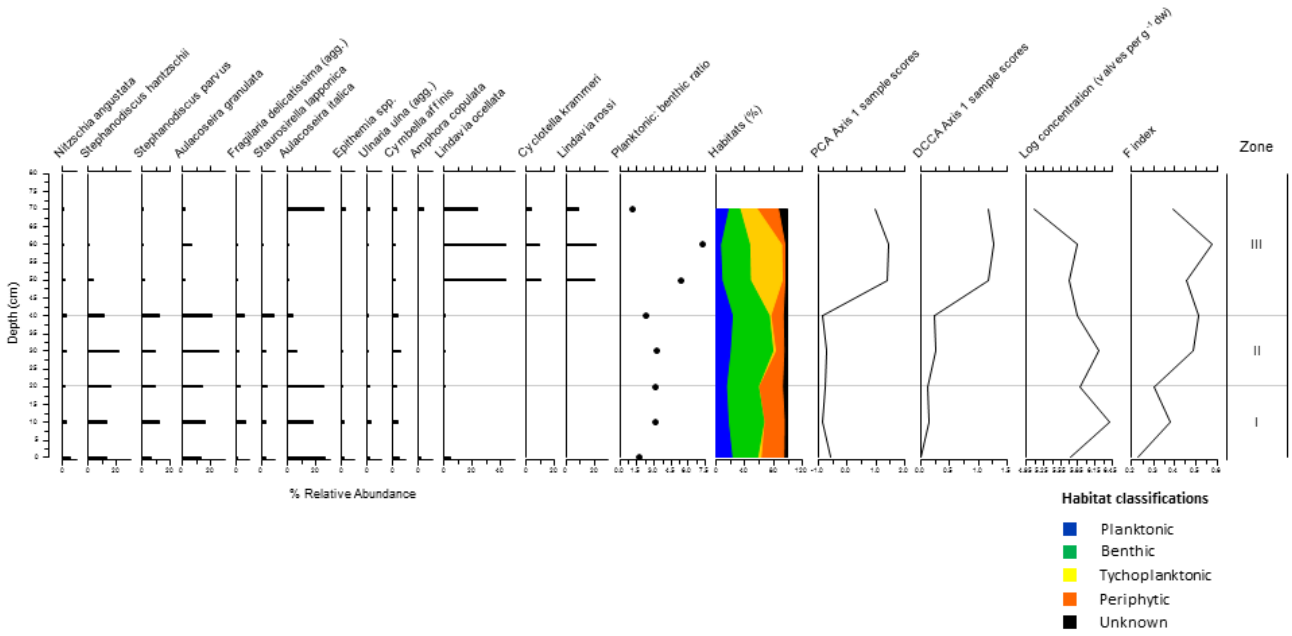

Supplementary Figure 19. Summary diagram of Al Wusta Pit 2 PD 16 diatomite diatom assemblage. All taxa with relative abundances of ≥3%. The diatoms are ordered according to their weighted averaging distribution and divided up into assemblages zones derived from the optimal-sum-of squares partitioning using the program ZONE[52]. The statistically significant zones were deduced by comparison with the Broken-stick model using the program BSTICK version 1[52]. The planktonic: benthic ratio is shown with the habitat summary, Principal Component Analysis and Detrended Canonical Correspondence Analyses axis 1 sample scores (abbreviated to PCA and DCCA respectively), log concentration, F-index which ranges from 0 (most dissolved) to 1 (most pristine).

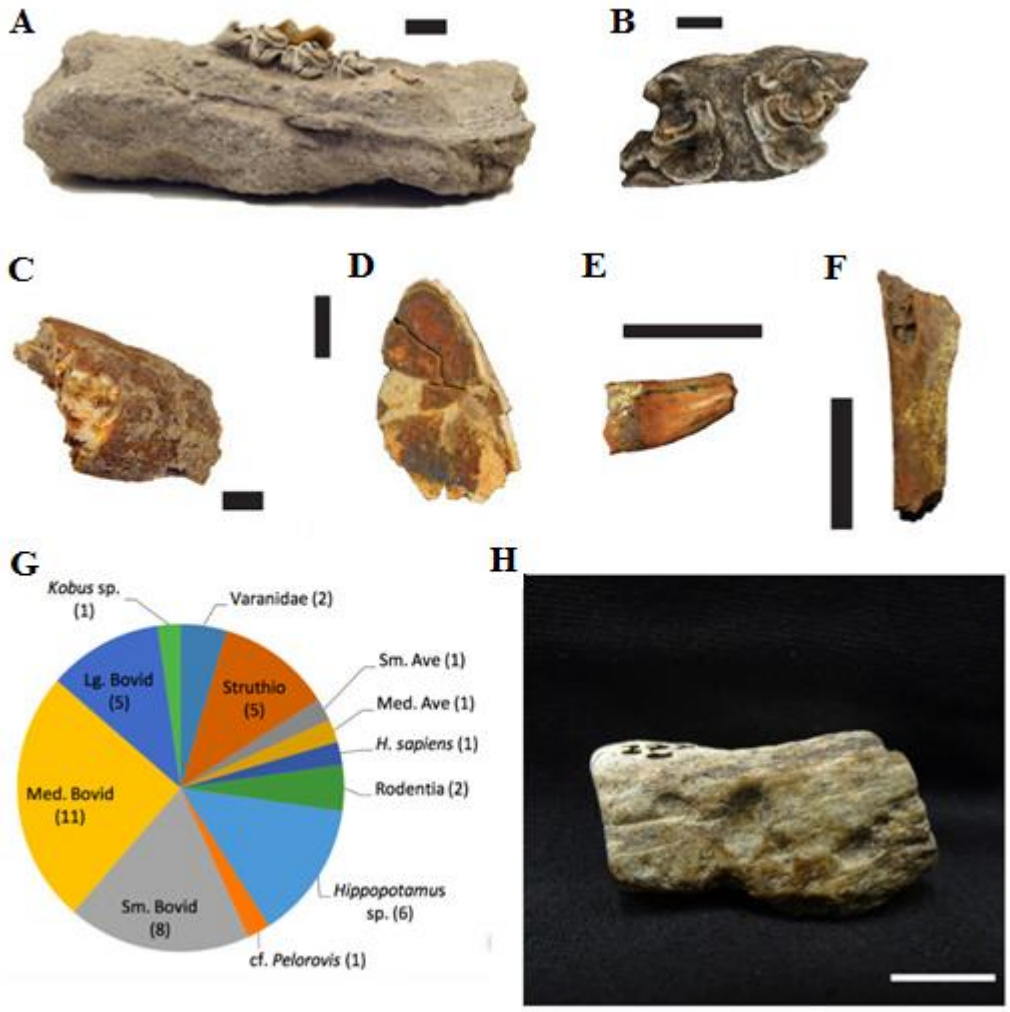

Supplementary Figure 20. Al Wusta vertebrate palaeontology. A: cf. *Kobus* sp. lower right M2-3; B: *Pelorovis* sp. mandibular fragment: C: *Hippopotamus* sp. ?upper canine fragment; D: *Hippopotamus* sp. medial upper incisor; E: *Varanus* sp. isolated tooth; F: Aves gen. et sp. indet. coracoid fragment; G: NISP for identified taxa. NISP is reported in parentheses; H: Evidence of carnivore gnawing on a bone fragment. Black scale bar = 10mm. White scale bar = 15mm.

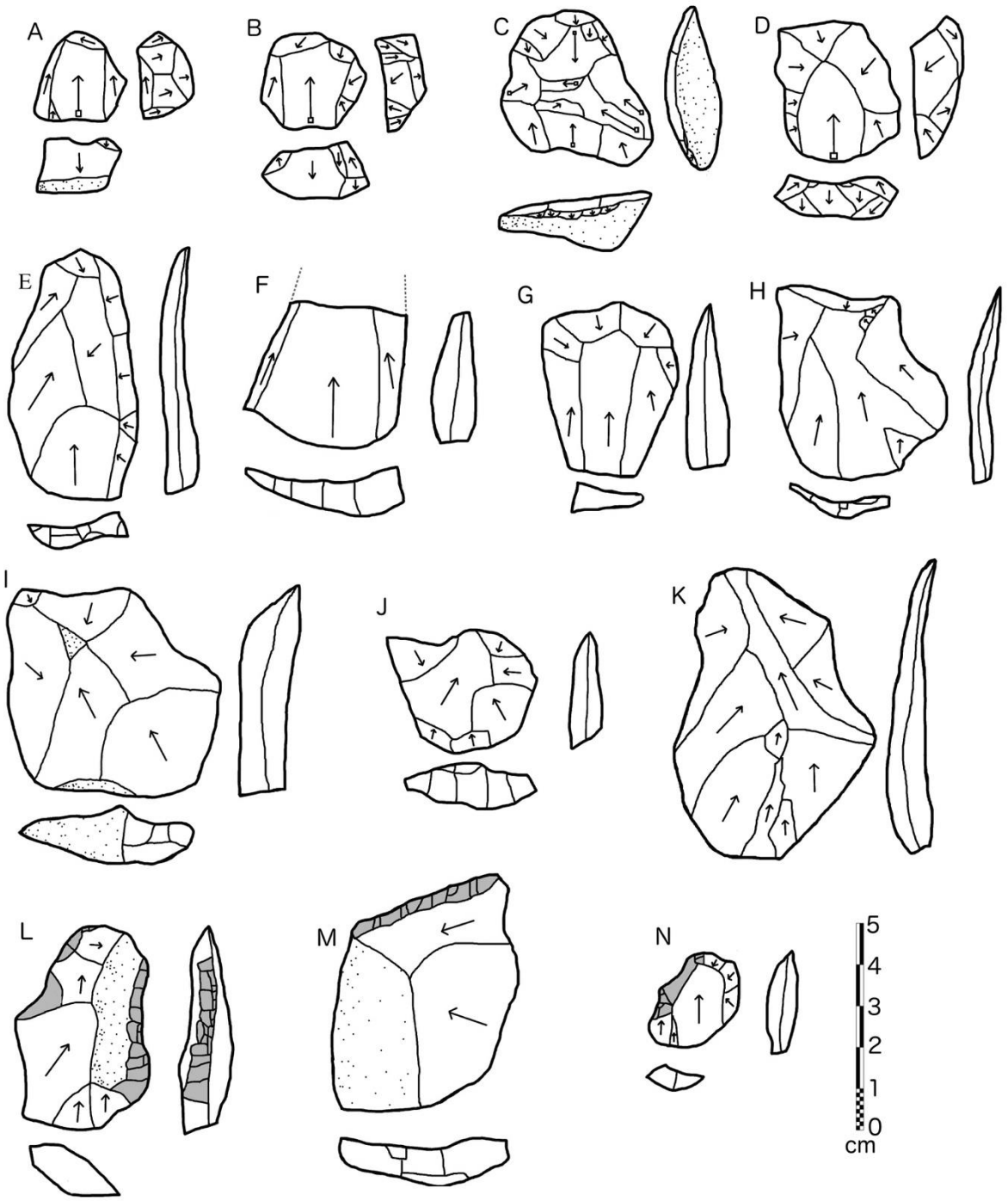

Supplementary Figure 21. Selected Al Wusta lithic artefacts. A,B,D: Preferential Levallois cores with centripetal preparation, C: recurrent centripetal Levallois core, E,G-K: Levallois flakes, F: broken Levallois point, L: double side retouched flake, M: end retouched flake, N: side retouched flake.